جامعة سيدي محمد بن عبد الله بفاس
UNIVERSITÉ SIDI MOHAMED BEN ABDELLAH DE FES

كلية العلوم ظهر المهراز فاس
FACULTE DES SCIENCES DHAR EL MAHRAZ FES

order N°: …76/2022..

Center for Doctoral Studies: Sciences and Techniques and Medical Sciences
Doctoral studies: Materials Sciences and Industrial Processes
Discipline: Physics
Specialty: Materials Science for Energy and Environment
Laboratory: Solid Physics

Thesis for obtaining a DOCTORATE

Prepared by: **Walid BELAID**

Electronic properties of III-nitrides single and multiple quantum wells for optoelectronic applications

Publicly defended on 23/12/2022 in front of the jury:

Pr. Anouar JORIO	USMBA, Faculty of sciences, Fez	President
Pr. Ahmed SALI	USMBA, Faculty of sciences, Fez	Reporter
Pr. Khalid RAHMANI	UM5, ENS, Rabat	Reporter
Pr. Khadija HTOUTOU	CRMEF Fez-Meknes, Meknes	Reporter
Pr. Yasin RAMAZAN EKER	NEU, Faculty of engineering, Konya, Turkey	Examiner
Pr. Hamdi SÜKÜR KILIÇ	Selcuk University, Faculty of sciences, Konya, Turkey	Examiner
Pr. Mimouna BAITOUL	USMBA, Faculty of sciences, Fez	Invited
Pr. Haddou EL GHAZI	UH-II, ENSAM, Casablanca	Co-supervisor
Pr. Izeddine ZORKANI	USMBA, Faculty of sciences, Fez	Supervisor

Academic year: 2022-2023

Declaration of Authorship

I, Walid BELAID, declare that this thesis titled, "**Electronic properties of III-nitrides single and multiple quantum wells for optoelectronic applications**" and the work presented in it are my own. I confirm that:

- This work was done wholly or mainly while in candidature for a research degree at this University.
- Where any part of this thesis has previously been submitted for a degree or any other qualification at this University or any other institution, this has been clearly stated.
- Where I have consulted the published work of others, this is always clearly attributed.
- Where I have quoted from the work of others, the source is always given. Except for such quotations, this thesis is entirely my work.
- I have acknowledged all main sources of help.
- Where the thesis is based on work done by myself jointly with others, I have made clear exactly what was done by others and what I have contributed myself.

Signed:

Date: 23/12/2022

Acknowledgments

My thesis wouldn't be possible without the contribution of some people.

Foremost, I would like to express my sincere gratitude to my co-supervisor Prof. **Haddou EL GHAZI** for the continuous support of my Ph.D. study and research, for his patience, motivation, enthusiasm, and immense knowledge. His guidance helped me in all the time of research and writing of this thesis. I could not have imagined having a better advisor and mentor for my Ph.D. study.

I would like to thank my thesis supervisor Prof. **Izeddine ZORKANI** for his useful and detailed discussions, patience, encouragement, and also for his always positive attitude that gives a lot of motivation to work.

I am very grateful to Prof. **Anouar JORIO** for his valuable advice, precise comments and for offering a fresh perspective on the work.

My warmest thanks to Professors **Ahmed SALI**, **Khalid RAHMANI** and **Khadija HTOUTO** for accepting to proofread this thesis and to be reviewers.

I would like to especially thank my dear Professors **Pr. Mimouna BAITOUL**, **Pr. Hamdi ŞÜKÜR KILIÇ** and **Pr. Yasin RAMAZAN EKER** for their interest in my work by participating in the jury of this thesis and being among the examiners. Also, I would like to acknowledge all people working in the solid-state laboratory for their help in all areas, just for smiling at me in the hall.

I would like to say thank you to my friends, **Dr. Redouane EN-NADIR**, **Mohamed Guerboub**, **Mohamed TIHTIH**, **Mohamed A. BASYOONI**, **Dr. Amina HOUIMI**, **Dr. Kamal ALAILI**, and **Dr**. **Mohamed EL-GAHOUCHI**, for their constant support, patience in listening to me and some distraction from this work.

Last but not the least, I would like to thank my family: my parents **Mohammed BELAID** and **Hakima MHIRECH** for giving birth to me in the first place and supporting me spiritually throughout my life. I would like to thank my brother and sister, **Yassine** and **Amal BELAID** for supporting me.

My special thanks go to my fiancee **Hanae KACHACH** for her endless support, and for always being there when I needed help.

Abstract

This work, separated into six chapters, deals with the study of the binding energy in III-nitrides-based simple and multiple quantum wells. Considering the effective-mass and dielectric mismatches between the well and its surrounding matrix, the numerical calculations are performed within the framework of the parabolic band and the single band effective-mass approximations under the finite potential barrier using the finite element method (FEM). To be close to reality, the diffusion effect at the interface between the well and the barrier is taken into account and an expression of the effective mass and dielectric constant is adopted. In addition, the pressure and temperature dependencies of the effective masse and dielectric constant were taken into account. In the first chapter, we presented a general overview of the nanostructures based on III-nitrides, their classifications, and their fields of application. We also recalled the electronic properties and the methods of numerical resolution. In the second chapter, we studied the binding energy of a shallow hydrogen impurity in single and double-coupled quantum wells based on hexagonal (In,Ga)N/GaN. The binding energy increases under the effect of the coupling, and it decreases for an off-center impurity. In the third chapter, we calculated the binding energy of a 1s donor impurity in symmetric double-coupled quantum wells based on hexagonal (In,Ga)N/GaN. We have shown that binding energy increases (decreases) with pressure for thick (thin) wells, and it decreases with well coupling. In the fourth chapter, we studied the binding energy of the ground state and the first two excited states of the hydrogenic impurity at the center of the double quantum wells (In,Ga)N/GaN for rectangular-shaped confinements, parabolic and triangular. The effects of well width and Indium concentration were taken into account in the calculations. The binding energy decreases with temperature and depends on the shape of the confinement potential. We have thus shown that the binding energy is greater for confinements of parabolic and triangular shape than for rectangular shape. In chapter five, we investigated the binding energy of the ground state and the first two excited states of the hydrogenic impurity at the center of (Al,Ga)N/AlN double quantum wells for rectangular-shaped confinements, parabolic and triangular, under the combined effects of temperature and electric field. His results show that the system dimension and the geometric shape have a significant influence on the binding energy. The latter decreases as a function of the electric field and the temperature. The binding energy strongly depends on the position of the impurity, it decreases when the impurity moves from the center to the edge. In the last chapter, we showed that the photovoltaic conversion efficiency can be modulated by optimizing the number of quantum wells and the thicknesses of the well, and the barrier in the active layer of the solar cells.

Keywords: Binding energy, quantum well, temperature, pressure, electric field.

Résumé

Ce travail, réparti en six chapitres, porte sur l'étude de l'énergie de liaison dans les puits quantiques simples et multiples à base de nitrures III. Compte tenu des décalages de masse effective et diélectrique entre le puits et sa matrice environnante, les calculs numériques sont effectués dans le cadre de la bande parabolique et des approximations de masse effective à bande unique sous la barrière de potentiel finie en utilisant la méthode des éléments finis (FEM). Pour être proche de la réalité, l'effet de diffusion à l'interface entre le puits et la barrière est pris en compte et une expression de la masse effective et de la constante diélectrique est adoptée. De plus, les dépendances à la pression et à la température de la masse effective et de la constante diélectrique ont été prises en compte. Dans le premier chapitre, nous avons présenté un aperçu général des nanostructures à base de nitrures III, leurs classifications et leurs domaines d'application. Nous avons également rappelé les propriétés électroniques et les méthodes de résolution numérique. Dans le deuxième chapitre, nous avons étudié l'énergie de liaison d'une impureté hydrogène peu profonde dans des puits quantiques à simple et double couplage à base de (In,Ga)N/GaN hexagonal. L'énergie de liaison augmente sous l'effet du couplage, et elle diminue pour une impureté excentrée. Dans le troisième chapitre, nous avons calculé l'énergie de liaison d'une impureté donneuse 1s dans des puits quantiques symétriques à double couplage basés sur l'hexagone (In,Ga)N/GaN. Nous avons montré que l'énergie de liaison augmente (diminue) avec la pression pour les puits épais (minces) et qu'elle diminue avec le couplage des puits. Dans le quatrième chapitre, nous avons étudié l'énergie de liaison de l'état fondamental et des deux premiers états excités de l'impureté hydrogénée au centre du double puits quantique (In,Ga)N/GaN pour des confinements de forme rectangulaire, parabolique et triangulaire. Les effets de la largeur du puits et de la concentration en indium ont été pris en compte dans les calculs. L'énergie de liaison diminue avec la température et dépend de la forme du potentiel de confinement. Nous avons ainsi montré que l'énergie de liaison est plus importante pour les confinements de forme parabolique et triangulaire que pour la forme rectangulaire. Dans le chapitre cinq, nous avons étudié l'énergie de liaison de l'état fondamental et des deux premiers états excités de l'impureté hydrogénée au centre de puits quantiques doubles (Al,Ga)N/AlN pour des confinements de forme rectangulaire, parabolique et triangulaire, sous la effets combinés de la température et du champ électrique. Ses résultats montrent que la dimension du système et la forme géométrique ont une influence significative sur l'énergie de liaison. Cette dernière diminue en fonction du champ électrique et de la température. L'énergie de liaison dépend fortement de la position de l'impureté, elle diminue lorsque l'impureté se déplace du centre vers le bord. Dans le dernier chapitre, nous avons montré que le rendement de conversion photovoltaïque peut être modulé en optimisant le nombre de puits quantiques et les épaisseurs du puits, et la barrière dans la couche active des cellules solaires.

Mots clés: Énergie de liaison, puits quantique, température, pression, champ électrique.

List of Acronyms

ADQW	**A**symmetric **D**ouble **Q**uantum **W**ells
AMQW	**A**symmetric **M**ultiple **Q**uantum **W**ells
BE	**B**inding **E**nergy
CD	**C**ompact **D**isc
CPA	**C**oherent **P**otential **A**pproximation
DIPQW	**D**ouble **I**nverse **P**arabolic **Q**uantum **W**ells
DPQW	**D**ouble **P**arabolic **Q**uantum **W**ells
DRQW	**D**ouble **R**ectangular **Q**uantum **W**ells
DTQW	**D**ouble **T**riangular **Q**uantum **W**ells
DVD	**D**igital **V**ersatile **D**isc
EDX	**E**nergy **D**ispersive **X**-ray **S**pectroscopy
FDM	**F**inite **D**ifference **M**ethod
FEM	**F**inite **E**lement **M**ethod
FF	**F**ill **F**actor
HVPE	**H**ydride **V**apor **P**hase **E**pitaxy
LD	**L**aser **D**iodes
LDS	**L**ow-**D**imensional **S**ystem
LED	**L**ight **E**mitting **D**iode
MOVPE	**M**etalorganic **V**apor-**P**hase **E**pitaxy
MQW	**M**ultiple **Q**uantum **W**ells
QD	**Q**uantum **D**ot
QR	**Q**uantum **R**ing
QW	**Q**uantum **W**ell
QWW	**Q**uantum **W**ell **W**ire
SQW	**S**ingle **Q**uantum **W**ell
VCA	**V**irtual **C**rystal **A**pproximation

List of Contents

Declaration of Authorship iii

Acknowledgments v

Abstract vii

Résumé ix

List of Acronyms x

List of Contents xii

List of Figures xvi

List of Tables xx

General Introduction 1

Chapter 1 Structural and electronic properties of III-Nitrides 6

1.1. Introduction 7

1.2. Structural properties 7

1.3. Electronic properties 10

1.3.1. Band structure 10

1.3.2. Effective mass 13

1.4. Elastic properties 15

1.4.1. Strain and stress 15

1.4.2. Spontaneous and Piezoelectric polarization 17

1.5. Structural Defects 22

1.6. Resistivity, mobility, and concentration of holders 23

1.7. Ternary alloys 25

1.8. Quantum confinement 26

1.8.1. Quantum Well 27

1.8.2. Quantum Wire 29

1.8.3. Quantum Dot 30

1.9. Effective Mass Approximation 30
1.10. Applications of element III-nitrides 34
1.10.1. Light-emitting diodes 34
1.10.2. Laser diodes 36
1.10.3. Ultraviolet photodetectors 37
1.10.4. Solar cells 38
1.11. Conclusion 39
Chapter 2 QW coupling impact on the binding energy in InGaN/GaN SQW and DQW under internal effects 40
2.1. Introduction 41
2.2. Theoretical approach 41
2.3. Effect of the structure size 44
2.3.1. Simple quantum well 44
2.3.2. Double quantum well 45
2.4. Effect of the impurity position 46
2.4.1. Simple quantum well 46
2.4.2. Double quantum well 47
2.5. Indium composition effect in a DQW 47
2.6. Coupling effect in DQW 49
2.7. Effect of number of layers 50
2.8. Conclusion 51
Chapter 3 Pressure-related binding energy in (In,Ga)N/GaN DQWs under internal effects 52
3.1. Introduction 53
3.2. Theoretical background 55
3.3. Results and discussion 57
3.4. Conclusion 63
Chapter 4 Effect of temperature on the binding energy in InGaN/GaN DQWs for different shapes 64
4.1. Introduction 65
4.2. Theoretical framework 65
4.3. Numerical Results and Discussion 68
4.4. Conclusion 77

Chapter 5 Combined effect of temperature and electric field on the binding energy in (Al,Ga)N/AlN for different shapes 78

5.1. Introduction 79

5.2. Theoretical approach 80

5.3. Numerical Results and Discussion 82

5.4. Conclusion 90

Chapter 6 Design optimization of multi-quantum well solar cells 91

6.1. introduction 92

6.2. Influence of the number of quantum wells on photovoltaic characteristics 92

6.3. Influence of the quantum wells thickness on photovoltaic characteristics 94

6.4. Influence of the barrier thickness on photovoltaic characteristics 95

6.5. conclusion 97

Conclusions and perspectives 98

References 101

List of Publications 116

List of Conferences 118

List of Figures

Figure I.1. Presentation of the band gap energies of several families of semiconductors according to their lattice parameter. **2**

Figure 1.1. Arrangement of atoms in the elementary lattice of (a) Hexagonal unit cell with the base vectors $\mathbf{a_1}, \mathbf{a_2}, \mathbf{a_3}$ and c (b) Cubic unit cell with the base vectors $\boldsymbol{a_1}, \boldsymbol{a_2}$ and $\boldsymbol{a_3}$ **8**

Figure 1.2. Schematic representation of (a) the wurtzite and (b) zinc-blende structures. The blue and red spheres indicate metal and N atoms, respectively. For the hexagonal the two tetrahedra are identical for the cubic there are opposites. **9**

Figure 1.3. Electronic band structures of InN, GaN, and AlN in wurtzite and zinc-blende crystal structures. The black full lines represent the calculations with PBE functional and the red dotted lines are representing the calculations with the $\mathrm{TB-mBJ}$ method. The Fermi level is shown as a horizontal dashed line (Figure extracted from the thesis of Araujo Rafael B. [53]). **11**

Figure 1.4. Schematic illustration of the spin-orbit splitting and crystal field splitting in wurtzite (WZ) materials compared to zinc blende (ZB) materials [56]. **12**

Figure 1.5. Valence band structure of GaN, indicating the anisotropy [61]. **14**

Figure 1.6. Demonstration of the effect of the stress σ in the zinc-blende phase in the direction (001) and (111) as well as in the wurtzite phase in the direction (0001). No polarization is generated in the cubic phase for stress following (001). On the other hand, a stress following (0001) in the hexagonal phase will generate a piezoelectric polarization equivalent to stress (111) in the zinc-blende structure (Figure extracted from the thesis of J. Simon [72]) **18**

Figure 1.7. The polarity of hexagonal GaN layers. (a): gallium polarity (b) nitrogen polarity. The red and blue spheres indicate Ga and N atoms, respectively. **21**

Figure 1.8. Orientation of spontaneous and piezoelectric polarizations for gallium polarity nitrides according to the stress: (1) layer A is in tension on layer B, (2) layer A is in compression on layer. **21**

Figure 1.9. Schematic illustration of point defect types in the crystal structure. **22**

Figure 1.11. Schematic representation of a quantum well. CB and VB are, respectively, the conduction band and the valence band. L_w and L_b are, respectively, the thickness of the well and barrier materials. **27**

Figure 1.12. Light output (without light extraction) for III-V semiconductor-based diodes, according to: a: [90], b: [91], c: [92], d: [93]). **34**

Figure 1.13. Structure of a light-emitting diode [101]. **35**

Figure 1.14. Schematic diagram of the structure of the GaN-based LD with different MQWs [105]. **36**

Figure 1.15. Schematic diagrams of non-polar GaN-based p-i-n photodetector [108]. **37**

Figure 2.1. Single $GaN/In_{\upsilon}Ga_{1-\upsilon}N$ QW and double coupled $GaN/In_{\upsilon}Ga_{1-\upsilon}N/$ $GaN/In_{\upsilon}Ga_{1-\upsilon}N/$ GaN QWs description under study. **42**

Figure 2.2. Binding energy in GaN/(In,Ga)N/GaN SQW as a function of the well width under the effect of the barrier width. **44**

Figure 2.3. Binding energy in GaN/(In,Ga)N/GaN DQW as a function of the well width under the effect of the barrier width. **45**

Figure 2.4. Binding energy in GaN/(In,Ga)N/GaN SQW as a function of the well width under the effects of the impurity's position. **46**

Figure 2.5. Binding energy in GaN/(In,Ga)N/GaN DQW as a function of the well width under the effects of the impurity's position. **47**

Figure 2.6. Ground-state binding energy according to well width for three different values of the Indium concentrations. **48**

Figure 2.7. Ground-state binding energy in DQW as a function of the well width for two different values of the coupling barrier width. **49**

Figure 3.1. The schematic diagrams of double QWs under study based on $(In, Ga)N/GaN - DQWs$. The 1s-like density probability and its corresponding eigen-value are reported for two different values of impurity position for P=0 GPa. .....Error! Bookmark not defined.

Figure 3.2. The 1s-like binding energy in $\mathbf{In_{.2}Ga_{.8}N}/GaN$ DQW versus the impurity position for three different values of the hydrostatic pressure..... **57**

Figure 3.3. The 1s-like binding energy in symmetric $(In, Ga)N/GaN - DQWs$ as a function of the well width at room temperature for two different positions of the impurity. **59**

Figure 3.4. The 1s-like binding energy in (In,Ga)N/GaN-DQWs versus the well width at $T = 300K$ and $\mathbf{Z_i = 2L_b + 3/2L_w}$ for three different values of hydrostatic pressure. **60**

Figure 3.5. The 1s-like binding energy in (In,Ga)N/GaN-DQWs versus the well width at $T = 300K$ and $\mathbf{Z_i = 2L_b + 3/2L_w}$ for three different values of In-composition. **61**

Figure 3.6. The DQW 1s-like binding energy as a function of the well width at room temperature for three different values of the barrier width. **62**

Figure. 4.1. Probability density of 1s, 2s, and 2p states in finite InGaN/GaN on-center donor impurity DRQW, DPQW and DTQW as a function of the growth direction. Potential profiles are included.....Error! Bookmark not defined.**68**

Figure. 4.2. Variation of the donor 1s, 2s and 2p states energies versus well width in a $GaN/In_{.25}\mathbf{Ga_{.75}N}$ rectangular, parabolic and triangular DQWs for fixed parameters L = **1** and H =

1.5, in the presence (a) absence (b) of impurity, at T=0K (solid curve), T=300K (dashed curve) and T=900K (dotted curve). **70**

Figure 4.3. The 1s, 2s and 2p states binding energy Eb as a function of the well width in a $\mathrm{GaN/In_{\upsilon}Ga_{1-\upsilon}N}$ DRQW, DPQW and DTQW for fixed parameters $\nu = 0.1$, $\mathrm{L_b} = \mathbf{1}$, $\mathbf{L_{b1}} = \mathbf{1.5}$, for different temperature values T=0K (solid curve), T=300K (dashed curve) and T=900K (dotted curve). **71**

Figure 4.4. Variation of 1s, 2s and 2p states binding energy Eb with temperature T in DRQW, DPQW and DTQW for fixed parameters $\nu = 0.1, \mathrm{L_b} = \mathrm{L_{b1}} = 1$ and $\mathrm{L_w} = 2$ with donor impurities located in the structure center (solid curve), in the right well center (dashed curve) and in the right barrier center (dotted curve). **73**

Figure 4.5. The ground state, 2s, and 2p states binding energy $\mathbf{Eb}$ of an on-center hydrogenic donor impurity as a function of the side barrier's width of DRQW, DPQW and DTQW for different coupling barrier widths $\mathbf{L_{b1}} = \mathbf{0.5}, \mathbf{1.0}$ and 1.5 with an indium content $\nu = 0.1, \mathrm{L_w} = 2$ and T=300K. **74**

Figure 4.6. Ground state binding energy $\mathrm{E_b}$ of an on-center hydrogenic donor impurity as a function of the side barrier's width of DRQW, DPQW and DTQW for fixed parameters T = 300 K, $\mathrm{L_{b1}} = 1, \mathrm{L_w} = 2$ for different indium content $\nu = 0.1, 0.2$ and 0.3.Error! Bookmark not defined.**75**

Figure 5.1. The variations of the confinement potential profile, ground, first and second excited state energies and the squared wave functions for related energy levels for different values of the electric field. **83**

Figure 5.2. The 1s, 2s, and 2p states binding energy $\mathrm{Eb(meV)}$ as a function of the well width $\mathrm{Lw(ab*)}$ in $\mathrm{AlN/Al_{1-\upsilon}Ga_{\upsilon}N}$ DRQW, DPQW, and DTQW for fixed parameters υ=0.1, L_b= 1, L_{b1} =0.5 at $\mathrm{T} = 300°\mathrm{K}$, for two values of electric field $\eta = 0$ (blue curve) and $\eta = 60$ (red curve).**84**

Figure 5.3. The 1s, 2s, and 2p states binding energy $\mathbf{Eb(meV)}$ as a function of the well width $\mathbf{Lw(ab*)}$ in $\mathbf{AlN/Al_{1-\upsilon}Ga_{\upsilon}N}$ DRQW, DPQW, and DTQW for fixed parameters $\boldsymbol{\upsilon}$=0.1, $\mathbf{L_b}$= 1, $\mathbf{L_{b1}}$ =0.5 with $\boldsymbol{\eta} = \mathbf{0}$, for two values of temperature $\mathbf{T} = \mathbf{300°K}$ (blue curve) and $\mathbf{T} = \mathbf{500°K}$ (red curve). **87**

Figure 5.4. The difference of the 1s, 2s, and 2p-states shallow-donor binding energy $\mathbf{\Delta Eb(meV)}$ of (Al,Ga)N/AlN DRQW, DPQW and DTQW as a function of the electric field $\boldsymbol{\eta}$ (a) and temperature T (b) for the fixed parameters $\boldsymbol{L_w}$=3, $\boldsymbol{L_b}$=1, $\boldsymbol{L_{b1}}$=0.5 and $\boldsymbol{\upsilon}$= 0.1. ..... **88**

List of Tables

Table 1.1. Mesh parameters of III-nitrides in cubic and hexagonal phases. **10**

Table 1.2. Gap (eV) for binary nitrides of element III in hexagonal and cubic phase [57]. **13**

Table 1.3. Effective masses of electrons and holes of InN, GaN, and AlN in hexagonal and cubic phases [57]. **14**

Table 1.4. Experimental and theoretical constants of InN, GaN, and AlN in GPa. **16**

Table 1.5. State of the art of InGaN-based solar cells. **38**

Table 3.1. Materials parameters used in our calculation. **58**

Table 4.1. Parameters used in the computation. **67**

Table 4.2. The variation of the barrier height, the effective mass and dielectric constant for both well and barrier regions with temperature T for $\nu = 0.1$. **72**

Table 5.1. Physical parameters of wurtzite AlN and GaN used in our computations. **82**

Table 5.2. The variation of the energy difference $\Delta \mathrm{E}$ (meV) between the two lowest excited states and the ground state with the electric field. **85**

Table 5.3. The variation of the barrier height, the effective mass, and dielectric constant for both well and barrier regions with temperature T for υ= 0.1 and η=0. ..... **86**

Table 6.1. Experimental values of the structural properties and photovoltaic performance of In0.1Ga0.9N/GaN multiple-quantum-well solar cells: number of quantum wells ($\mathrm{N_w}$), external quantum efficiency (EQE), open-circuit voltage ($\mathrm{V_{oc}}$), short-circuit current ($\mathrm{J_{sc}}$), fill factor (FF), and overall conversion efficiency (η) under 1 sun AM1.5 G equivalent illumination [206]. **93**

Table 6.2. Theoretical values of the binding energy (meV) of $\mathrm{In_{.1}Ga_{.9}N(1nm)/GaN1nm}$ multiple-quantum well with number of quantum wells ($\mathbf{N_w}$). **94**

Table 6.3. Electrical characteristics of samples with different QW thicknesses: short-circuit current Jsc, open-circuit voltage $\mathbf{V_{oc}}$, fill factor FF and conversion efficiency η [207]. **94**

Table 6.4. Theoretical values of the binding energy (meV) of $\mathbf{In_{.1}Ga_{.9}N(L_w)/GaN(1nm)}$ multiple-quantum well with quantum wells thickness ($\mathbf{L_w}$). **95**

Table 6.5. Summary of the electrical characteristics: external quantum efficiency EQE, open-circuit voltage $\mathrm{V_{oc}}$, short-circuit current $\mathrm{J_{sc}}$, fill factor FF, conversion efficiency η for $15 \times \mathrm{In_{.17}Ga_{.83}N(2nm)/GaN}$ −based devices with different barrier thicknesses under $1\ \mathrm{Sun\ AM1.5G}$ equivalent illumination. **96**

Table 6.6. Theoretical values of the binding energy (meV) of $\mathbf{In_{.1}Ga_{.9}N(1nm)}/\mathrm{GaN(L_b)}$ simple-quantum well with barrier thickness ($\mathbf{L_b}$). **96**

General Introduction

Since the middle of the last century (first coherent emission: H. Maiman) many optical and optoelectronic devices such as lasers and light emitting diodes have entered our everyday life. Such devices were able to see the light of day thanks to the formidable materials that are semiconductors. Indeed, the physical properties of these allow them to efficiently convert electrical energy into light energy and vice versa (p-n junction).

There are different families of semiconductors classified according to their chemical nature and physical properties. The study presented here was carried out on element III-nitrides, the best-known representatives of which are GaN, AlN, InN and their alloys AlGaN and GaInN. These materials generally have a relatively high direct gap capable of covering a large part of the visible and UV spectrum (see Figure I.1).

III-nitride materials (GaN, AlN, InN, and their alloys) exhibit remarkable properties, the most important of which is their direct forbidden bandwidth which varies between 0.65 eV (InN) and 6.2 eV (AlN), which thus makes it possible to cover a wide range of wavelengths ranging from infrared to ultraviolet. Other properties such as their high thermal and mechanical stability, their high piezoelectric constants, or their large spontaneous polarization make nitride materials very good candidates for the fields of electronic and optoelectronic applications.

The effort on the development of nitride semiconductors, in particular GaN, intensified in the sixties and seventies due to the potential of this material and its alloys for the manufacture of light-emitting diodes in the spectral ranges. blue and ultraviolet (UV). In 1969, Maruska and Tietjen [1] developed GaN for the first time by hydride vapor phase epitaxy (HVPE).

Shortly thereafter, GaN was synthesized by vapor phase epitaxy by decomposition of organometallics (metalorganic vapor phase epitaxy, MOVPE) [2] and by molecular beam epitaxy (MBE) [3]. The advancement of nitride technology has been stunted by many problems. First, there was no GaN compatible substrate, so the material had to be deposited on high mesh mismatch

substrates, such as sapphire or Si (111). This heteroepitaxial GaN was very conductive due to impurities and crystal defects. This residual n-type conductivity, combined with the high activation energy of the acceptors, made the fabrication of p-n junctions difficult. Despite these problems, Pankove et al. [4] presented in 1971 the first light-emitting diode (LED) based on GaN, a diode that consisted of a metal-insulator-semiconductor structure.

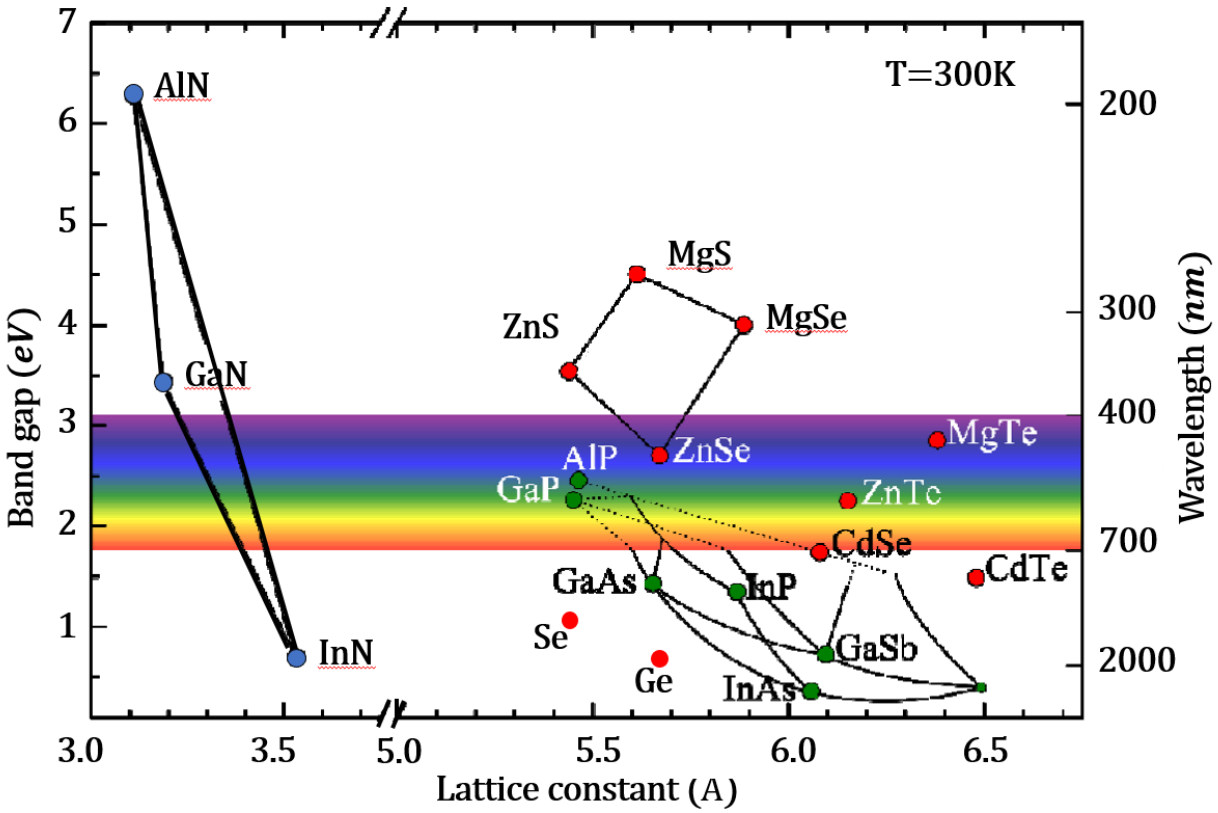


Figure I.1. Presentation of the band gap energies of several families of semiconductors according to their lattice parameter.

In 1983, Yoshida et al. [5] demonstrated that the use of an intermediate AlN layer between the sapphire substrate and the GaN epitaxial layer significantly increased the luminescence of the material. Another major advance in research on nitride semiconductors was made in 1989 by Amano et al. [6]: These demonstrated that highly resistive Mg-doped GaN could become p-type conductive after exposure to an electron beam in a scanning electron microscope. This discovery made it possible to manufacture the first nitride LED with a p-n junction. Sometime later,

Nakamura et al. were successful in activating the acceptor Mg by annealing at $700\,℃$ in an N_2 atmosphere [7].

The development of InGaN-based quantum wells by Nakamura made it possible to significantly improve the performance of LEDs [8–10], progress which culminated in November 1993 with the announcement of the massive production and marketing of blue LEDs. manufactured by Nichia Chemical Industries. The first blue laser diode operating continuously at room temperature was published by Nichia in 1997 [11]. Blue and green diodes are a commercial reality today, as are laser diodes in these spectral regions. A new generation of high-density DVDs based on nitride technology is already on the market. Research efforts in the field of nitride optoelectronics are now focused on replacing illumination with white diodes and extending the emission wavelength to the far UV. On the photodetector side, Nitride-based Schottky photodiodes have been marketed by APA Optics since 1998 and their application in the assessment and monitoring of solar UV radiation has become widespread very quickly.

Group III nitrides are also promising materials for applications in high-frequency and high-power electronics. The defense industry needs advanced components for radar and satellite communications, but the most promising market for these components remains the replacement of GaAs technology in third-generation base stations. One of the biggest costs of these systems is the refrigeration required to reduce noise levels, an area in which nitride technology has clear advantages. Today, nitride transistors still pose stability and break-down problems, but experts expect these components to be commercialized within two years.

Recently, the electronic properties were examined using different methods: variational approach [12–17], finite element method [18–22], difference finite method [23,24], plane wave expansion method [25–27], perturbation method [28], matrix diagonalization method [29] and density functional theory [30] . However, in the presence of a hydrogenic donor impurity, few studies were devoted to investigating the electronic properties of multiple quantum dots [31–34]. (Al,Ga)N/AlN multiple quantum wells (MQWs) with high structural and optical qualities have also been successfully fabricated and investigated [35–37]. Based on symmetric and asymmetric multiple quantum wells (MQWs) systems, several theoretical papers are reported in the literature, such as double parabolic quantum well (DPQW) [38], double inverse parabolic quantum well (DIPQW) [39], double asymmetric quantum wells (DAQW) [40,41], asymmetric multiple

quantum wells (AMQWs) [42].

Due to their particular properties, coupled double quantum wells (DQWs) contain an extra degree of electronic freedom in the growth direction, giving rise to new transport phenomena not found in single-electron layers. This system holds promise for future quantum effect electronic devices, and also photonic devices based on III-V compound semiconductors InN, GaN, and InGaN. This system consists of two quantum wells separated by a narrow barrier that electrons can tunnel through. Several quantum effect devices have already been proposed for DQWs. The DQWs are no longer only promising systems for fundamental research but are definitely important for future industrial applications. The purpose of this thesis is to the optimization of the binding energy in single and double quantum wells by taking into account the effect of the external and internal parameters (temperature, electric field, the composition of alloys, mismatch, ...) as well as the dimension and the shape of the structure and of confinement potential.

More specifically, the studies carried out in this thesis are divided into five chapters as follows:

In chapter 1, we present the state of the art on materials based on III-nitride. This chapter is mainly focused on the description of the basic properties of semiconductors based on element III nitrides to understand the nature of the materials and use them correctly for each application. We give a detailed description of the materials and techniques used for their manufacture which are essential to understand the performance of the devices.

In the second chapter, we exploit the binding energy of the shallow hydrogen impurity in single and double quantum wells based on unstrained wurtzite (In,Ga)N/GaN.

In the third chapter, we provide the calculation of the 1s-type binding energy of a shallow impurity donor in symmetric double-coupled quantum wells based on (In,Ga)N/GaN wurtzite.

In the fourth chapter, we study the binding energy bound to shallow soil donors and two low excited states of the central hydrogen impurity in double quantum wells (In,Ga)N/GaN for rectangular (DRQW), parabolic (DPQW) and triangular (DTQW), under the combined effects of temperature and electric field. The effects of well width and gallium concentration were also taken into account in the calculations.

In the fifth chapter, we study the binding energy bound to shallow soil donors and two low excited states of hydrogen impurities centered in double quantum wells (Al,Ga)N/AlN for rectangular (DRQW), parabolic (DPQW), and triangular potential profiles (DTQW), under the combined effects of temperature and electric field.

In the last chapter, we summarized the influence of the insertion of MQW structure in the intrinsic region of p-i-n solar cells, as well as the influence of well thickness, barrier thickness, and the number of quantum wells in a structure on the binding energy.

Chapter 1

Structural and electronic properties of III-Nitrides

1.1. INTRODUCTION

In this chapter, the basic properties of III-nitride semiconductors are described to understand the nature of the materials and properly use them for each application. The first section of this chapter discusses the crystal properties, specifically crystal structure and crystal polarity, followed by their electronic properties, which are divided into band structure and effective mass. The concepts of stress, strain, and the intrinsic natures of spontaneous and piezoelectric polarization are then demonstrated. Furthermore, the defects found in the III-nitride system are discussed. The last part of the chapter is dedicated to the applications of III-N-based semiconductors such as light-emitting diodes, laser diodes, ultraviolet photodetectors, and solar cells.

1.2. STRUCTURAL PROPERTIES

One element from column XIII (B, Al, Ga, In) and one element from column XV make up the III-V materials (N, P, As, Sb). They are isoelectronic with the elements of column XIV (C, Si, Ge, Sn) and thus share properties such as crystal structure and semiconductor character. Since they are tetravalent, they form a chemical bond via sp^3 hybridization. Crystals of wurtzite ($P6_3mc - C_{6v}$ space group) or zinc-blende (space group $F\bar{4}3m - Td$ space group) are formed depending on whether the compact stack is hexagonal (ABAB stack…) or cubic (ABCABC stack…) respectively. This class of material includes III-N nitride semiconductors. BN, on the other hand, is a bit unique in that it, like carbon, can be formed via sp2 hybridization (which then forms graphite). If the stack is hexagonal, we get the "graphitic" structure of the space group $P6_3 / mmc$ (D6h), and if it's cubic, we get the rhombohedral structure (R3m space group).

The wurtzite structure is the most stable for InN, GaN, and AlN semiconductors, but only slightly, because the energy gain is only about the order of 15 $meV / atom$ once compared to the zincblende structure. As a result, the latter structure can be easily synthesized, either accidentally by introducing a stacking fault in the wurtzite structure (a C plane in the ABAB stack) or more extensively by changing the growth conditions. The graphitic is the most stable structure for BN.

The most stable structure for InN, GaN, and AlN is the wurtzite structure, but by little, because the energy gain is only of the order of $15\,meV\,/$ atom compared to the zinc-blende structure [43]. Thus, the latter structure can be formed easily, accidentally by introducing a stacking fault in the wurtzite structure (a C plane in the ABAB stack), or more extensively by changing the growing conditions [44]. For BN, the most stable structure is the graphitic structure.

We can therefore see that GaN, AlN, and InN have similar stable structures, while that of BN is different. In this thesis, at the level of standard nitrides, we were interested in the ternary alloy $In_vGa_{1-v}N$, which can be seen as an alloy formed from single nitrides InN and GaN, and has a crystal structure derived from them. We will now detail each structure in more detail, first the pure materials and then the alloy.

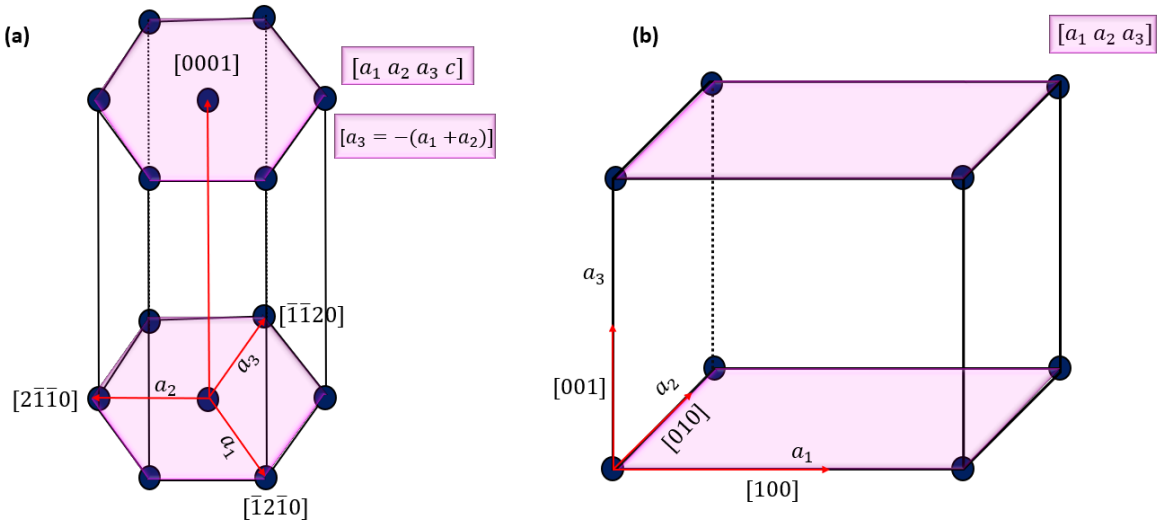


Figure 1.1. Arrangement of atoms in the elementary lattice of (a) Hexagonal unit cell with the base vectors a_1, a_2, a_3 and c (b) Cubic unit cell with the base vectors a_1, a_2 and a_3.

Element III-nitrides can exist in two different crystal forms (polytypes): the zinc-blende structure (cubic) and the wurtzite (hexagonal) structure both shown in Figure 1.1. The zinc-blende structure can be represented by two face-centered cubic networks occupied one by the III element atoms and the other by the nitrogen atoms and shifted by a quarter of the main diagonal of the mesh, i.e., (¼ ¼ ¼). Likewise, the wurtzite structure corresponds to two hexagonal networks each

composed of one of the two species of atoms and shifted along the c axis by $5/8$ of the cell unit. These two polytypes are relatively close from a crystalline point of view; the direction (0001) of

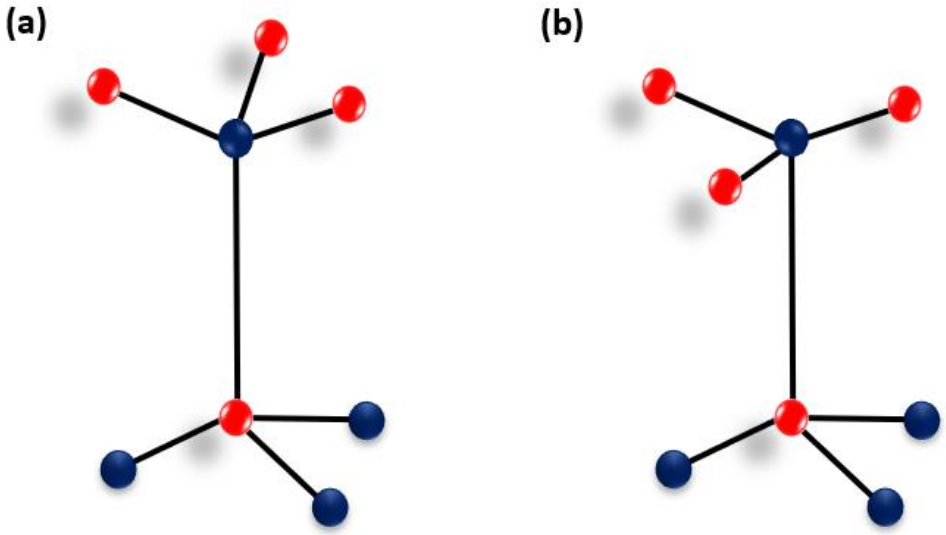


Figure 1.2. Schematic representation of (a) the wurtzite and (b) zinc-blende structures. The blue and red spheres indicate metal and N atoms, respectively. For the hexagonal the two tetrahedra are identical for the cubic there are opposites.

the hexagonal phase differs from the direction (111) of the cubic phase only by the stacking sequence of the crystalline planes (see Figure 1.1). As a result, the two structures are differentiated for an atom only from its third neighbor (see Figure 1.2). Unlike the thermodynamically stable hexagonal structure, the cubic structure is metastable. The energy difference for each atom between the two phases was determined by ab initio calculations leading to the following values for the different materials: -11.44 meV for InN, -9.88 meV for GaN, and -18.41 meV for AlN [43]. Despite this metastable character, the cubic phase can appear, for example as a parasitic form in a hexagonal layer if the crystal has many structural defects, in particular stacking faults. It can also be obtained in the form of a thick single-phase layer by rigorously adjusting the growth parameters. One of the key points in the growth of good quality cubic and hexagonal layers is the choice of substrate, note that there is no tuned mesh substrate for these materials.

Despite recent results obtained by Soukhoveev et al. [45] showing solid GaN layers 5 cm diameter, massive nitride substrates are still confined to the laboratory research stage due to their

small size. The growth of nitrides is therefore generally heteroepitaxy (growth of one material on another of a different nature). It follows that there is an important difference in lattice parameters between the substrate and the epitaxial layer. This difference will cause the appearance of stress inside the first deposited monolayers. This stress will then quickly relax in the form of structural defects such as the dislocations so numerous in nitrides; hence the importance of the choice of substrate. The mesh parameters of the nitrides are presented in Table 1.1 for the hexagonal phase and the cubic phase.

Table 1.1. Mesh parameters of III-nitrides in cubic and hexagonal phases.

	InN	GaN	AlN	References
Zinc-blende	$a = 4.50$ Å	$a = 4.38$ Å	$a = 4.98$ Å	[46–48]
	$a = 4.53$ Å	$a = 4.3996$ Å		[49,50]
	$a = 4.452$ Å	$a = 4.34$ Å	$a = 4.981$ Å	[51]
Wurtzite	$a = 3.189$ Å	$a = 3.112$ Å	$a = 3.548$ Å	[52]
	$a = 5.185$ Å	$a = 4.982$ Å	$a = 5.760$ Å	

For the hexagonal phase, the state of the art in terms of structural quality which is much better than its cubic counterpart, the values presented in Table 1.1 will be adopted as a reference. Regarding the cubic phase, some dispersion of the mesh parameters can be noted. This is partly due to the difficulty of obtaining thick layers of high structural quality today. Indeed, the presence of structural defects (point defects, inclusion of parasitic hexagonal phase), as well as the presence of stress in the layers, will cause this dispersion in the measurements.

1.3. ELECTRONIC PROPERTIES

1.3.1. Band structure

Knowledge of the band structure of a semiconductor is the essential parameter for the realization of devices. One of the important points of the band structure is the value of the energy separating the maximum of the valence band from the minimum of the conduction band (“gap” of the material).

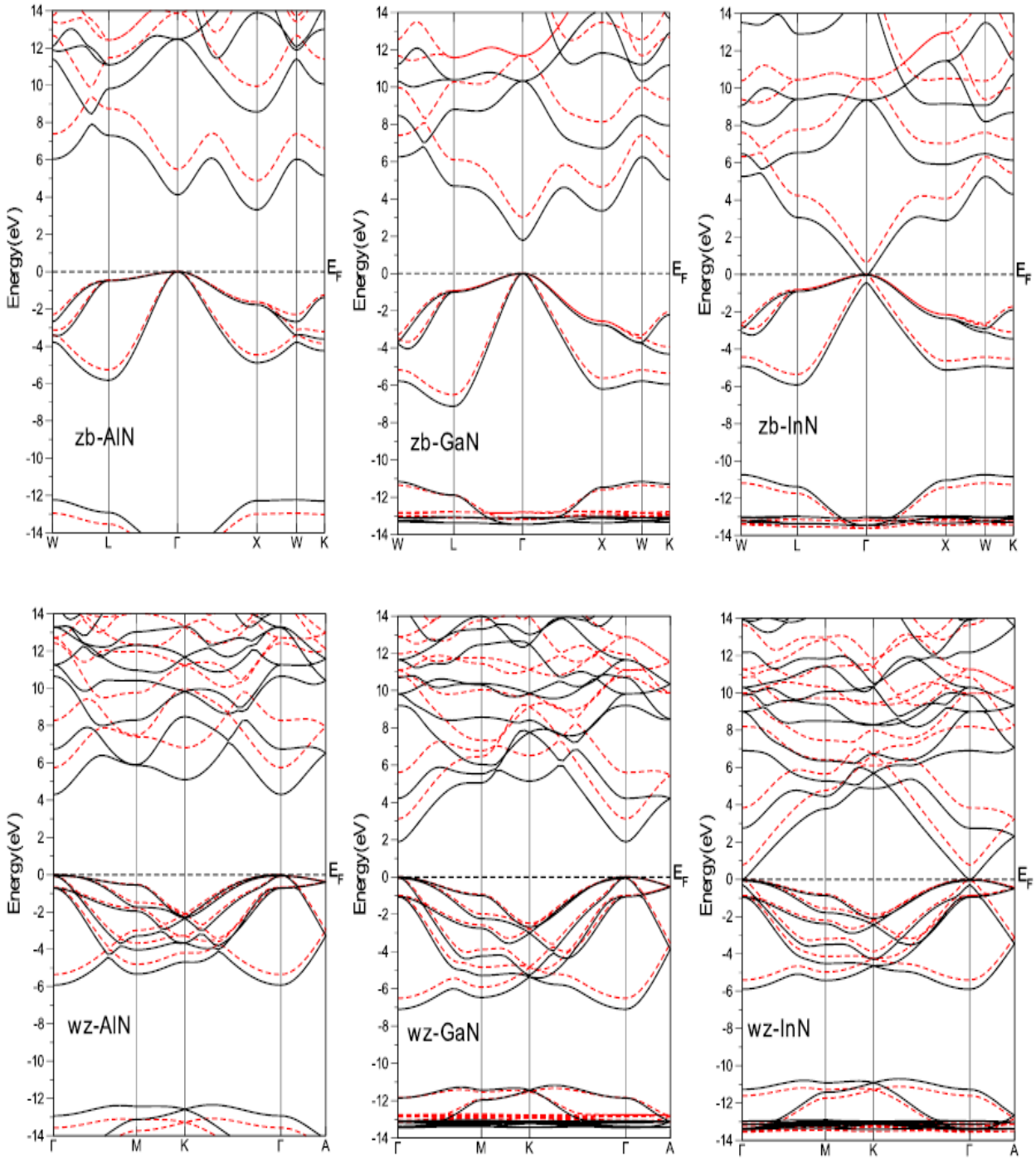


Figure 1.3. Electronic band structures of InN, GaN, and AlN in wurtzite and zinc-blende crystal structures. The black full lines represent the calculations with PBE functional and the red dotted lines are representing the calculations with the $\mathrm{TB}-\mathrm{mBJ}$ method. The Fermi level is shown as a horizontal dashed line (Figure extracted from the thesis of Araujo Rafael B. [53]).

We present in Figure 1.3 the band structures obtained for AlN, GaN, and InN in the two crystal phases by the empirical method of pseudo-potentials, this method provides the best results in terms of comparison with the experimental measurements of the gap.

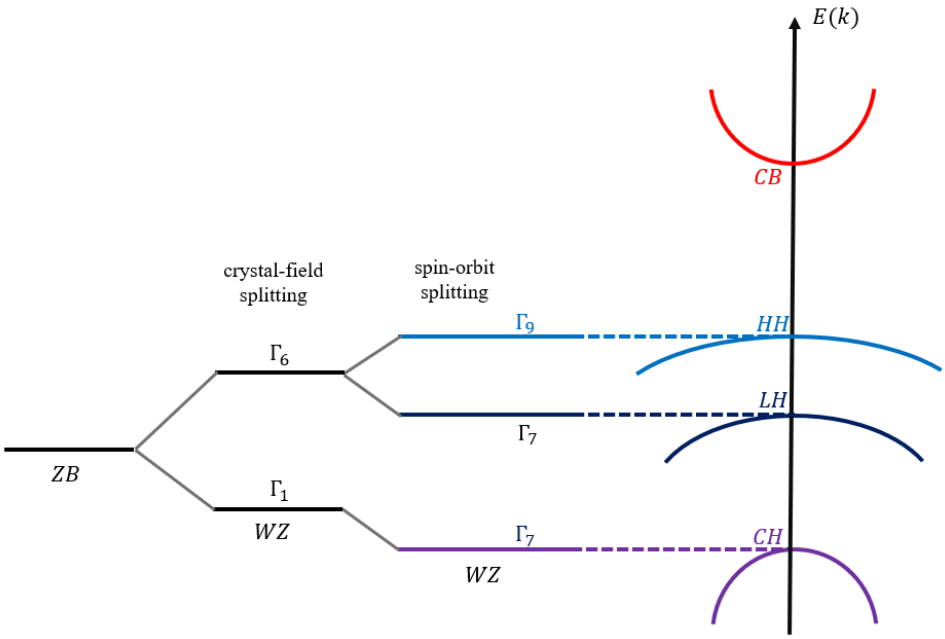


Figure 1.4. Schematic illustration of the spin-orbit splitting and crystal field splitting in wurtzite (WZ) materials compared to zinc blende (ZB) materials [56].

Element III-nitrides generally have a direct gap, that is to say, that the minimum of the conduction band and the maximum of the valence band are aligned in the "k space" at the center of the zone of Brillouin. Despite the similarity between the direction (111) of the cubic phase and the direction (0001) of the hexagonal phase, we notice from Figure 1.3 that the band structure differs between the two phases. More precisely at the point Γ where the radiative transitions for the two phases sit (see Figure 1.4), the spin-orbit coupling divides the top of the valence band into two levels for the cubic phase. One corresponds to the bands of heavy holes (HH), light holes (LH) degenerated at point Γ_8, the second (state Γ_7) corresponds to the band of "split-off" (SH) holes shifted by Δ_{SO} compared to Γ_8. In addition to the spin-orbit coupling there exists for the hexagonal phase an electric field called crystalline field coming from the non-cubicity of this phase which will remove the degeneration at point Γ of heavy holes and light holes. This will create three energy levels on the top of the valence band, thus leading to the existence of three excitons: A, B, and C

for the hexagonal phase. An exciton is the quasi-particle created by an electron and a hole in Coulomb interaction, the exciton binding energy is relatively high in $GaN \approx 30$ meV, so this allows the presence of excitons in GaN at room temperature. We will simply add for information that the energy differences between these three excitonic levels can be calculated by the quasi-cubic model of Hoppfield [54] from the values of Δ_{SO} and Δ_{CR}. Different values of Δ_{SO} and Δ_{CR} obtained by calculation and experiment are available and referenced in the review done by Jain et al. [55].

Table 1.2. Gap (eV) for binary nitrides of element III in hexagonal and cubic phase [57].

	InN	GaN	AlN
Wurtzite	1.994	3.507	6.23
Zinc blende	1.94	3.299	4.9

In summary, we report in Table 1.2 the widths of the band gaps of AlN, GaN, and InN binary nitrides considered as "acquired" in the hexagonal phase and the cubic phase at low temperatures.

1.3.2. Effective mass

The effective masses of the carriers in a semiconductor are directly related to the band structure of the latter; they are proportional to the inverse of the curvature of the bands. and can be derived from Eq. (2.5) by assuming a parabolic curvature of the (E, k).

$$\frac{d^2E}{d^2k} = \frac{\hbar^2}{m^*} \tag{1.1}$$

It is interesting to note that the effective mass of the electrons in a direct gap semiconductor varies little with the crystallographic direction, so m_e^* will represent an average value according to the different directions. Thus, the effective mass has a smaller value for the bands with a higher degree of curvature (for example, the Γ-valley of GaN in comparison to the K-valley and M-L-valleys, as illustrated in Figure 1.5).

In approximations, the bands are assumed parabolic and the average effective masses are taken from different experimental measurements, such as infrared reflectivity, Hall effect [58], cyclotron resonance [59], and picosecond time-resolved photoluminescence [60].

There are many values in the literature resulting from calculations or experimental measurements of the effective electronic masses in hexagonal GaN: the community of nitrides

today agrees on the value of $0.20\, m_e \pm 0.02$. Concerning GaN in the cubic phase, we count a few experimental measurements, the theoretical data are also much less numerous than for GaN wurtzite. For AlN, there is currently no measurement of the effective mass of the electrons in either of the two crystal phases. The commonly used effective masses of electrons and holes of wurtzite GaN and AlN are summarized in Table 1.3.

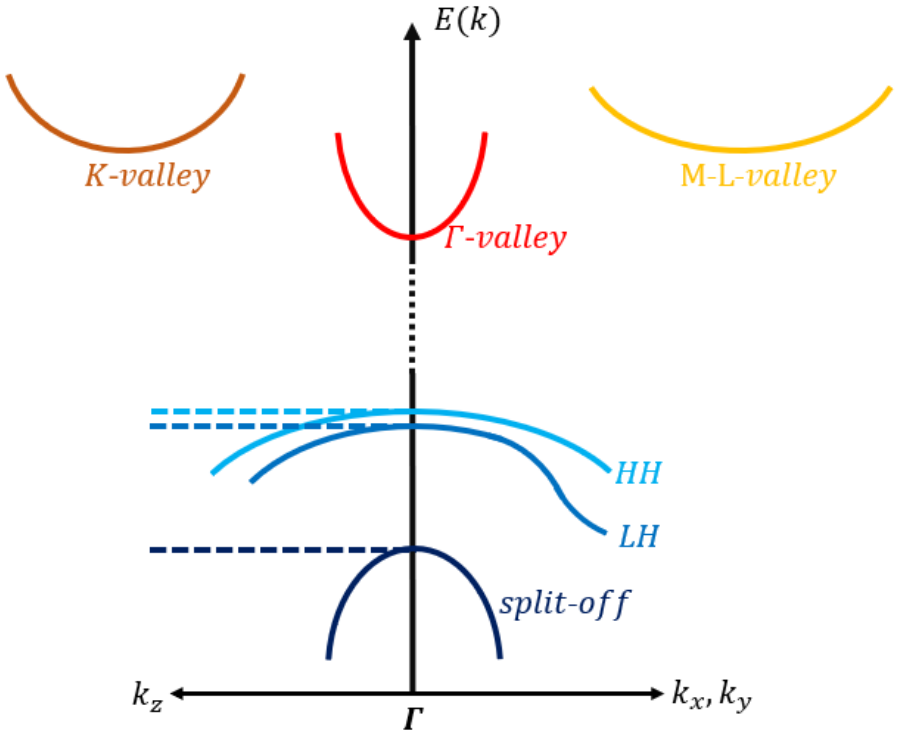


Figure 1.5. Valence band structure of GaN, indicating the anisotropy [61].

Table 1.3. Effective masses of electrons and holes of InN, GaN, and AlN in hexagonal and cubic phases [57].

	InN	GaN	AlN
Wurtzite	$m_e^{\parallel} = 0.12$	$m_e^{\parallel} = 0.20$	$m_e^{\parallel} = 0.28$
	$m_e^{\perp} = 0.12$	$m_e^{\perp} = 0.20$	$m_e^{\perp} = 0.32$
Zinc blende	$m_e^*(\Gamma) = 0.12$	$m_e^*(\Gamma) = 0.15$	$m_e^*(\Gamma) = 0.25$
	$m_{lh}^*(X) = 0.48$	$m_{lh}^*(X) = 0.5$	$m_{lh}^*(X) = 0.53$
	$m_{hh}^*(X) = 0.27$	$m_{hh}^*(X) = 0.3$	$m_{hh}^*(X) = 0.31$
	$m_{SO}^* = 0.3$	$m_{SO}^* = 0.29$	$m_{SO}^* = 0.25$

Regarding the values of the effective masses of holes in nitrides, things are more complicated than for electrons because, according to theoretical results, these effective masses are strongly dependent on the crystallographic direction. For hexagonal GaN, the experimental data are very dispersed: between 0.3 m_0 [62] and 2.2 m_0 [60] (Vurgaftman et al. [57] have done a good review on the field). This uncertainty can in part be explained by the non-parabolicity of the top of the valence band, the effect of stress on the band structure as well as the energetic proximity of the three bands of holes. The experimental measurement could be an "average" of these three components.

1.4. ELASTIC PROPERTIES

III-nitride materials are mainly synthesized on sapphire, SiC, or Si substrates. The lattice and thermal expansion mismatch between substrate and epitaxial layer impose stress on the epitaxial layer which can profoundly affect its optical and electronic properties. The magnitude of the effect depends on the degree of stress. For small stress, the lattice reacts elastically through a shape transition (strain). For large deformations, the relaxation occurs plastically, i.e., introducing dislocations or cracks.

1.4.1. Strain and stress

The stress (σ_{ij}) applied to a material, in a linear elasticity regime, is related to the strain (ε_{kl}) by Hooke's law:

$$\sigma_{ij} = \sum_{kl} C_{ijkl} * \varepsilon_{kl} \tag{1.2}$$

Where C_{ijkl} is the fourth-order elastic tensor.

We introduce the indices 1, 2, 3, 4, 5, and 6, which replace the pairs of indices to simplify the notation, especially that of the fourth-order tensor C_{ijkl},

$$\varepsilon_1 = \varepsilon_{xx} \qquad \sigma_1 = \sigma_{xx}$$
$$\varepsilon_2 = \varepsilon_{yy} \qquad \sigma_2 = \sigma_{yy}$$

$$\varepsilon_3 = \varepsilon_{zz} \qquad \sigma_3 = \sigma_{zz}$$
$$\varepsilon_4 = \varepsilon_{yz}\,, \varepsilon_{zy} \qquad \sigma_4 = \sigma_{yz}\,, \sigma_{zy}$$
$$\varepsilon_5 = \varepsilon_{zx}\,, \varepsilon_{xz} \qquad \sigma_5 = \sigma_{zx}\,, \sigma_{xz}$$
$$\varepsilon_6 = \varepsilon_{xy}\,, \varepsilon_{yx} \qquad \sigma_6 = \sigma_{xy}\,, \sigma_{yx}$$

For hexagonal symmetry, the elastic tensor contains six elastic modules, five of which are independent and $C_{66} = (C_{11} - C_{12})/2$ as illustrated in Eq. (1.2):

$$\begin{pmatrix}\sigma_1\\ \sigma_2\\ \sigma_3\\ \sigma_4\\ \sigma_5\\ \sigma_6\end{pmatrix} = \begin{pmatrix} C_{11} & C_{12} & C_{13} & 0 & 0 & 0\\ C_{12} & C_{11} & C_{13} & 0 & 0 & 0\\ C_{13} & C_{13} & C_{33} & 0 & 0 & 0\\ 0 & 0 & 0 & C_{44} & 0 & 0\\ 0 & 0 & 0 & 0 & C_{44} & 0\\ 0 & 0 & 0 & 0 & 0 & C_{66}\end{pmatrix}\begin{pmatrix}\varepsilon_1\\ \varepsilon_2\\ \varepsilon_3\\ \varepsilon_4\\ \varepsilon_5\\ \varepsilon_6\end{pmatrix} \tag{1.3}$$

Calculated and experimental values of the C_{ij} parameters of GaN and AlN are summarized in Table 1.4.

Table 1.4. Experimental and theoretical constants of InN, GaN, and AlN in GPa.

	C_{11}	C_{12}	C_{13}	C_{33}	C_{44}	References
InN	223	115	92	224	48	[63]
GaN	374	106	70	379	101	[64]
	390	145	106	398	105	[65]
	365	135	114	381	109	[66]
	370	145	110	390	90	[67]
	396	144	100	392	91	[68]
	367	135	103	405	95	[63]
AlN	411	149	99	389	125	[69]
	410	140	100	390	120	[67]
	398	140	127	382	96	[68]
	396	137	108	373	116	[63]

When performing heteroepitaxy of III-nitrides on the (0001) plane, biaxial stress occurs, i.e., the in-plane stress is uniform $(\sigma_{11} = \sigma_{22} = \sigma)$and there is neither stress along with the c-axis nor shear stress. In that particular case (biaxial strain configuration), Hooke's law is simplified:

$$\begin{pmatrix}\sigma\\ \sigma\\ 0\end{pmatrix}=\begin{pmatrix}C_{11} & C_{12} & C_{13}\\ C_{12} & C_{11} & C_{13}\\ C_{13} & C_{13} & C_{33}\end{pmatrix}\begin{pmatrix}\varepsilon_1\\ \varepsilon_2\\ \varepsilon_3\end{pmatrix} \quad (1.4)$$

Due to the lattice symmetry, the strain components ε_1 and ε_2 are equal:

$$\varepsilon_1 = \varepsilon_2 = \varepsilon_{xx} = -(a_{epi} - a_{sub})/a_{sub} \quad (1.5)$$

Where a_{epi} and a_{sub} are the lattice constants of the epilayer, and substrate, respectively. Consequently, the biaxial strain induces a strain ε_3 with the opposite sign of ε_{xx} along the (0001) axis perpendicular to the surface, which is given by:

$$\varepsilon_3 = \varepsilon_{zz} = -2(C_{13}/C_{33})\varepsilon_{xx} \quad (1.6)$$

1.4.2. Spontaneous and Piezoelectric polarization

One of the peculiarities of element III-nitrides is the presence in GaN / AlGaN heterostructures of a strong internal polarization. A signature of the presence of such electrical polarization is the modification of the optical properties of the heterostructure containing quantum wells. The action of the electric field in an InGaN quantum well in GaN was advanced by Hangleiter et al. [70] to explain the shift between the observed exciton transition energy and that expected for a given indium concentration. This effect of the electric field on the optical properties in $GaN/In_vGa_{1-v}N$ heterostructures such as those we have studied will be detailed in the coming papers. This polarization will, of course, modify the electrical properties of the heterostructure: the creation possibility of a 2D gas at GaN / AlGaN interfaces [71]. The next two paragraphs are devoted to the presentation of the origin of the two types of polarization in nitrides.

A. Piezoelectric polarization

Piezoelectric polarization essentially originates from the symmetry of the crystal. The piezoelectric effect can be defined as the appearance of electrical polarization in a semiconductor layer when the latter is subjected to a stress σ which modifies the lattice of the crystal by breaking its symmetry. The opposite effect also exists in some materials, namely a change in crystal lattice volume when electrically polarized. Many devices allowing movements on the nanometer scale operating on this principle are marketed. As we have already mentioned, nitrides can crystallize in two crystalline phases. These two phases: zinc-blende (cubic) and wurtzite (hexagonal) are non-

centrosymmetric. This induces the existence within them of the piezoelectric effect. The appearance of the electric field can be represented by a simple ionic model involving the displacement, under the effect of stress, of the barycenters of positive and negative charges within the tetrahedra forming the crystal lattice. There then appears inside each tetrahedron of the cell an elementary dipole oriented in the direction of the stress as can be seen in Figure 1.6.

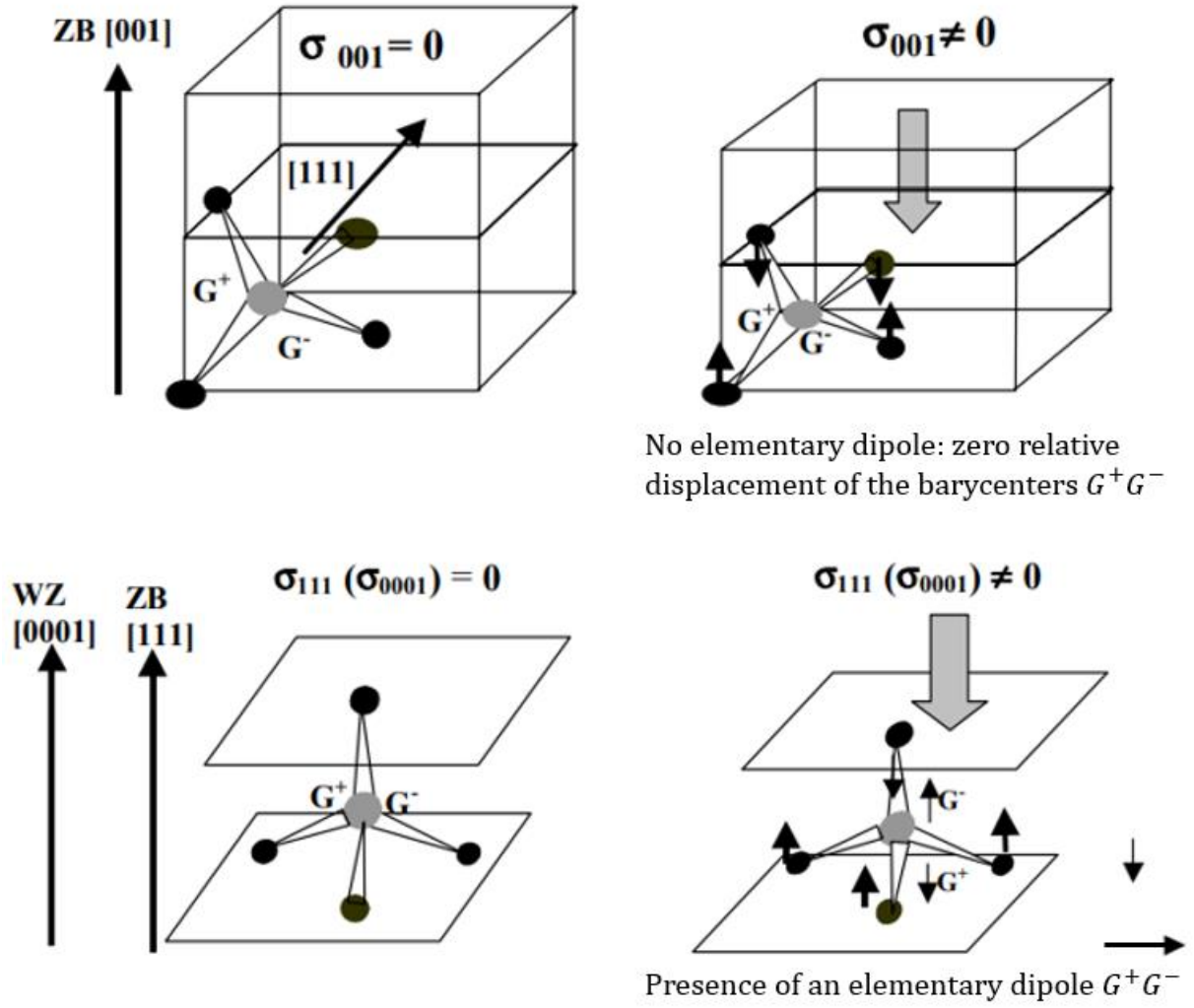


Figure 1.6. Demonstration of the effect of the stress σ in the zinc-blende phase in the direction (001) and (111) as well as in the wurtzite phase in the direction (0001). No polarization is generated in the cubic phase for stress following (001). On the other hand, a stress following (0001) in the hexagonal phase will generate a piezoelectric polarization equivalent to stress (111) in the zinc-blende structure (Figure extracted from the thesis of J. Simon [72]).

It is important to note that the two crystalline phases of nitrides will behave differently when faced with a state of stress.

The stress following the direction of growth (0001) in the hexagonal phase will give rise to a polarization of piezoelectric origin in this direction because the relative displacement of the barycenters of the positive and negative charges is not zero.

As regards the cubic phase, the same phenomenon is observed in the case where the layer is epitaxied in a polar direction such as (111). On the other hand, an epitaxial layer following (001) does not see any polarization appear with stress in this direction. Indeed, the relative displacement of the barycenters of the two types of loads is zero.

We have just highlighted the major difference between the two phases, namely that the epitaxial cubic phase in the (001) direction does not exhibit any piezoelectric polarization. We will show that this gives the cubic layers a definite advantage over the hexagonal phase for the realization of optoelectronic devices.

The value of the polarization of piezoelectric origin can be quantified from the value of the stress present in the layer. We show that polarization can be written in the form:

$$P_i^{pz} = d_{ij} \,.\, \sigma_{jk} \tag{1.7}$$

Where P_i is the piezoelectric polarization in the i direction, σ_{jk} is the tensor of the stresses in the layer and d_{ij} is the tensor of order 3 representing the piezoelectric coefficients specific to the material. These different tensors have several identical or zero elements for reasons of symmetry in the crystal lattice. After simplification, only a piezoelectric component remains along the z-axis of growth for the hexagonal phase. This component is written:

$$P_3^{pz} = 2 \,.\, d_{31} \,.\, \sigma_1 \tag{1.8}$$

The stress tensor sigma1 can be expressed according to the strains in the hexagonal layer thanks to the elastic coefficients of the material in the following way:

$$P_3^{pz} = 2 \,.\, d_{31}.\left(C_{11} + C_{12} + C_{13}.\frac{-2\ C_{13}}{C_{33}}\right)\varepsilon_1 \tag{1.9}$$

Where $\varepsilon_1 = (a - a_0)/a_0$ is the deformation in the plane, with a0 the parameter of the mesh not where constrained and a that of the layer under stress. In the literature many very dispersed values of piezoelectric coefficients are reported, we will simply cite the following references [73–75]. We will conclude on this subject by noting that fields of piezoelectric origin can reach values as high as $10\ MV\ /\ cm$ in nitrides.

B. Spontaneous polarization

In the absence of any stress in a wurtzite nitride layer, however, it can exhibit non-zero macroscopic polarization. The wurtzite structure is the structure of the highest symmetry allowing this phenomenon [73]. This spontaneous polarization is explained in the same way as the piezoelectric polarization, that is to say by a non-superposition of the barycenters of the positive charges with that of the negative charges. This shift between the two barycenters of the loads has two origins:

- The first is the non-ideality of the Wurtzite structure, more precisely the irregularity of the tetrahedra forming the crystal. The distances between atoms with a strong ionic character vary according to the axis of growth, each tetrahedron will therefore have an elementary dipole. These elementary dipoles are added to give the structure a macroscopic spontaneous polarization directed along the axis of growth of the material (0001).
- The second is a reason for the disruption of symmetry in the crystal from the third neighbor. Indeed, the crystal is no longer center-symmetrical from the third neighbor, which generates the creation of an electric dipole following the (0001) direction in the hexagonal phase (see Figure 1.2).

The first contribution is more important than the others.

B. The resulting polarization

According to Bernardini et al. [73], the contribution of spontaneous polarization is comparable to that of piezoelectric polarization in nitrides, and therefore should not be neglected. The total polarization in the nitride layer in the hexagonal phase will then be the result of the sum of the two types of polarization: piezoelectric and spontaneous, it is therefore written:

$$\vec{P} = \vec{P}^{sp} + \vec{P}^{pz} \tag{1.10}$$

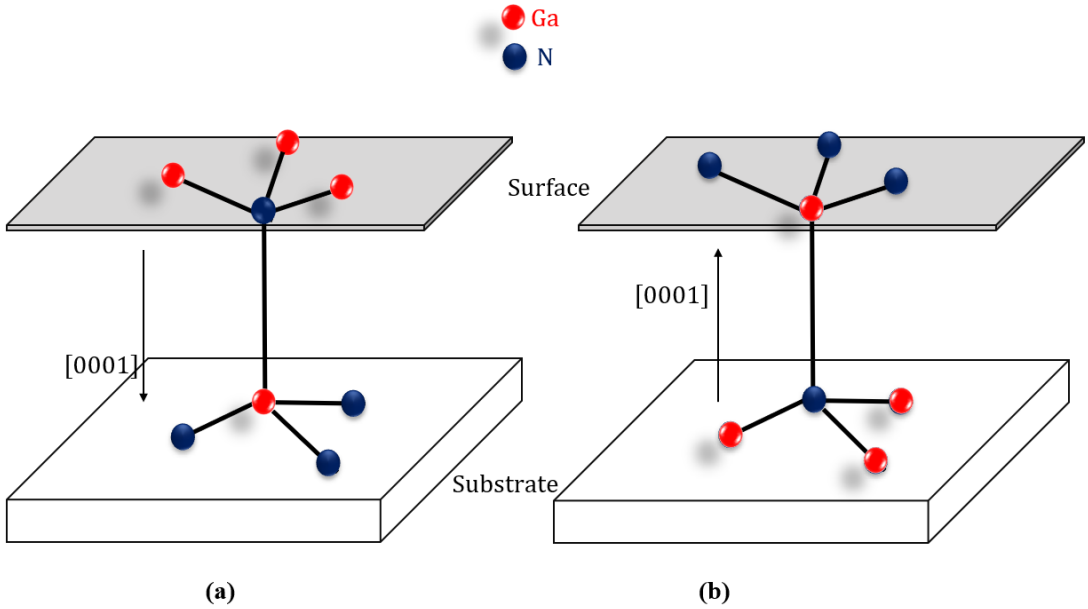


Figure 1.7. The polarity of hexagonal GaN layers. (a): gallium polarity (b) nitrogen polarity. The red and blue spheres indicate Ga and N atoms, respectively.

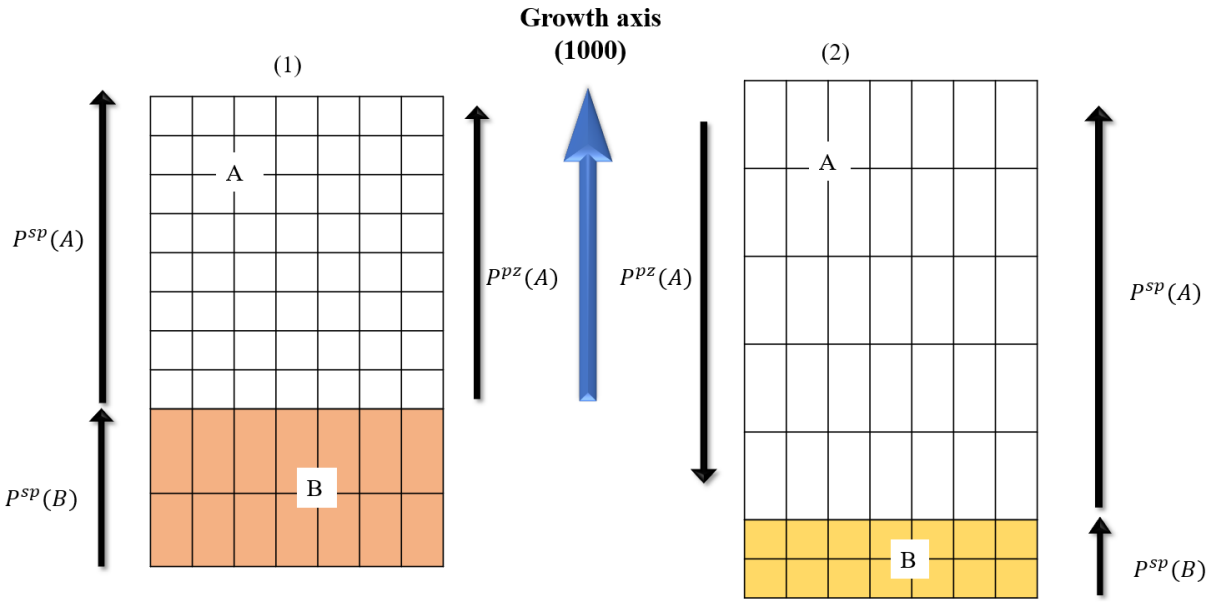


Figure 1.8. Orientation of spontaneous and piezoelectric polarizations for gallium polarity nitrides according to the stress: (1) layer A is in tension on layer B, (2) layer A is in compression on layer.

In hexagonal phase nitrides, one orientation is important: it is the direction of the Ga-N bond along the (0001) direction. This orientation is called the polarity of the layer (see Figure 1.7). The samples we have studied are of gallium polarity.

In nitrides of gallium polarity, the spontaneous polarization is oriented along the direction of growth in the same direction as the latter. As for the piezoelectric polarization, also oriented along the axis of growth. On the other hand, its meaning depends on the type of stress present in the layer. The different possibilities are shown in Figure 1.8.

We have described the origin of the large internal polarization that exists in hexagonal phase nitrides. We have shown that this polarization is absent in the cubic phase when the latter is epitaxial in the (001) direction. This is one of the peculiarities that the cubic phase has compared to the hexagonal phase.

1.5. Structural Defects

Structural defects are any interruption of the crystal translation system and can be classified into point defects, line defects, and planar defects. Point defects are defects generated only at or around a lattice point so that the lattice distortion is rather local. Point defects can be vacancies, interstitial defects, or substitutional defects, as illustrated in Figure 1.9.

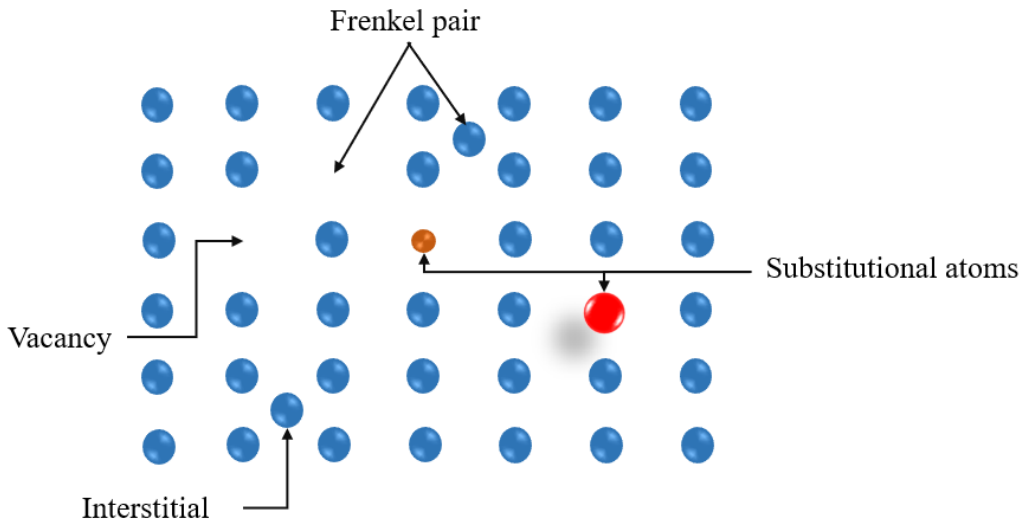


Figure 1.9. Schematic illustration of point defect types in the crystal structure.

Vacancies are lattice sites that should be occupied in the perfect crystal but are vacant. Interstitial defects are atoms that occupy some sites in the structure where; usually; there should not be an atom. A pair of nearby vacancy and interstitial atoms is called Frenkel defect. Substitutional defects are the types of atoms that should not be in the lattice structure but they are in this latter; by occupying the vacant sites in the lattice. Hence, they can be called impurities. Such substitutional atoms can be either smaller (substitutional smaller atom) or larger (substitutional larger atom) than the fundamental atom. The effect of the position of these impurities on nanostructures such as quantum wells is studied in detail in the next chapters.

1.6. RESISTIVITY, MOBILITY, AND CONCENTRATION OF HOLDERS

The concentration of electrons and their mobility are directly related to the resistivity of the layer, measured by the van der Pauw technique, which will be detailed in the next chapter. In GaN, these parameters have been studied by several teams [76,77]. It appears that these parameters vary depending on the thickness of the layer, structural and morphological properties, extensive and point defects, the type of substrate, etc. Mobility is a very important characteristic of the material, as it reflects the ability of wearers to move through the material. It is therefore a determining factor for the devices. This is very important for areas like optoelectronics, or telecommunications. According to the definition of mobility, electron transport depends primarily on two parameters: the effective mass of electrons and the frequency of interactions with the crystal lattice. The average speed of electrons results from two antagonistic interactions: acceleration due to the electric field and diffusion through the crystal lattice. The action of crystal potential is described by the concepts of effective mass; two disturbing effects are added on an ad hoc basis to the action of the crystalline potential. On the one hand, due to thermal agitation, atoms vibrate around their position of equilibrium (phonon), on the other hand, there are local perturbations of the crystalline potential (dopant, alloys, etc.) which are also sources of other types of interactions of carriers with the network. Thus, the various interactions that limit mobility are mainly:

• The interaction with ionized impurities

The ionization of the impurities contained in the crystal leads to the appearance of a Coulomb potential which disrupts the periodic distribution of the crystal potential. Thus, electrons that pass in the vicinity of an ionized impurity find their trajectory altered, which reduces their efficiency in

transporting current, but they retain their kinetic energy (elastic interaction). This interaction has been the subject of several studies, Brooks et al. [78] give the expression of mobility limited by ionized impurities, it varies in Ni -1T 3/2, with Ni the total number. This type of interaction is the most penalizing for mobility at very low levels. low temperatures, and it is all the more penalizing as the number of impurities is high.

• The interaction with neutral impurities

At low temperatures, when the Fermi level of the semiconductor is above the energy level corresponding to an impurity, it will not be ionized. If distortions in the crystal lattice are introduced, there is a break in the periodicity of the lattice. The coupling between carriers and this impurity is not Coulomb. This interaction is present throughout the temperature range and is not predominant in any particular temperature range.

• Alloy diffusion

Due to the disorder of an alloy, the crystal potential is not periodic due to local fluctuations in composition. This phenomenon exists throughout the temperature range, but at low levels, it is masked by other predominant interactions (ionized impurities and optical phonons).

This is often the most detrimental interaction at intermediate temperatures.

• Interaction with phonons

Phonons are distinguished into two categories, depending on the vibrations of atoms: optical phonons, where atoms vibrate in phase opposition, and acoustic phonons, where atoms vibrate in phase. These phonon-electron interactions take place by absorption or emission of phonons while respecting the conservation of energy and the wave vector. We distinguish:

- Interaction with acoustic phonons: With the two types of mechanisms that bring these collisions into play: are acoustic interaction (coupling by deformation of crystal potential) and piezoelectric interaction (Coulomb coupling). Acoustic collisions are elastic shocks the main effect of which is to randomize the direction of the electron velocity vector. These two mechanisms are penalizing for the transport of charges with the application of an electric field. This type of interaction is present throughout the temperature range but seldom prevails.

- Interaction with optical phonons: At low temperatures, the number of phonons is low, and electron-phonon interaction is unlikely. When the temperature increases, the vibrations of the network increase. Thus, the interaction with optical phonons becomes predominant at high temperatures. However, these are the impurities and the temperature.

1.7. TERNARY ALLOYS

The perfectly disordered alloy does not, by definition, have long-range chemical order and translational invariance. Thus, calculating a band structure, based on the periodicity of the crystal, is not entirely correct [57]. However, it is experimentally observed that the alloy has a forbidden band and that the value of the latter varies as a function of the concentration between the two mixed materials. As a first approximation, in an $M_\upsilon M'_{1-\upsilon}N$ alloy, we account for the experimental variation of the gap as a function of the composition x by:

$$E_{g_{M_\upsilon M'_{1-\upsilon}N}} = \upsilon . E_{g_{MN}} + (1-\upsilon) . E_{g_{M'N}} - b \, . (1-\upsilon) \, . \upsilon \qquad (1.11)$$

With b, the bowing parameter, which describes the deviation from linearity. The experimental values of b are generally very dispersed. Indeed, the correct determination of this parameter requires a perfectly disordered alloy (without clusters for example), the composition of which is well determined (by quantitative EDX, with the use of a standard) and without residual stress. Thus, the values of b for $In_\upsilon Ga_{1-\upsilon}N$ and $Ga_\upsilon Al_{1-\upsilon}N$ vary in the literature between 1 and 3.5. In this thesis, it is taken as recommended by Vurgaftman et al. [57]. This bowing term can also be calculated, for example in the case of the virtual crystal approximation (VCA), where all the properties are determined by taking the average of the properties of the pure materials, weighted by their respective concentration. However, a difference with the experimental measurements is observed. Moreover, one notices that this law (Eq. (1.11)) is symmetric compared to $\upsilon = 0.5$, which is a big simplification of the experimental measurements.

This symmetry results from the fact that in virtual crystal approximation (VCA) calculations, it is considered that the excitonic quasi-particle positioned on a given atom feels the average alloy around it. However, the spatial extension of the exciton being limited, it probes a different alloy at each point, linked to the alloy disorder. To account for this statistical disorder, a more rigorous calculation can be undertaken, for example in the approximation of the coherent potential (CPA). This calculation uses as a starting point the properties of each pure constituent using Green's

functions. The gap felt by the quasi-particle is calculated for any composition. One then finds evolutions closer to those observed experimentally, and not necessarily symmetrical compared to $\upsilon = 0.5$. In this thesis, we will therefore keep the simplified model of Eq. (1.11).

1.8. QUANTUM CONFINEMENT

The electronic structure of bulk semiconductors is characterized by the delocalization of electronic states, as well as by an almost continuous energy spectrum in the valence and conduction bands. However, in the case of nanostructured semiconductors, the charge carriers are confined in a restricted region of space, of the order of a few tens of nanometers, which leads, due to quantum confinement, to a remarkable modification of the energy spectrum. In particular, as the size of the semiconductor decreases the bandgap energy increases. On the other hand, the density of states, which describes the electronic states for a given energy, goes from a continuous function of the energy (proportional to $\sqrt{E - E_g}$), in the bulk case, to a discrete function with the appearance of very distinct energy levels in the case of confinement along the three directions of space (Figure 1.10).

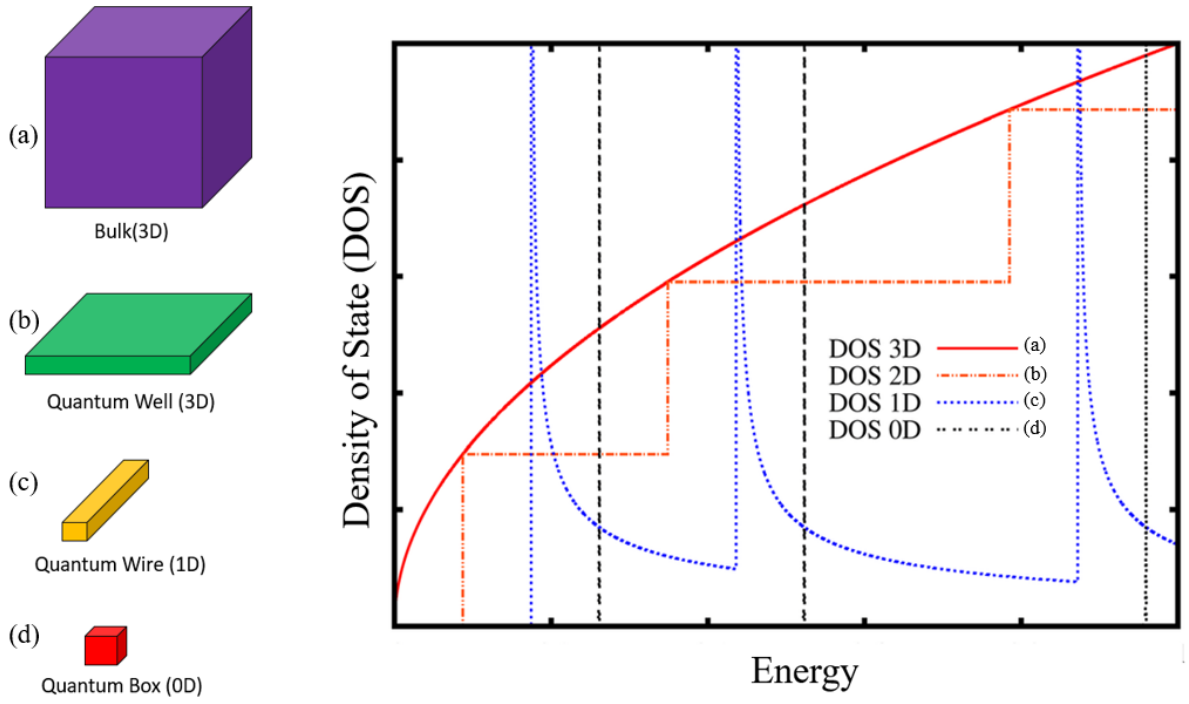


Figure 1.10. Representation of the density of state for a (a) bulk material, (b) quantum well, (c) quantum wire, and (d) quantum box.

In the following, we present an overview of the effect of quantum confinement on the behavior of charged particles in idealized nanomaterial structures.

1.8.1. Quantum Well

We discuss, in this paragraph, the case of a square quantum well. To do this, we will consider a semiconductor (w) as well material sandwiched between two layers of a semiconductor (b) which will play the role of the barrier material (Figure 1.11).

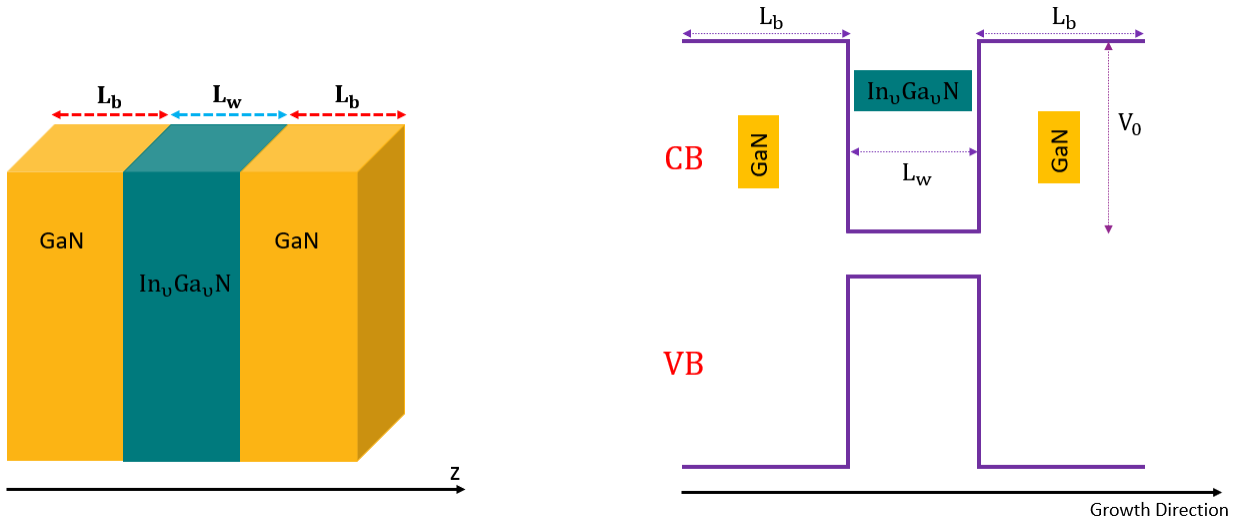


Figure 1.11. Schematic representation of a quantum well. CB and VB are, respectively, the conduction band and the valence band. L_w and L_b are, respectively, the thickness of the well and barrier materials.

Due to the discontinuity of the conduction (valence) bands at the interface between the two materials, a confinement potential appears. It is this potential that is responsible for restricting the movement of electrons (holes) in two spatial directions. In order to go back to the eigen energies of the charge carriers, confined inside a quantum well (QW), we can model, in a simple way, the discontinuity of bands between the two materials by a square potential. Moreover, it has been demonstrated that, for materials with a direct gap (GaAs, InP….), the wave function of the electron can, approximately, take the following form [79,80]:

$$\psi_e(r) = u_{k0}^{A,B}\phi(r) \qquad (1.12)$$

$u_{k0}^{A,B}$, represents the Bloch function at the minimum of the conduction band in the material (w) or (b), while $\phi(r)$ is an envelope function solution of the Schrödinger equation below:

$$\left(-\frac{\hbar^2}{2m_e^*}\Delta + V_{conf.}\right)\phi(r) = \varepsilon\phi(r) \tag{1.13}$$

Where m_e^* is the effective mass of the electron. Since the confinement potential depends only on the growth direction Z, the energies and the eigenfunctions of Eq. (1.13) are written, respectively, as follows:

$$\varepsilon_{\mathbf{k}n} = \frac{\hbar^2\mathbf{k}^2}{2m_e^*} + \varepsilon_n^z \tag{1.14}$$

And

$$\phi_{\mathbf{k}n}(r) = \frac{1}{\sqrt{S}}e^{i\mathbf{k}\rho}\chi_n(z) \tag{1.15}$$

With $\mathbf{k} = (k_x, k_y), k = |\mathbf{k}|, \rho = (x, y),\ S = \mathrm{L_x}, \mathrm{L_y}$, and n is an integer. Therefore, the electron is free to move in the X-Y plane, while it is confined along the Z direction. Therefore, $\chi_n(z)$ obeys the following equation:

$$\left(-\frac{\hbar^2}{2m_e^*}\frac{d^2}{dz^2} + V_{conf.}\right)\chi_n(z) = \varepsilon_n^z\chi_n(z) \tag{1.16}$$

It should be noted that the solutions $\chi_n(z)$ are bound states is less than the value of the potential barrier [81]. In the case of an infinitely deep potential well, $V_{conf.} = 0$ for $-\frac{L_A}{2} \le z \le \frac{L_A}{2}$ and infinity elsewhere, we can write the eigenstates of a confined electron in the following form:

$$\chi_n(z) = \begin{cases} \sqrt{\frac{2}{L_z}}\sin\left(\frac{n\pi z}{L_z}\right) & if\ n\ is\ pair \\ \sqrt{\frac{2}{L_z}}\cos\left(\frac{n\pi z}{L_z}\right) & if\ n\ is\ impair \end{cases} \tag{1.17}$$

And as a result, the application of the connection conditions in $\pm\frac{L_z}{2}$ leads us to eigen energies:

$$\varepsilon_{\mathbf{k}n} = \frac{\hbar^2}{2m_e^*}\left(\frac{n\pi z}{L_z}\right) \tag{1.18}$$

So, we can conclude that the one-dimensional confinement leads to a discretization of the energy along the direction of the confinement. However, in contrast to a smooth square root energy dependence found in bulk materials (Figure 1.10.a), the density of electronic states in a quantum well has the shape of a stair step (Figure 1.10.b), which can be formulated as follows:

$$\rho_{2D}(\varepsilon) = 2\sum_{k_x,k_y,n} \delta\left[\varepsilon - \varepsilon_n^z - \frac{\hbar^2\mathbf{k}^2}{2m_e^*}\right] \tag{1.19}$$

1.8.2. Quantum Wire

In the case of quantum wires, the charge carriers are confined along two spatial directions (X,Y for example). However, their movement along the third direction (Z) is free. So, using a square confining potential, $V_{conf.}(x,y)$ we can transform Eq. (1.13) into a differential equation with separable variables. Thus, the eigenvalues of energy are:

$$\varepsilon_{kn_xn_y} = \frac{\hbar^2k^2}{2m_e^*} + \varepsilon_{nx}^x + \varepsilon_{ny}^y \tag{1.20}$$

while the eigenstates are of the form:

$$\phi_{kn_xn_y}(r) = \frac{1}{\sqrt{L_z}} e^{ikz}\chi_{n_x}(x)\chi_{n_y}(y) \tag{1.21}$$

If we consider, moreover, the case of infinite confinement, the bound states $\chi_{n_x}(x)$ and $\chi_{n_y}(y)$ have the form of Eq. (1.17). On the other hand, the number of states available to an electron in a given energy interval, or more commonly density of states is, in this case, a continuous function varying as the inverse of the square root of the energy (Figure 1.10.c). More precisely, the density of states is written:

$$\rho_{1D}(\varepsilon) = \sum_{n_x,n_y} \frac{L_z}{\pi}\sqrt{\frac{2m_e^*}{\hbar^2}}\sqrt{\left(\varepsilon - \varepsilon_{nx}^x - \varepsilon_{ny}^y\right)} \tag{1.22}$$

and therefore, has a singularity at each band minimum $\varepsilon_{nx}^x + \varepsilon_{ny}^y$. Because the density of states is involved in all physical properties (electronic, optical, magnetic, etc.), two-dimensional confinement allows a remarkable improvement in semiconductor-based devices.

1.8.3. Quantum Dot

The confinement of charge carriers along the three spatial directions gives rise to quantum dots. In this type of confinement, we witness a total discretization of the energy spectrum (Figure 1.10.d). This property is close to that of an atom, for that reason, quantum dots are sometimes called "artificial atoms". In the simple case of a square confinement potential along the X, Y, and Z axes, we can easily arrive at the expressions for the eigenvalues and eigenvectors, of the confined electron, that we formulate them, in this order, as follows:

$$\varepsilon = \varepsilon_{nx}^{x} + \varepsilon_{ny}^{y}\varepsilon + \varepsilon_{nz}^{z} \tag{1.23}$$

And

$$\phi_{n_x n_y n_z}(r) = \chi_{n_x}(x)\chi_{n_y}(y)\chi_{n_z}(z) \tag{1.24}$$

The density of states of a quantum dot is made up of a set of Dirac distributions at the energy of each discrete level:

$$\rho_{0D}(\varepsilon) = 2\sum_{n_x,n_y} \delta\left(\varepsilon - \varepsilon_{n_x n_y n_z}\right) \tag{1.25}$$

This property of quantum dots can be exploited for the realization of logic gates in the field of quantum information. From a physical point of view, the three-dimensional confinement of the carriers in a quantum box gives them unique properties such as the extension of the coherence time or the freezing of spin relaxation mechanisms. In the case of infinite confinement, we have [82]:

$$\varepsilon_{n_x n_y n_z} = \frac{\hbar^2\pi^2}{2m_e^*}\left[\left(\frac{n_x}{L_x}\right)^2 + \left(\frac{n_y}{L_y}\right)^2 + \left(\frac{n_z}{L_z}\right)^2\right] \tag{1.26}$$

1.9. Effective Mass Approximation

It is well known that, in electronic devices, the movement of charged particles is altered by the presence of impurities or, again, due to the application of external fields; electromagnetic field for example. Therefore, the effective mass theory was essentially proposed to study the behavior of charge carriers in a perturbed periodic potential [83,84]. Note that there are two approaches to arrive at the approximation of the effective mass. The first is to introduce the concept of Wannier functions, while the second uses only Bloch functions. Wannier functions are Fourier transforms

of Bloch functions. Consequently, the two approaches are equivalent and will eventually give the same results. On the other hand, the Wannier function $a_n(\mathbf{r};\mathbf{R_i})$ is related to the Bloch function $\psi_{n\mathbf{k}}(\boldsymbol{r})$ by:

$$a_n(\mathbf{r};\mathbf{R_i}) = N^{-1/2}\sum_{\mathbf{k}} exp(-i\mathbf{k}\mathbf{R_i})\,\psi_{nk}(\mathbf{r}) \tag{1.27}$$

or

$$\psi_{nk}(\mathbf{r}) = N^{-1/2}\sum_{\mathbf{k}} exp(-i\mathbf{k}\mathbf{R_i})a_n(\mathbf{r};\mathbf{R_i}) \tag{1.28}$$

$\mathbf{R_i}$ is a vector of the direct lattice, n is an integer, k is the wave vector, and N is the number of elementary cells in the crystal. Note, in passing, that the Bloch functions are indexed by the wave vectors of the reciprocal lattice, while the Wannier functions are indexed by the position vectors of the direct lattice. Therefore, Bloch functions are more convenient for representing delocalized states in crystals, whereas Wannier functions are more suitable for representing localized states[80,85]. Below we present some properties of Wannier functions:

- $a_n(\mathbf{r};\mathbf{R_i})$ is uniquely a function of $\mathbf{r}-\mathbf{R_i}$.
- The Wannier functions, $a_n(\mathbf{r}-\mathbf{R_i})$ form, like the Bloch functions, an orthonormal basis.
- The Wannier functions are eigenfunctions of a "lattice vector operator" $\mathbf{R_{op}}$ defined by:

$$\mathbf{R_{op}}a_n(\mathbf{r}-\mathbf{R_i}) = \mathbf{R_i}a_n(\mathbf{r}-\mathbf{R_i}) \tag{1.29}$$

The effect of $\boldsymbol{R_{op}}$ on a wave function of type:

$$\psi(\boldsymbol{r}) = \sum_{n,\mathbf{k}} A_n(\mathbf{k})\,\psi_{n\mathbf{k}}(\boldsymbol{r}) \tag{1.30}$$

can be approximately represented by:

$$R_{op}\psi(\boldsymbol{r}) \approx \sum_{n,\mathbf{k}}\left(i\frac{\delta}{\delta\mathbf{k}}A_n(\mathbf{k})\right)\psi_{n\mathbf{k}}(\boldsymbol{r}) \tag{1.31}$$

We will now use Eq. (1.30) to simplify the problem of an electron in a crystal subjected to an external perturbation. To do this, we write the wave function $\psi(\boldsymbol{r})$ as a linear combination of Wannier functions:

$$\psi(\boldsymbol{r}) = N^{-1/2} \sum_{n,\mathbf{k}} C_n(\mathbf{R_i})\, a_n(\mathbf{r} - \mathbf{R_i}) \tag{1.32}$$

Thus, the coefficients $C_n(\mathbf{R_i})$, can be considered as the amplitudes of the Wannier functions. We will show later that they are a solution of a wave equation. Hence, they are called envelope functions. Assuming, at this point, that $W_n(\boldsymbol{k})$, are eigenvalues of the unperturbed Hamiltonian $H_0(\mathbf{r})$. Since $\hbar\mathbf{k}$ and R_{op} are conjugate operators in the sense that $\mathbf{R} \leftrightarrow \left(\frac{i\partial}{\partial \mathbf{k}}\right)$ and $\mathbf{k} \leftrightarrow \left(\frac{-i\partial}{\partial \mathbf{R}}\right)$, we can write:

$$\langle n, R_i | H_0(\mathbf{r}) | n', R_j \rangle \leftrightarrow \partial_{nn'} \partial_{ij} W_n(-i\partial/\partial \mathbf{R}) \tag{1.33}$$

To obtain the operator corresponding to the external perturbation, $U_{ext}(\mathbf{r})$, we assume that $U_{ext}(\mathbf{r})$, is a slowly varying function of $\mathbf{r}$ such that the variation of U_{ext} over a lattice constant (a_0) is small compared to U_{ext}:

$$a_0 |\Delta U_{ext}(\mathbf{r})| \ll U_{ext}(\mathbf{r}) \tag{1.34}$$

The elements of the $U_{ext}(\mathbf{r})$ matrix are:

$$\langle n, R_i | U_{ext}(\mathbf{r}) \, | n', R_j \rangle \leftrightarrow \int a_n^*(\mathbf{r} - \mathbf{R_i}) U_{ext}(\mathbf{r})\, a_{n'}(\mathbf{r} - \mathbf{R_j}) / d\mathbf{r} \tag{1.35}$$

Supposing, now, that $\mathbf{r}$ is linked to the primitive cell indexed by the vector of the lattice $\mathbf{R}$, therefore:

$$U_{ext}(\mathbf{r}) = U_{ext}(\mathbf{R}) + (\mathbf{R} - \mathbf{r}) \nabla_{\mathbf{R}} U_{ext}(\mathbf{R}) \tag{1.36}$$

And as a result, by injecting Eq. (1.36) into Eq. (1.35) we get:

$$\begin{aligned} &\langle n, R_i | U_{ext}(\mathbf{r}) | n', R_j \rangle \\ &\quad = U_{ext}(\mathbf{R}) \delta_{nn'} \delta_{ij} \\ &\quad + \nabla_{\mathbf{R}} U_{ext}(\mathbf{R}) \int a_n^*(\mathbf{r} - \mathbf{R_i})(\mathbf{R} - \mathbf{r})\, a_{n'}(\mathbf{r} - \mathbf{R_j}) / d\mathbf{r} \end{aligned} \tag{1.37}$$

So, according to the inequality Eq. (1.34), the second term of Eq. (1.37) can be neglected and the Eq. (1.37) reduces to:

$$\langle n, R_i | U_{ext}(\mathbf{r}) | n', R_j \rangle \simeq \delta_{nn'}\delta_{ij} U_{ext}(\mathbf{R}) \tag{1.38}$$

This allows us to write:

$$\langle n, R_i | H_0(\mathbf{r}) + U_{ext}(\mathbf{r}) | n', R_j \rangle \leftrightarrow \delta_{nn'}\delta_{ij}[W_n(-i\partial/\partial\mathbf{R}) + U_{ext}(\mathbf{r})] \tag{1.39}$$

Finally, the use of Eq. (1.32) and Eq. (1.39) leads us to:

$$[W_n(-i\partial/\partial\mathbf{R}) + U_{ext}(\mathbf{r})] \simeq EC_n(\mathbf{R}) \tag{1.40}$$

Eq. (1.39) can be used to solve the problem of donor impurity. For this purpose, let us place ourselves in the approximation of an isotropic, non-degenerate, parabolic conduction band, having its minimum in the center of the Brouillon zone. Therefore, the energy of the unperturbed electron is:

$$W_n(\mathbf{k}) = E_c(0) + \frac{\hbar^2 k^2}{2m_e^*} \tag{1.41}$$

where m_e^* is the effective mass of the electron in the conduction band, while $E_c(0)$ is the edge of the conduction band. Since we consider only one conduction band, the band index n will be removed.

We point out, however, that this approximation cannot be applied to the study of silicon and germanium, since their conduction band minima are degenerate and are not located in the center of the Brillouin zone. However, these hypotheses are valid for many semiconductors having the zinc-blende structure, such as GaN, AlN, and InN for example.

Now, we substitute the expression for $W_n(\mathbf{k})$, Eq. (1.41), into Eq. (1.40):

$$\left[-\left(\frac{\hbar^2}{2m_e^*}\right)\left(\frac{\partial^2}{\partial\mathbf{R}^2}\right) + \frac{\hbar^2 k^2}{2m_e^*}\right] \simeq [E - E_c(0)]C(\mathbf{R}) \tag{1.42}$$

This leads us to an equality equivalent to the Schrödinger equation of an electron of mass m_e^* moving in a potential U_{ext}. This approach is known as the effective mass approximation. We recall that Eq. (1.42) only allows obtaining the envelope function $C(\mathbf{R})$. This envelope function must be

multiplied by the Wannier function, $a(\mathbf{r}-\mathbf{R})$, in order to arrive at the final expression for the wave function of the electron $\psi(\mathbf{r})$.

1.10. APPLICATIONS OF ELEMENT III-NITRIDES

1.10.1. Light-emitting diodes

Light Emitting Diodes (LEDs) are arguably a set of the major commercial applications for this family of materials. The operating principle of LEDs is based on the inter-band radiative recombination of carriers under the injection of electric current [86]. The first GaN-based luminescent devices appeared in the $1970s$ [87,88]. However, major developments were obtained by S. Nakamura's group within the Nichia company in 1993 [89]. The active structure initially made up of a thick layer of GaN, very quickly evolved into a heterostructure based on InGaN quantum wells [89].

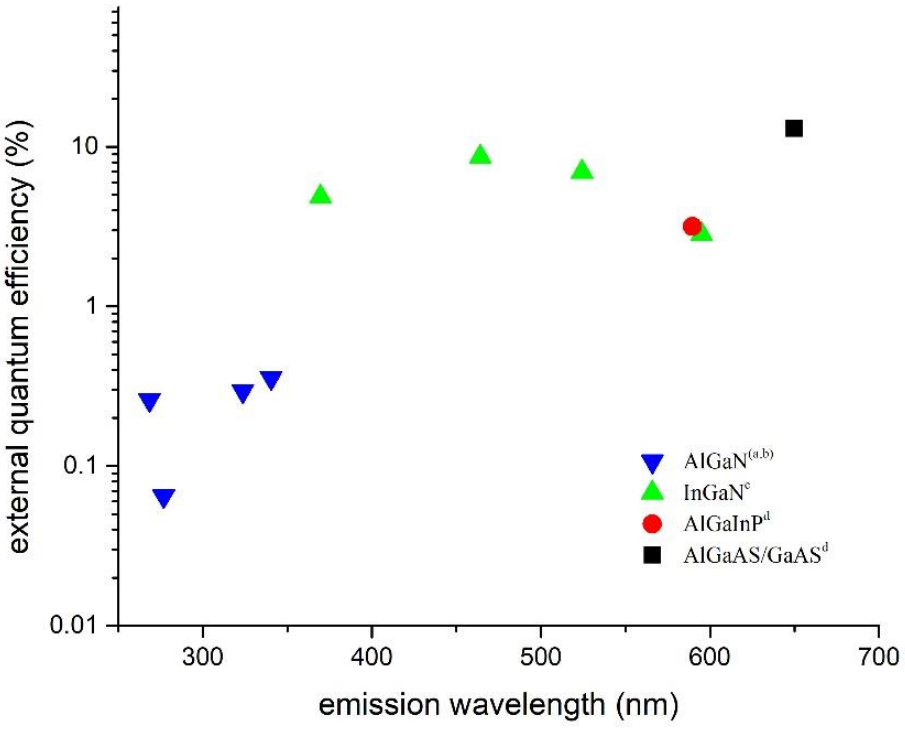


Figure 1.12. Light output (without light extraction) for III-V semiconductor-based diodes, according to: a: [90], b: [91], c: [92], d: [93]).

The wavelengths covered by varying the thickness and composition of the InGaN wells range from near-ultraviolet (380 nm) to yellow and green (600 nm). External quantum efficiency is typically in the order of 10% (see Figure 1.12), but can reach $20-30\%$ with designs that optimize light extraction [94]. The quantum efficiency is very high considering that the dislocation density for sapphire devices is in the order of $108-1010\ /\ \mathrm{cm}^3$ [95] . The commonly accepted explanation today is that carriers are found to be localized to fluctuations in indium-rich composition and are thus less sensitive to non-radiative recombination due to dislocations [96–100].

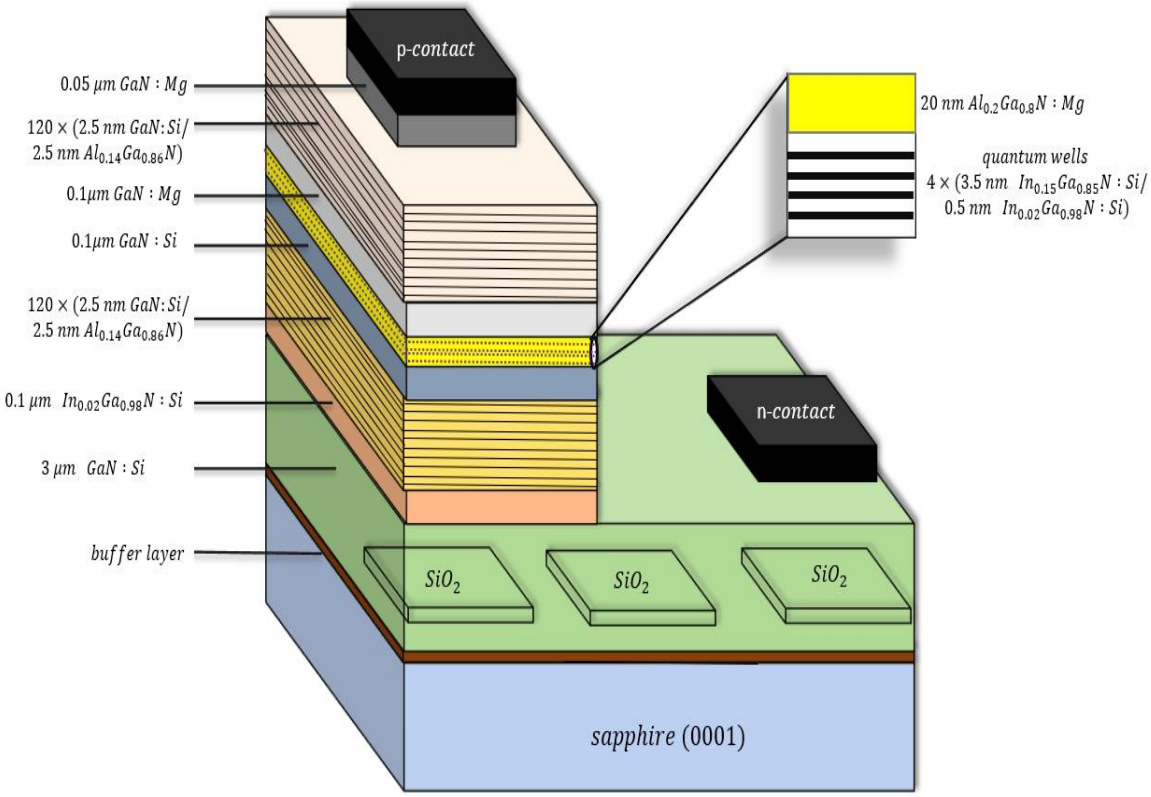


Figure 1.13. Structure of a light-emitting diode [101].

For display applications, the important parameter is light output. It is measured in lm/W and takes into account the response of the human eye which has a maximum at around 555 nm. Typical light output values for InGaN-based LEDs are 10 lm/W in blue and 60 lm / W in green [102].

A big industrial effort is devoted to the development of white diodes which could, in the long term, replace incandescent bulbs and fluorescent lamps. White light can be obtained by combining

the fundamental colors in adequate proportions. The role of nitride heterostructures is to provide blue or ultraviolet light which serves to optically pump phosphors or organic molecules with broadband luminescence [103]. The simplest system uses a combination of two colors (blue and yellow). In Figure 1.13, a simplified diagram of the operation of a blue-emitting LED that optically pumps yellow phosphor is shown. An alternative approach is to use InGaN quantum well stacks with different thicknesses emitting blue and yellow [104]. A three-color system gives a better color temperature but requires the presence of either a blue diode and two phosphors, or three LEDs at different wavelengths [93].

1.10.2. Laser diodes

As for light-emitting diodes, the first demonstration of laser diodes (LD) based on nitrides was given in 1996 by the Nakamura group [89]. LDs operating continuously at room temperature with lifetimes in the order of 10,000 hours find immediate application in data storage on CDs. The use of wavelengths in blue (405 nm for Blu-ray technology) increases the information density by a factor of 4 compared to AlGaAs-based laser diodes operating at 780 nm.

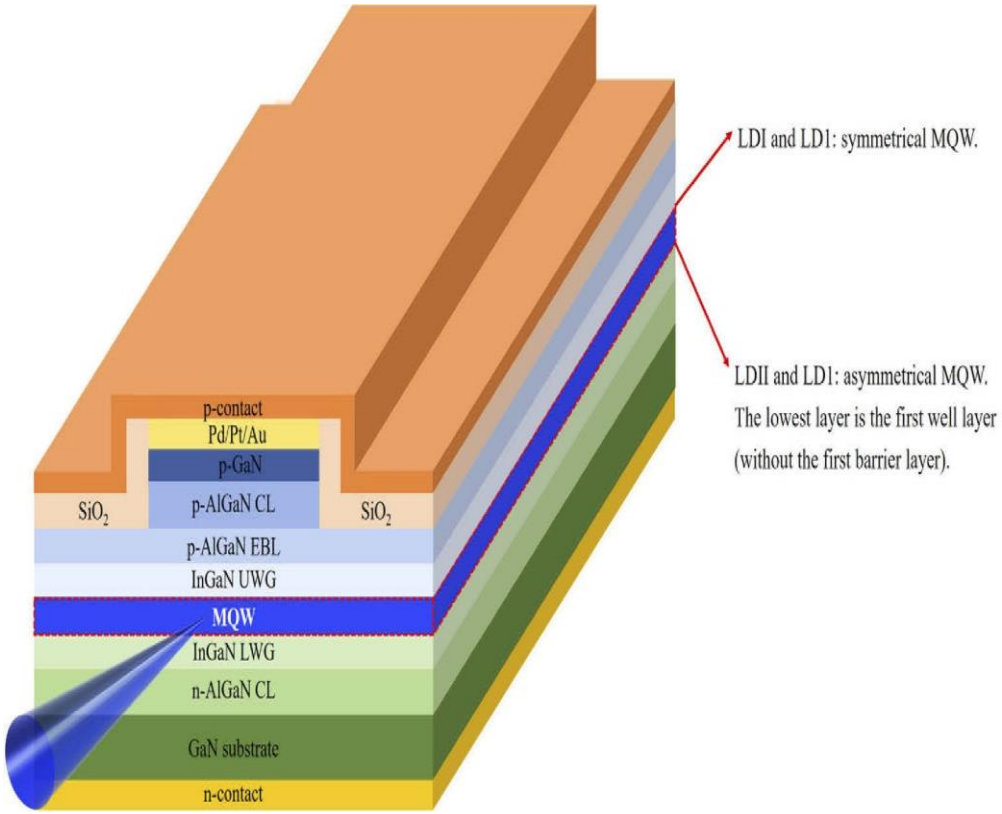


Figure 1.14. Schematic diagram of the structure of the GaN-based LD with different MQWs [105].

As an illustration of the complexity and mastery of the growth techniques required for the development of nitride LDs, Figure 1.14 shows a GaN-based blue LD using symmetrical and asymmetrical multiple quantum wells. Multiple Quantum Well (MQW) as the active area of GaN-based laser diodes is essential for device performance. whose material quality and structural characteristics play a decisive role in the optical performance of LDs.

1.10.3. Ultraviolet photodetectors

In a photodetector, the photons absorbed in the active layer generate electron-hole pairs. The internal potential, in the case of a p-n junction, or the applied voltage gives rise to an electric current proportional to the flow of photons [106]. The different types of detectors used are photoconductors, Schottky photodiodes, M-S-M photodiodes (metal-semiconductor-metal), M-I-S photodiodes (metal-insulator-semiconductor), p-i-n photodiodes (Figure 1.15), etc.[107] .

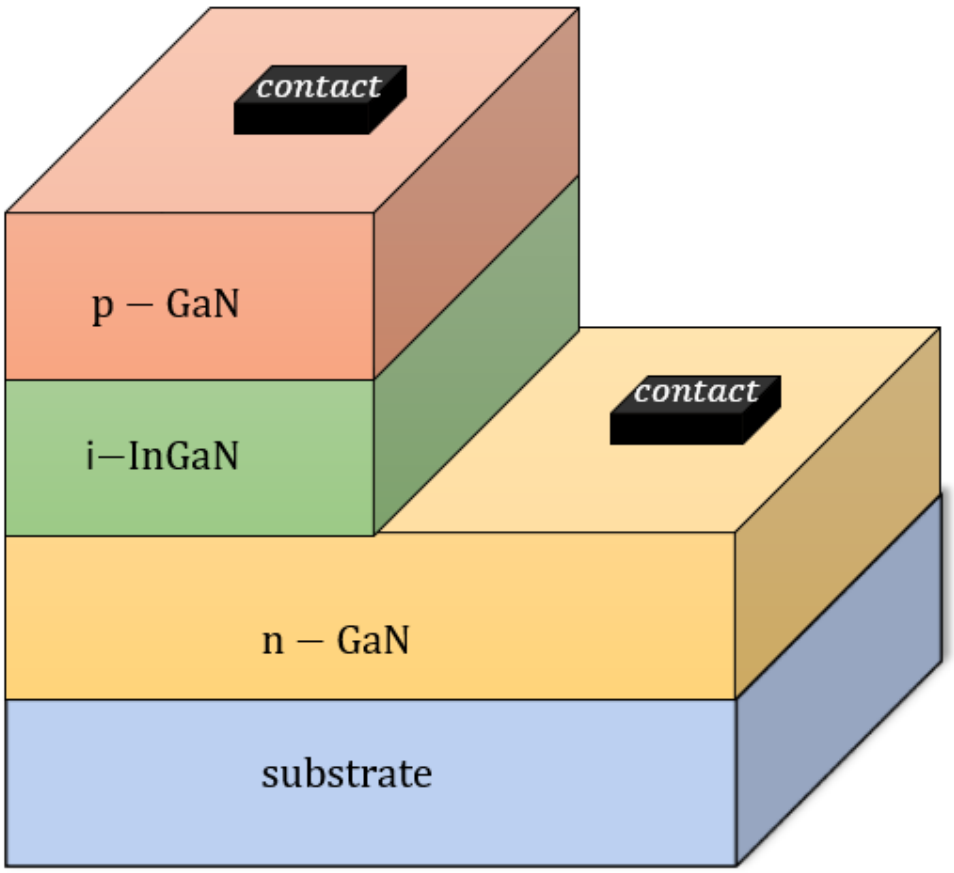


Figure 1.15. Schematic diagrams of non-polar GaN-based p-i-n photodetector [108].

The use of nitrides for photodetectors has advantages linked to good chemical stability, resistance to the effects of radiation, and good thermal conductivity. Aspects that require improvement are crystal quality, wearer mobility, and the development of reliable and reproducible technological processes for device development.

1.10.4. Solar cells

For the past ten years or so, several studies have been carried out on different structures of solar cells based on InGaN. This, as we have already pointed out, is thanks to its wide tunable spectral coverage covering an energy range between 0.7 eV to 3.4 eV and a high absorption coefficient.

Table 1.5. State of the art of InGaN-based solar cells.

Structures	Performance	Realization	References
InGaN-based heterojunction solar cells			
InGaN/GaN (1 sun)	$V_{OC} = 2.4\ V$, $I_{CC} = 3.8\ \mathrm{mA/cm^2}$	MOVPE	[109]
InGaN/GaN (AM0)	$V_{OC} = 1.81\ V$, $I_{CC} = 4.2\ \mathrm{mA/cm^2}$	MOVPE	[110]
Schottky/InGaN/GaN	$V_{OC} = 0.91\ V$, $I_{CC} = 7\ \mathrm{mA/cm^2}$	MOVPE	[111]
InGaN/GaN (AM1.5G)	$V_{OC} = 0.25\ V$, $I_{CC} = 6\ \mathrm{mA/cm^2}$	MOVPE	[112]
P- (MQW) -N heterojunction solar cells based on InGaN			
P-(MQW)-N (AM1.5)	$\eta = 2.9\%$	MOVPE	[113]
P-(MQW)-N (AM1.5)	$\eta = 35\%$	Simulation	[114]
P-(MQW)-N (AM1.5)	$V_{OC} = 1.89\ V$, $I_{CC} = 1.06\ \mathrm{mA/cm^2}$	MOVPE	[115]
P-(MQW)-N (150 sun)	$\eta = 2.31\%$	MOVPE	[116]
P-(MQW)-N (AM1.5)	$\eta = 2.3\%$	MOVPE	[117]
P-(MQW)-N (AM1.5)	$\eta = 3.56\%$	MOVPE	[118]
Homojunction solar cells based on InGaN			
InGaN homo (AM1.5)	$\eta = 31\%$	MOVPE	[119]
InGaN homo (AM1.5)	$\eta = 31\%$	MOVPE	[120]
InGaN homo (AM1.5)	$\eta = 31\%$	MOVPE	[121]
InGaN homo (150 sun)	$\eta = 17\%$	Simulation	[122]
Multijunction solar cells based on InGaN			
InGaN homo (AM1.5)	$\eta = 31\%$	Simulation	[123]
InGaN homo (AM1.5)	$\eta = 35.1\%$	Simulation	[124]
InGaN/GaN MQW (AM1.5)	$\eta = 3.33\%$	MOVPE	[125]

In Table 1.5, we have summarized the state of the art concerning the different structures of InGaN-based solar cells. For each type of structure, we have reported the electrical characteristics of the cell or the efficiency obtained.

1.11. CONCLUSION

In this chapter, we have recalled the main properties of InN, GaN, and AlN binary nitrides in the two types of hexagonal and cubic structures. We have thus demonstrated their enormous potential in the field of optoelectronics for the production of luminescent (LED, laser) or electrical (transistors) devices. Some devices are already on the market and others are about to be. However, most of the studies reported to date have been carried out on the hexagonal phase, which is easier to synthesize. Recent advances in the growth of the cubic phase have rekindled interest in this crystalline phase. With this in mind, we demonstrated that the cubic phase can be an interesting alternative to the hexagonal for the realization of light-emitting diodes as well as heterostructures providing inter-sub-band transitions at telecommunications wavelengths. In the last part of this chapter, the applications of III-N-based semiconductors were summarized.

Chapter 2

QW coupling impact on the binding energy in InGaN/GaN SQW and DQW under internal effects

2.1. INTRODUCTION

Low-dimensional systems (LDS) based on single and multiple quantum wells (SQW, MQW), quantum well wire (QWW), and quantum dots (QD) provide an excellent theoretical and experimental study field. During the last several decades, semiconductor systems based on III-nitrides such as AlN, GaN, (In,Ga)N, and (Al,Ga)N have developed as suitable materials for applications such as solar cells, lasers, and diode lasers. As shown in chapter 1, they have appealing features such as chemical and thermal stability, strong radiation resistance, and high absorption, as well as recent advances in the quality of materials produced using various techniques.

It is well understood that the presence of impurities in such a reduced system has a significant influence on electrical and optical characteristics. It has received a great deal of theoretical and experimental attention in several studies. Mutta et al., for example, used photoluminescence and transmission electron microscopy to investigate several internal and external factors affecting the (In,Ga)N/GaN SQW electronic characteristics. The impact of internal composition on optical characteristics has been described for wurtzite (In,Ga)N/GaN QW. On the SQW, the finite barrier and built-in electric field impacts are explored.

2.2. THEORETICAL APPROACH

We consider a hydrogenic shallow-donor impurity situated at $Z_{\mathrm{i}} = L_b + \frac{L_w}{2}$. The indium fraction in the composite material is denoted ν while L_w is the width of each well and $L_b$is the width of the outer barrier and L_{b1} is the width of the coupling barrier of SQW (DQW) wurtzite structure with $GaN/\mathrm{In_\nu Ga_{1-\nu}N}$ composition. The schematic description of these structures is given in Figure 2.1.

In this manuscript, the results are given in the effective units, i.e., the effective Rydberg energy $\mathrm{R}^*\left(=\frac{\mathrm{m}^*\mathrm{e}^4}{2\hbar^2\varepsilon_0^2}=27.67\ \mathrm{meV}\right)$ as the unit of energy and the effective Bohr radius $\mathrm{a}^*\left(=\frac{\varepsilon_0\hbar^2}{\mathrm{m}^*\mathrm{e}^2}=2.80\ \mathrm{nm}\right)$ as the unit of length.

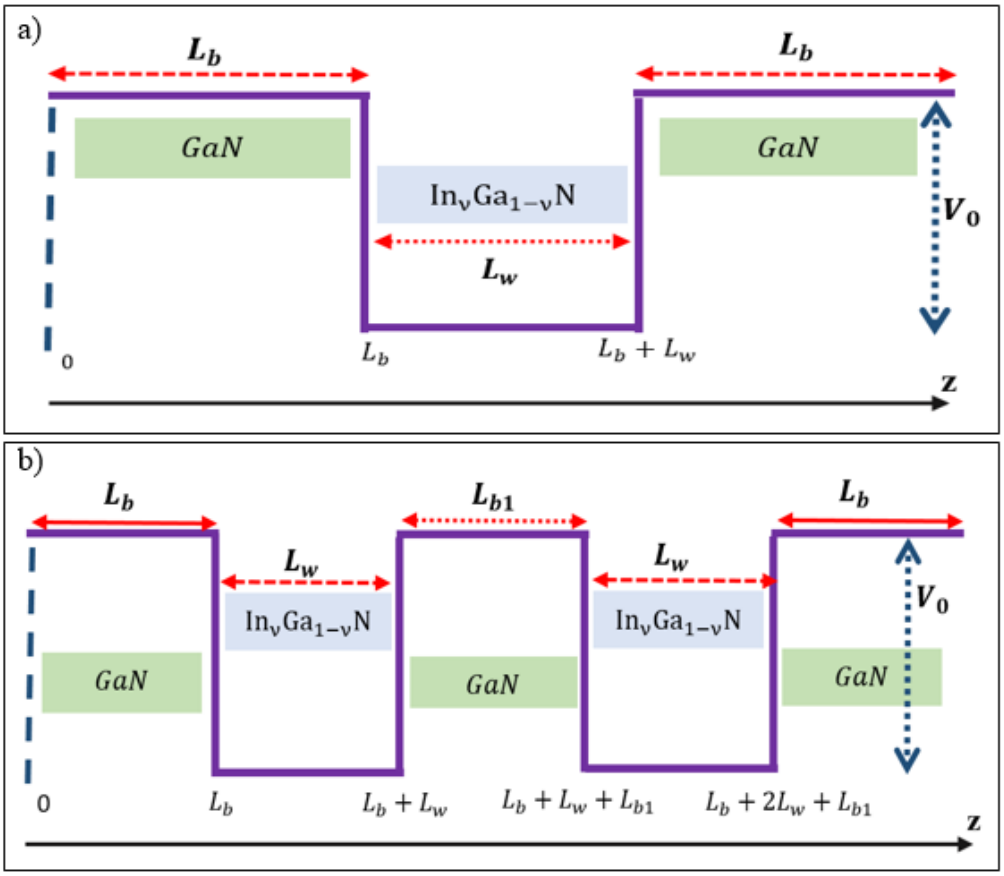


Figure 2.1. Single $GaN/In_vGa_{1-v}N$ QW and double coupled $GaN/In_vGa_{1-v}N/GaN/In_vGa_{1-v}N/GaN$ QWs description under study.

Within the framework of single-band effective-mass and the parabolic band approximations, the Hamiltonian of the electron in the presence of a shallow-donor impurity in structures mentioned in Figure 2.1 can be written as:

$$\mathrm{H} = -\frac{\hbar^2}{2\mathrm{m}^*}\nabla^2 - \frac{e^2}{\varepsilon^*\mathrm{r}} + \mathrm{V(z)} \tag{2.1}$$

e is the electron charge, $|\vec{r} - \vec{r_0}| = \sqrt{x^2 + y^2 + (z - z_0)^2}$ is the electron-impurity distance and V (z) is the finite potential barrier given as:

$$\mathrm{V(z)} = \begin{cases} 0 & \text{well} \\ V_0 & \text{barrier} \end{cases} \tag{2.2}$$

$V_0 = Q.\Delta\mathrm{E_g(v)}$ denotes the height of the potential barrier, whereas Q (= 0.7) [183] and $\Delta\mathrm{E_g}$ are respectively the conduction band off-set parameter and the difference between the band gaps of GaN and $\mathrm{In_vGa_{1-v}N}$ which are defined as follows:

$$\Delta E_g(\nu) = E_g(GaN) - E_g(\mathrm{In_\nu Ga_{1-\nu} N}) \tag{2.3}$$

For $In_\nu Ga_{1-\nu} N$, the band-gap energy is obtained as the interpolation between InN and GaN corrected by the bowing parameter [126] :

$$E_g(In_\nu Ga_{1-\nu} N) = \nu . E_g(InN) + (1-v) . E_g(GaN) - b . (1-\nu) . \nu \tag{2.4}$$

ε and m^* are respectively the main relative dielectric constant and the effective mass. For$(In, Ga)N$, they are equal to the linear combination of those of InN and GaN.

$$m^* = \begin{cases} \nu . m^*_{InN} + (1-\nu) . m^*_{GaN} - b . (1-v) . \nu & well \\ m^*_{GaN} & barrier \end{cases} \tag{2.5}$$

$$\varepsilon^* = \begin{cases} \nu . \varepsilon^*_{InN} + (1-\nu) . \varepsilon^*_{GaN} - b . (1-\nu) . \nu & well \\ \varepsilon^*_{GaN} & barrier \end{cases} \tag{2.6}$$

The electron effective-mass in GaN (InN) is $m^*_{GaN} = 0.19 m_0$ $(m^*_{InN} = 0.1 m_0)$ m_0 is the free electron mass. The mean dielectric constant is $\varepsilon^*_{GaN} = 9.8 \varepsilon_0$ $(\varepsilon^*_{InN} = 13.7 \varepsilon_0)$ for GaN (InN) ε_0 is the static electrical permittivity of the vacuum.

For the dielectric constant at the interfaces, we have used the model as follows:

$$\varepsilon(Interfaces) = \sqrt{\varepsilon(GaN) * \varepsilon(In_\nu Ga_{1-\nu} N)} \tag{2.7}$$

Using the effective units, the Hamiltonian described in Eq. (2.1) becomes

$$H = -\nabla^2 - \frac{2}{r} + \frac{V(z)}{R^*} \tag{2.8}$$

In such a situation, the analytical solution of the Schrödinger equation is impossible. For this reason, we have adopted the finite difference method (FDM) as the mathematical tool to solve $H\Psi = E\Psi$. The ground state binding energy is obtained as follows:

$$E_b = E_0 - E_I \tag{2.9}$$

Where E_I (E_0) is the ground state energy in the presence (absence) of impurity.

The hydrogenic shallow-donor impurity's binding energy in single and double quantum wells based on unstrained wurtzite GaN/(In,Ga)N/GaN is estimated as a function of quantum

well/barrier width, impurity location, and well coupling. The finite element approach is used in our computations.

2.3. EFFECT OF THE STRUCTURE SIZE

Based on theoretical predictions and studies of the microstructure using a variety of electron microscopy techniques [127–131] it is widely believed that indium segregates in InGaN layers during growth, leading to local fluctuations in the band gap that may be effective in localizing injected carriers. It should be noted, however, that well-width fluctuations should be expected to be highly effective as an alternative or additional mechanism for carrier localization in this material system [132–134]. As a result, several qualitative changes in electronic and optical properties are promoted to be properly controlled by adjusting the well/barrier width.

2.3.1. Simple quantum well

To investigate the influence of the well and barrier widths and the impurity position, we have primarily presented in Figure 2.2 the binding energy of wurtzite (In,Ga)N/GaN SQW versus the well width. For all impurity's position and barrier's width, the binding energy increases with

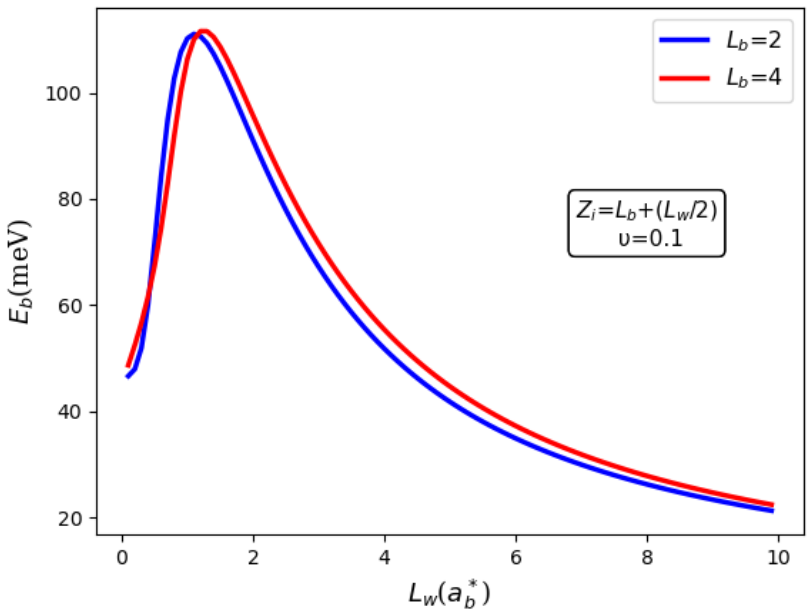


Figure 2.2. Binding energy in GaN/(In,Ga)N/GaN SQW as a function of the well width under the effect of the barrier width.

decreasing the well width until it reaches a maximum corresponding to the critical value (L_w^c) of the well size around the effective Bohr radius. This is due to the diminishing of the electron-impurity distance which enhances the binding energy. For the strong confinement regime (L_w<$L_w^c$the majority of the wave-function is in the barrier region. Therefore, the electron is less attracted by the impurity which is manifested by the reduction of the binding energy tending to the GaN bulk value. According to the same figure, the binding energy shows two behaviors limited by the width critical value. The binding energy drops (augments) with increasing the barrier width for a strong (low) confinement regime. The physical reason is that for strong confinement, the whole of the wave-function is in the barrier and then the barrier width increasing induces more spreading in the barrier which reduces the binding energy. For low confinement, with increasing the barrier width the wave-function spread in the barrier diminishes and then the binding energy can only enhance.

2.3.2. Double quantum well

Binding energy in DQW for two different barrier widths and impurity's position is displayed in Figure 2.3 for a fixed coupling width $L_{b1} = 2$. It is revealed that the behavior of the binding energy in DQW versus the well size is the same as that of the SQW.

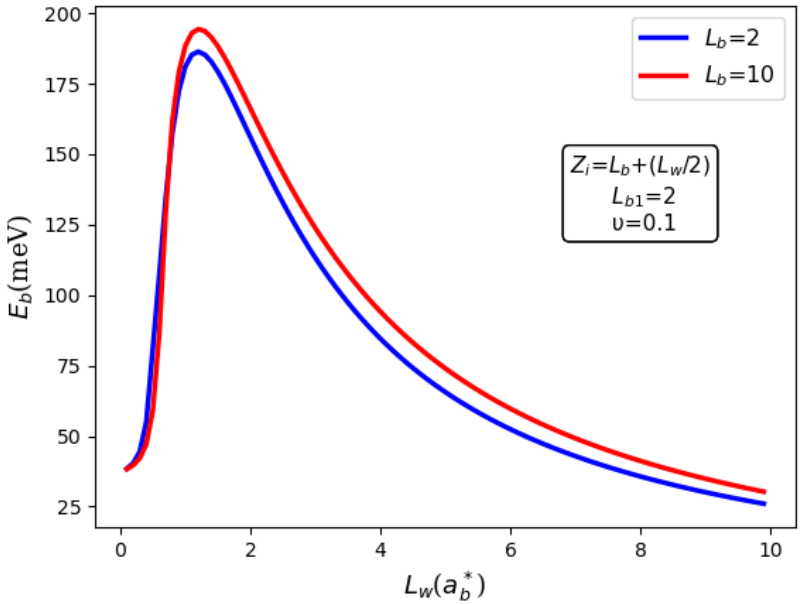


Figure 2.3. Binding energy in GaN/(In,Ga)N/GaN DQW as a function of the well width under the effect of the barrier width.

The principal characteristic is that the binding energy in DQW is greater than that in SQW. This enhancement can be assigned to the coupling effect. For coupling barrier size equals to $L_{b1} = 2$, the improvement rate is about 77%. In the same trend, the impact of the impurity's position is more significant in DQW, particularly for the moderate confinement regime.

2.4. EFFECT OF THE IMPURITY POSITION

It is well known that the impurity in such a reduced system has a great impact on the electronic and optical properties, which may be adequately controlled by choosing the optimum sample geometry and external fields. It is widely studied through several papers [135–140] theoretically and experimentally. The majority of these theoretical calculations were performed for a hydrogenic impurity within the effective-mass approximation and using a variational procedure.

2.4.1. Simple quantum well

Figure 2.4 displays the results concerning the effects of the impurity's position on the binding energy for a fixed value of the barrier width. With the displacement of the impurity far away the

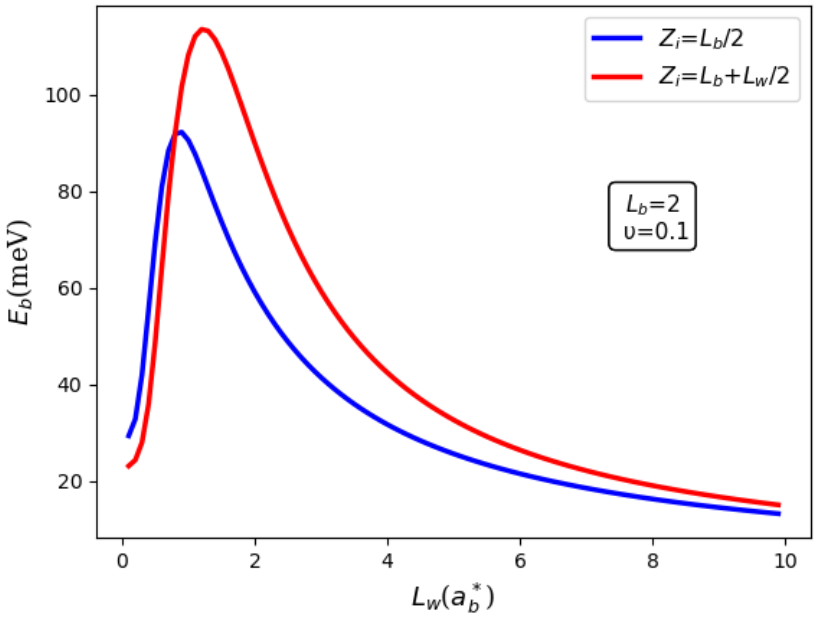


Figure 2.4. Binding energy in GaN/(In,Ga)N/GaN SQW as a function of the well width under the effects of the impurity's position.

structure center the electron-impurity distance increases and therefore the binding energy shows a significant drop. It is clearly seen that this effect is more marked especially in the moderate regime confinement than in the strong one.

2.4.2. Double quantum well

Figure 2.5 contains the variation of the binding energy versus the well width for two different values of the impurity position. It is clearly seen that as the impurity moves from the left barrier to the structure center, the binding energy is strongly enhanced. For instance, the rate enhancement is about 36% when it is moved from L_b to L_b+L_w/2.

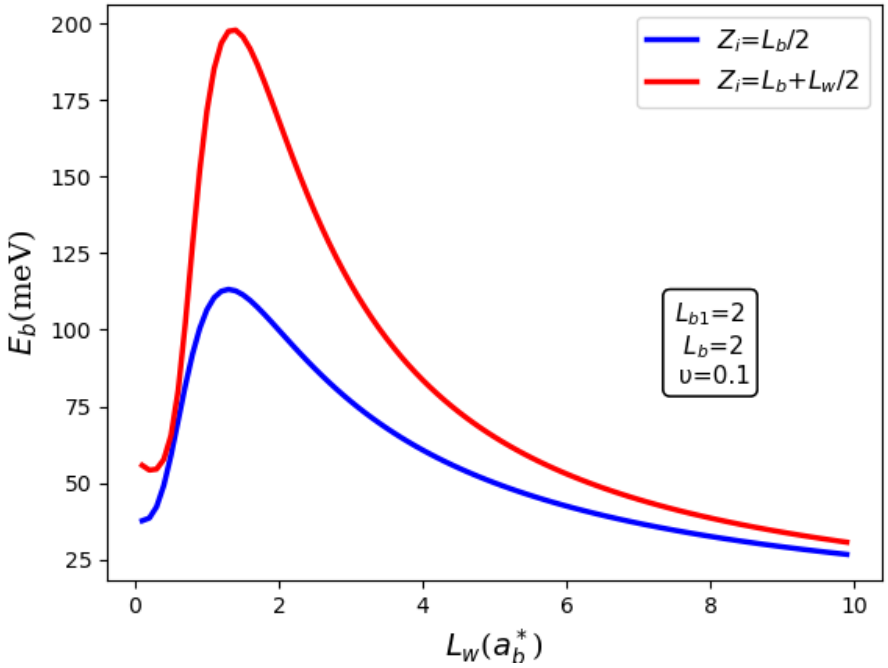


Figure 2.5. Binding energy in GaN/(In,Ga)N/GaN DQW as a function of the well width under the effects of the impurity's position.

2.5. INDIUM COMPOSITION EFFECT IN A DQW

As known, the internal composition of a structure affects the difference between the well and barrier band gaps, which has a great impact on the electronic and optical properties. Figure 2.6 depicts the results corresponding to the ground-state the binding energy in double QWs as a function of the well width under the effects of the In-composition in the well.

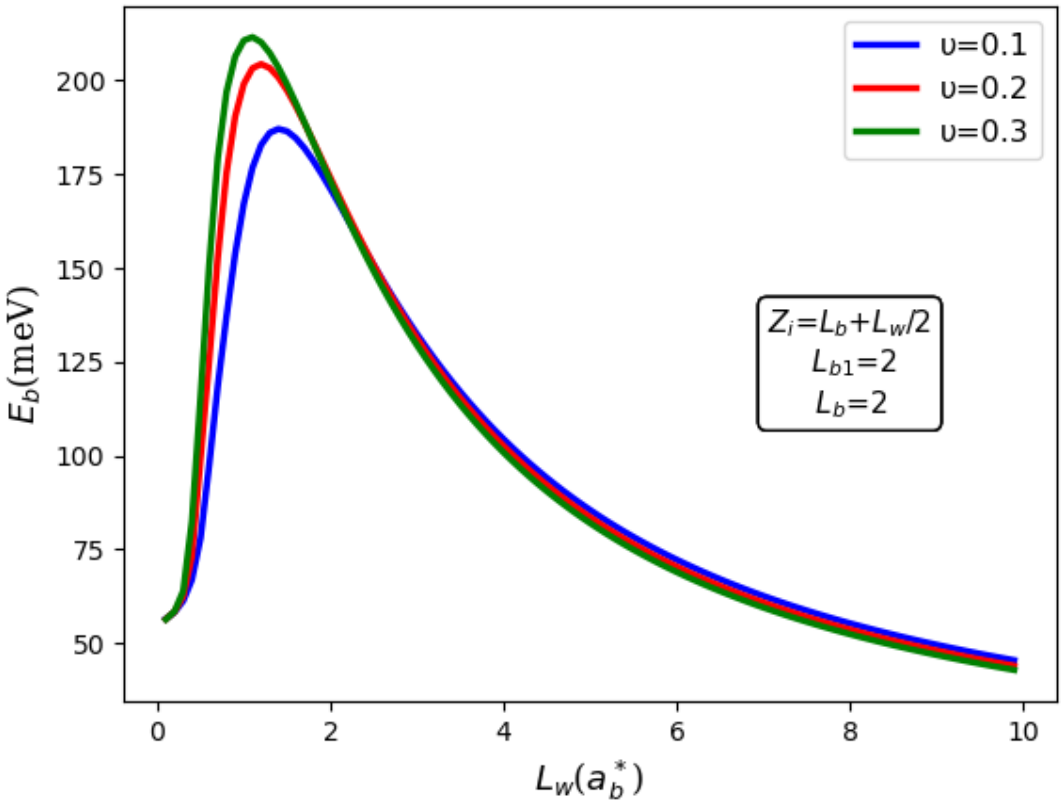


Figure 2.6. Ground-state binding energy according to well width for three different values of the Indium concentrations.

For instance, we have reported the results for $\upsilon = 0.1, 0.2$ and 0.3 for $L_{b1} = L_b = 2$. As expected, two behaviors are obtained. On the one hand, for a low confinement regime, the binding energy drops according to the internal composition. The main reason for this change can be explained by the diminishing of the coupling effect, i.e., the increasing of Indium fraction in the wells leads to the enhancement of the potential barrier which induces more confinement of the electron wave function, and then the binding energy can only go down. On the other hand, for the strong confinement regime, it is found that the binding energy is enhanced versus In-composition in the wells. As known, in such a regime the wave-function is more spread in barriers, so, the In-fraction increasing improves this confinement which enhances the binding energy.

2.6. COUPLING EFFECT IN DQW

The single-particle tunneling probability through the central barrier induces the quantum-mechanical coupling between adjacent wells. As a result, the coupling phenomenon causes a separation of wave-function between left and right wells altering the binding energy.

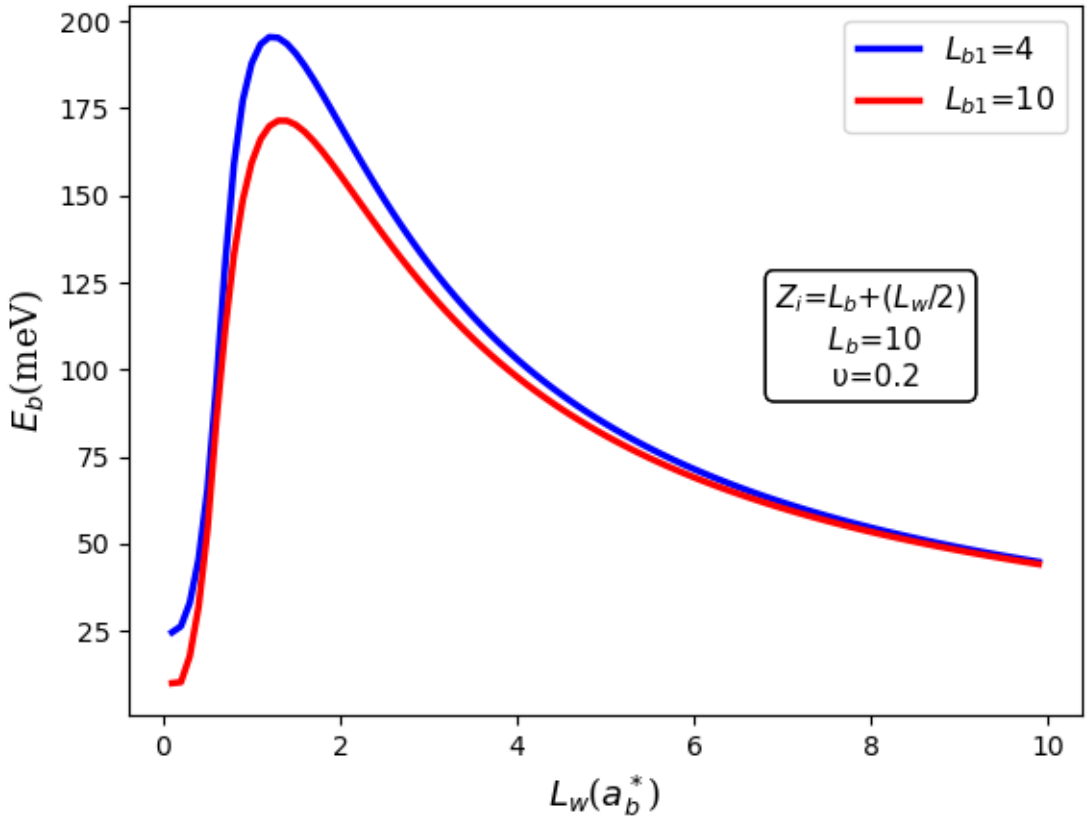


Figure 2.7. Ground-state binding energy in DQW as a function of the well width for two different values of the coupling barrier width.

The variation of the ground-state binding energy in DQW according to well width under the effect of the coupling barrier width is depicted on Figure 2.7. The calculation includes $\upsilon = 0.2$, $L_b = 10$ and $Z_i = L_b + L_w/2$ as fixed parameters and two different values of the intermediate barrier. It is observed that as the coupling barrier width increases the binding energy drops. We notice that the rate drop is about 20 meV representing 12.5% of the binding energy. This result can be assigned to the reduction of the wave-functions overlapping in both wells.

2.7. EFFECT OF NUMBER OF LAYERS

The variation of the ground-state binding energy in SQW and DQW according to well width with fixed parameters for $\upsilon = 0.3$, $L_{b1} = L_b = 2$, and $Z_i = L_b + L_w/2$ is depicted on Figure 2.8. We notice that at the pic of the Eb increase from 122 meV for SQW to 212 meV for DQW representing 74% enhancement of the binding energy. The large binding energy difference between SQW and DQW nanostructures we can observe here shows a strong dependence of the binding energy on the number of layers (well/barrier) in a nanostructure. This enhancement can be assigned to the coupling effect. Furthermore, the critical value (L_w^c) which corresponds to the maximum of the Eb increase from $0.85a_b^*$ for SQW to $1.11a_b^*$ for DQW representing 31% enhancement of the critical value of the well thickness which is a good factor for deposition techniques that cannot go below 1nm such as regular pulsed laser deposition (PLD), etc…

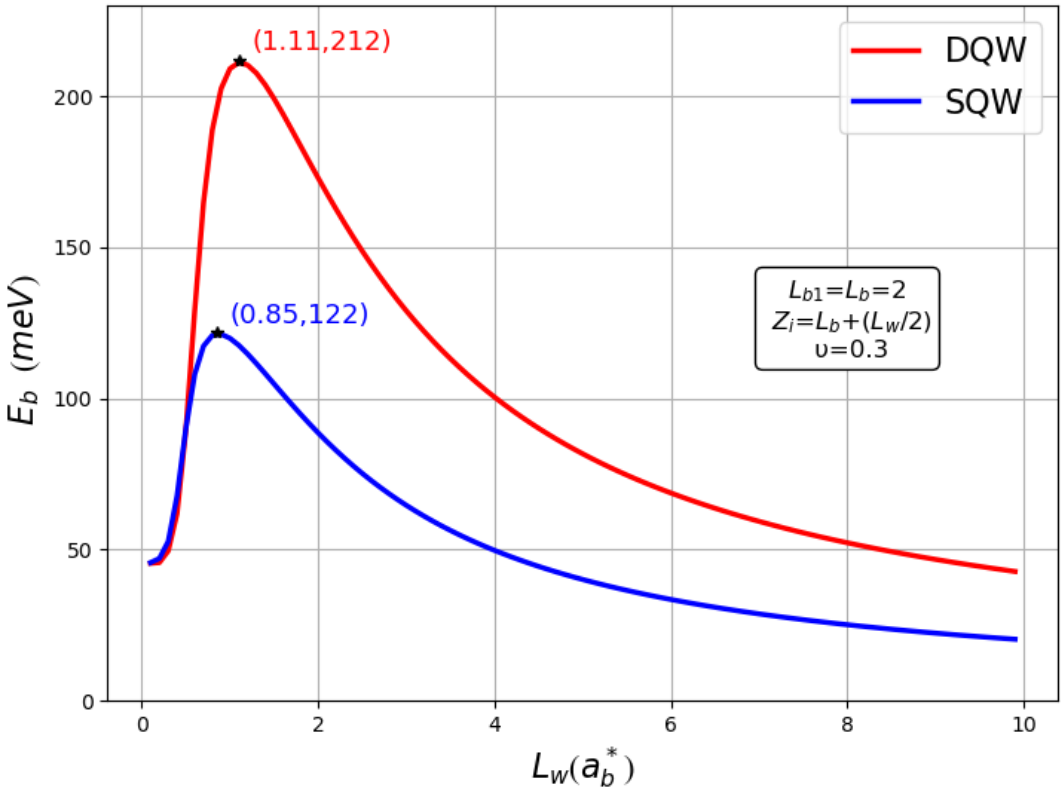


Figure 2.8. Ground-state binding energy in simple and double quantum wells as a function of the well width.

2.8. CONCLUSION

This chapter has been devoted to investigate the effects of the impurity's position, the Indium composition, the structure size and the coupling on the ground-state binding energy in simple and double quantum wells. Based on the finite element method, the wave-function and the energy level are calculated within the framework of the effective mass approximation. The overall conclusion is that the binding energy is strongly depending on these parameters. Depending on the particular nature of the varying internal parameters, we found that:

- The binding energy is enhanced versus the coupling effect.
- The binding energy is reduced as a function of displacement of the impurity far away the structure centre.
- The binding energy is 74% enhanced in DQW compared to SQW, showing a strong binding energy number of layer dependence.
- The In-fraction impact depends on the confinement regime.

Chapter 3

Pressure-related binding energy in (In,Ga)N/GaN DQWs under internal effects

3.1. INTRODUCTION

External factors such as hydrostatic pressure is presented as the effective tools for investigating impurity-related electronic properties in semiconductor QWs. Consequently, it is interesting to take into account of such factor in these structures to control their properties. Hydrostatic pressure alters obviously the donor impurity-states in bulk material and in nanostructures such as QWs, quantum well wire (QWWs), quantum dot (QDs) and quantum ring (QRs) without distorting their crystal symmetry in particularly for low regime. It is well known that the parameters such dielectric constant, effective-mass, band-gap energy, width of QWs are strongly dependent on pressure [141–149]. Then, the energy levels are expected to be strongly influenced with applying the hydrostatic pressure. For instance, Kasapoglu et al. [150] have investigated theoretically the binding energy of shallow-donor in modulated doped as a function of the impurity position under the effects of the electric field.

It is reported that the binding energy presented two different structures for all different values of doping concentrations in particularly for the case without applying external electric field. Additionally, Baskoutas et al. [151,152] have performed theoretical investigation of the electronic and optical properties of ZnO nanorods and QDs versus an externally applied hydrostatic pressure based on the empirical pseudo-potential method. They reported that the applied pressure induces a linear enhancement of the optical band gap. Also, the pressure coefficient is found to be highly size dependent revealing a monotonic increase with increasing QD size.

In almost all previous studies, the calculations have been completed in the framework of effective mass and one-band parabolic approximations using the Ritz-variational and pseudo-potential approaches. However, Finite element method (FEM) and finite difference method (FDM) can be presented as the most powerful techniques originally developed to solve numerically the complex situations based on the PDEs encountered in different domains of engineering sciences. Nowadays, accurate eigen-values and eigen-states of 1D-, 2D- and 3D-nanostructures with different shapes can be obtained compared to variational method.

In this chapter, considering the case of an (In,Ga)N/GaN double quantum well (DQW) structure with a rectangular confinement potential subjected to an external applied hydrostatic

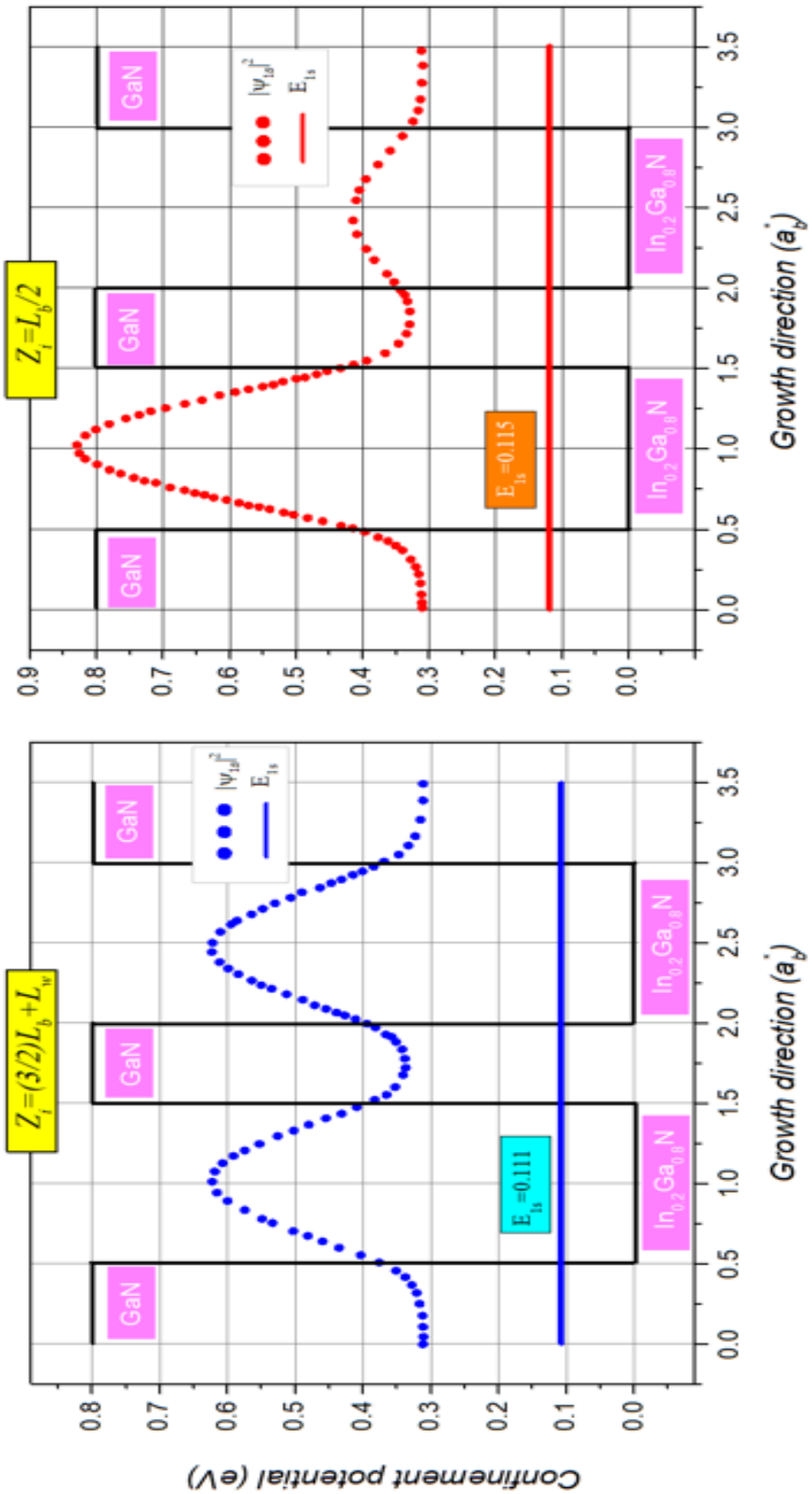


Figure 3.1. The schematic diagrams of double QWs under study based on $(In, Ga)N/GaN - DQWs$. The 1s-like density probability and its corresponding eigen-value are reported for two different values of impurity position for P=0 GPa.

pressure, we will attempt to investigate the influences of hydrostatic pressure, In-composition, structure size and impurity position on the 1s-like binding energy.

3.2. THEORETICAL BACKGROUND

Hydrogenic shallow-donor impurity in a symmetric wurtzite (In,Ga)N/GaN-DQWs is considered. It is worthwhile to point out that the dimension of symmetric DQWs is noticed as and for the barrier and well respectively. The reference of the studied system is located at the left barrier edge and the z-axis is taken to be parallel to the growth direction. The schematic diagrams of the structures under study are shown in Figure 3.1.

The Schrodinger's equation is treated based on the FDM considering the realistic finite potential barrier height and adequate boundary conditions at the interfaces. Using the framework of single-band effective-mass and parabolic band approximations, the electron confined in a rectangular DQW with the presence of a donor impurity located along the growth direction can be described by the Hamiltonian as follows:

$$\mathrm{H} = -\frac{\hbar^2}{2}\vec{\nabla}\left(\frac{1}{m^*(x,z,P)}\vec{\nabla}\right) - \frac{e^2}{\varepsilon^*(x,z,P)\varepsilon_0|\vec{r}-\vec{r}_0|} + V(x,z,P) \tag{3.1}$$

Where e is the electron charge, $|\vec{\mathrm{r}}-\vec{\mathrm{r}}_0|$ is the electron-impurity distance and $V(\nu,z,P)$ is the finite potential barrier given as:

$$V(z) = \begin{cases} 0 & well \\ V_0\,(=Q\Delta Eg(\nu,P)) & barrier \\ 0 & well \end{cases} \tag{3.2}$$

V_0 is the height of the potential barrier while $Q(=0.7)$ and $\Delta Eg(\nu,P)$ are respectively the conduction band off-set parameter and the difference between the band gaps of GaN and $In_\nu Ga_{1-\nu}N$ semiconductor materials.

According to the reference [143], the pressure-dependent band-gap energy is given as:

$$E_g(P) = E_g(0) + \gamma P + \delta P^2 \tag{3.3}$$

For $In_\nu Ga_{1-\nu}N$, the band-gap energy is obtained as the interpolation between InN and GaN corrected by the bowing parameter [141] :

$$E_g(In_\nu Ga_{1-\nu}N) = \nu E_g(InN) + (1-\nu)E_g(GaN) - b(1-\nu)\nu \tag{3.4}$$

Where b is the bowing parameter taking account of bandgap non-linearity as a function of the indium composition. We have used the value ($b = 3.8$) as reported in the recent work [146] .

ε and m^* are respectively the main relative dielectric constant and the effective mass. For$(In, Ga)N$, they are equal to the linear combination of those of InN and GaN.

$$m^*(\nu, z, P) = \begin{cases} \nu m^*_{InN}(P) + (1-\nu) m^*_{GaN}(P) & in\ the\ well \\ m^*_{GaN} & in\ the\ barrier \end{cases} \tag{3.5}$$

$m^*(P)$ is the pressure-dependent effective mass. According to $\vec{k}.\vec{P}$ theory, the pressure-dependent effective-mass is given by the formulas [143] :

$$\frac{m_0}{m^*(P)} = 1 + \frac{C_i}{E_g(P)} \tag{3.6}$$

m_0 is the free electron mass while C is the energy related to the momentum matrix element obtained from the previous equation at $P = 0$ with $m^*(0) = [0.1x + (1-x)0.19]m_0$ which gives $C(GaN) = 14.7$ eV and $C(InN) = 15.50$ eV.

The hydrostatic pressure-dependent static dielectric constant is given as [144] :

$$\varepsilon^*(P) = \left(1 + (\varepsilon_\infty(0) - 1) exp\left[-\frac{5(0.9 - A_0)}{3B_0} P\right]\right)\left[\frac{\omega_{LO}(P)}{\omega_{TO}(P)}\right]^2 \tag{3.7}$$

For the longitudinal and transversal compounds, the pressure dependence of the angular frequency $i \equiv (LO, TO)$ is expressed as:

$$\omega_i(P) = \omega_0(P)\ exp\left[\frac{\alpha_i P}{B_0}\right] \tag{3.8}$$

For the dielectric constant at the interfaces, we have adopted the expression:

$$\varepsilon(Interfaces) = \sqrt{\varepsilon(GaN) * \varepsilon(In_\nu Ga_{1-\nu} N)} \tag{3.9}$$

We notice that the pressure is applied among the z-axis and then the $L(P)$ well/barrier length pressure dependence is given [149] as follows:

$$L_i(P) = L_i(0)[1 - (S_{11} + S_{12})P] \qquad i \equiv (Well, Barrier) \tag{3.10}$$

$L_i(0)$ is the z-direction without pressure effect, while S_{11} and S_{12} are the compliance constants expressed as follow:

$$\begin{cases} S_{11} = \dfrac{C_{11} + C_{12}}{(C_{11} - C_{12})(C_{11} + 2C_{12})} \\ S_{12} = \dfrac{C_{12}}{(C_{11} - C_{12})(C_{11} + 2C_{12})} \end{cases} \tag{3.11}$$

Using the effective units, the Hamiltonian described in Eq. (3.1) becomes:

$$H = -\nabla^2 - \frac{2}{r} + V(z) \tag{3.12}$$

The eigenvalues of the Hamiltonian given in Eq. (3.12) can be obtained with a numerical method using the finite-element method. The ground-state binding energy is obtained as follows:

$$E_b = E_0 - E_I \tag{3.13}$$

Where E_I(E_0) is the ground state energy in the presence (absence) of the impurity.

3.3. RESULTS AND DISCUSSION

Our numerical results are given in the effective units, i.e., the effective Rydberg energy as the unit of the energy and the effective Bohr radius as the unit of length. All used material parameters are listed in Table 3.1. We restrict ourselves to $0 - 40$ GPa pressure range to avoid structural deformation.

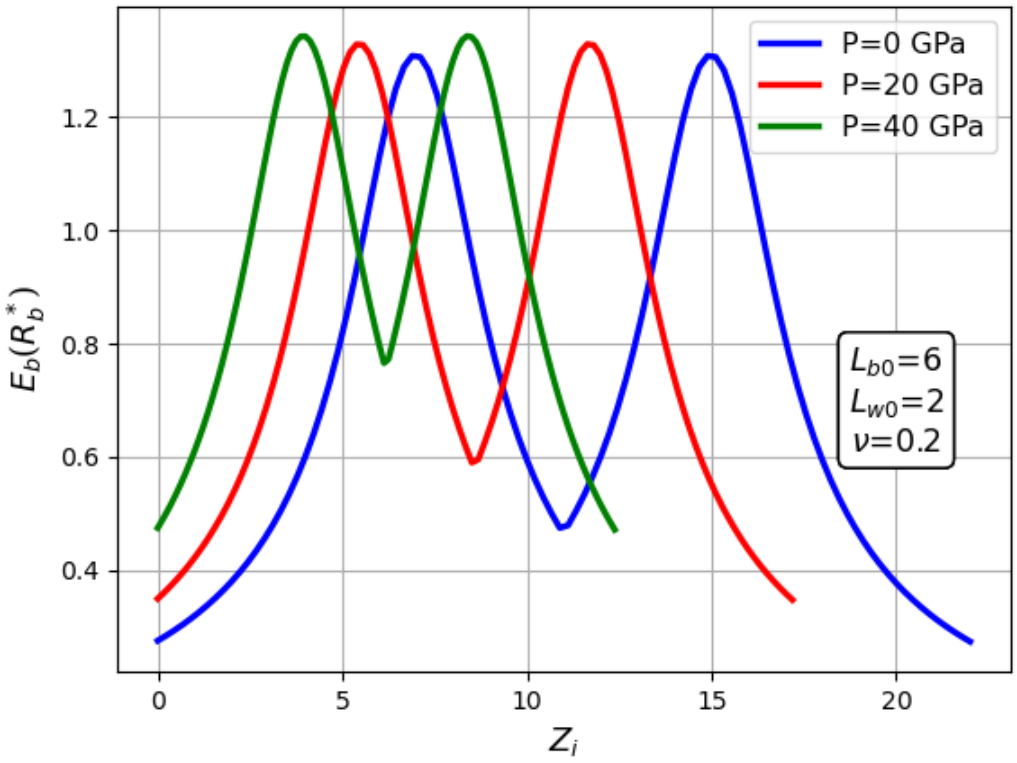


Figure 3.2. The $1s$-like binding energy in $In_{0.2}Ga_{0.8}N/GaN$ DQW versus the impurity position for three different values of the hydrostatic pressure.

To investigate the 1s-like BE, we begin with the presentation of the structure schematic diagram and its rectangular confinement. The results regarding the electron ground-state wave-functions and their eigenvalues are also reported for two different values of the impurity position in Figure 3.1. The electronic wave function is distributed symmetrically and mainly located in the left and right wells for on-center impurity. However, with displacing the impurity far away from the structure center toward barrier one, it is pushed in the same sense and becomes mainly localized in the left well. This can be assigned to the electron-impurity Coulomb attraction. On the other hand, this displacement leads to an electron energy enhancement of about 3.6%.

Table 3.1. Materials parameters used in our calculation.

Parameter	GaN	InN
$E_g(P=0)$(eV)	3.42	0.78
γ(meV/GPa)	40	16
δ(meV/GPa^2)	-0.38	-0.02
C_{11}(GPa)	293	187
C_{12}(GPa)	159	125
$\omega_{LO}(P=0)$(cm^{-1})	731.51	621.53
$\omega_{TO}(P=0)$(cm^{-1})	525.56	487.67
α_{LO}	1.08	1.27
α_{TO}	1.47	1.52
$\varepsilon_\infty(P=0)$	4.942	6.723
A_0	0.365	0.406
B_0	190	136
$\varepsilon(\varepsilon_0)$	9.8	13.7
$m^*(m_0)$	0.19	0.1

To show lighter on the impurity position influences on the 1s-like binding energy in $In_{0.2}Ga_{0.8}N-DQWs$, we display in Figure 3.2 its variation according to Z_i for $L_{b0}=6$ and $L_{w0}=2$. Noticeable modulation of the binding energy becomes perceptible with the displacement of the impurity along the growth axis. The plots don't reveal any obvious qualitative change in their features from that without pressure, except the shift of both structures to impurity position lower values. The said shift originates from the size drop versus hydrostatic pressure according to Eq. (3.10). For instance, the maximum is located at $Z_i=7$ and $Z_i=15$ for $P=0$ GPa which

corresponds respectively to left ($Z_i = L_b + \frac{1}{2}L_w$) and right ($Z_i = 2L_b + \frac{3}{2}L_w$) well centers. Just like the wave function (Figure 3.1), the BE reveals the same behavior according. This is consistent with the results reported by Kasapoglu et al. [150] (For more details: see Figure 3 of Ref. [150]). Furthermore, the observation indicates the presence of a local minimum $Z_i = 11$ corresponding to the structure middle. Also, the plot exhibits a huge enhancement of 1s-like BE minimum as the hydrostatic pressure increase.

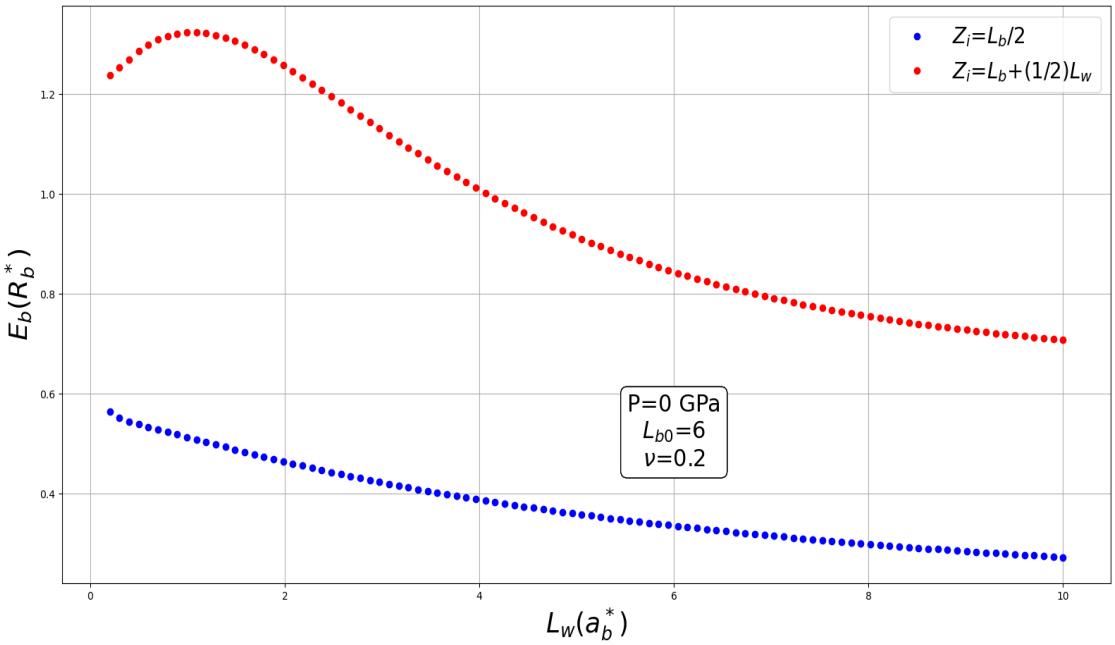


Figure 3.3. The $1s$-like binding energy in symmetric $(In, Ga)N/GaN - DQWs$ as a function of the well width at room temperature for two different positions of the impurity.

In the same trend, Figure 3.3 illustrates the variation of the 1s-like BE in symmetric $(In, Ga)N/GaN - DQWs$ as a function of the well width for two values of impurity position. The main characteristic is that the BE shows two different behaviors limited by a critical value of the well width (L_{wc}). For impurity located in the left well center ($Z_i = L_b + \frac{1}{2}L_w$), it appears that the binding energy presents a maximum for L_{wc}. The aforementioned maximum takes place when the wave-function began to be more spread in the barrier layer. With decreasing L_w ($L_w > L_{wc}$). the wave-function is found to be more confined in the well and then the binding energy increases while for $L_w < L_{wc}$ it began to penetrate more in the barrier which induces a significant diminishing of

the binding energy. However, unlike the previous case, a monotonic BE enhancement is depicted with decreasing the well width for impurity located in the left barrier center. In such a position, the electron wave-function is far away from the impurity and subsequently, with decreasing the well width it becomes closer which enhances the BE without showing any maximum. Additionally, an obvious increase of the BE is visualized as the impurity moves from the left barrier center to the left well one for all well sizes. For a fixed value of well width ($L_w = 4$) the binding energy is equal to $0.4R_b^*$ and $1.02R_b^*$ for two previous cases respectively. This result shows that the BE improvement is about 155%.

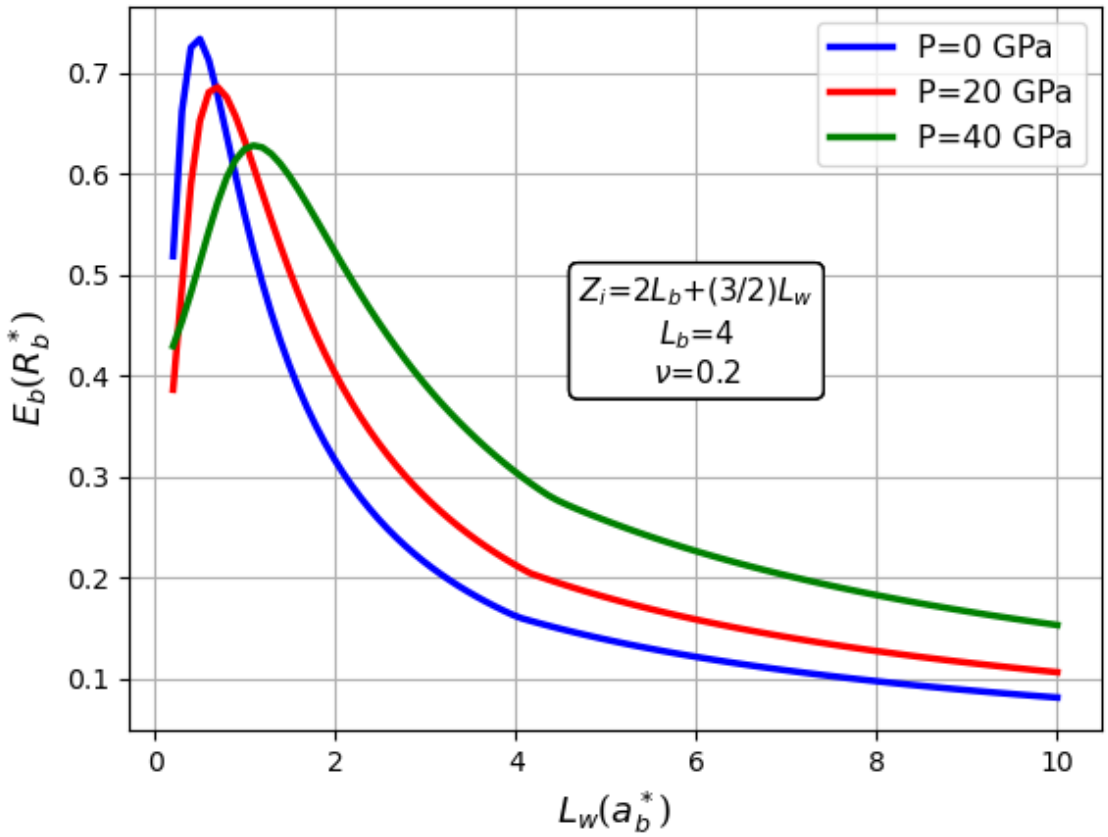


Figure 3.4. The $1s$-like binding energy in (In,Ga)N/GaN-DQWs versus the well width at $T = 300\text{K}$ and $Z_i = 2L_b + \frac{3}{2}L_w$ for three different values of hydrostatic pressure.

We now turn to consider the influence of the hydrostatic pressure on the symmetric $(In, Ga)N/GaN - DQW$ 1s-like binding energy for impurity located in the right well center ($Z_i =$

$2L_b + \frac{3}{2}L_w$). Figure 3.4 shows the variation of the binding energy to the well width for three different values of hydrostatic pressure. The main feature is that the curves show similar behavior for all pressures. The plot exhibits two different behaviors limited by the critical value. A persistent BE increment (decline) is obtained with increasing hydrostatic pressure for large (thin) well. The physical reason can be given as follows: the wave-function is mainly located in the well for $L_w > L_{wc}$ and then the reduction of its size can only improve the BE. However, for $L_w < L_{wc}$, the whole wave function is located in the barrier and the reduction of the well width causes more separation between the electron and impurity provoking a significant drop of BE. It is also found that the BE maximum is dropped whereas the critical value increases with increasing hydrostatic pressure. For instance, the maximum of the binding energy changes from 0.77 to 0.64 showing a substantial decrease of about 17%. At last, the pressure-dependent binding energy is principally related to the effective mass, dielectric constant, and potential barrier changes.

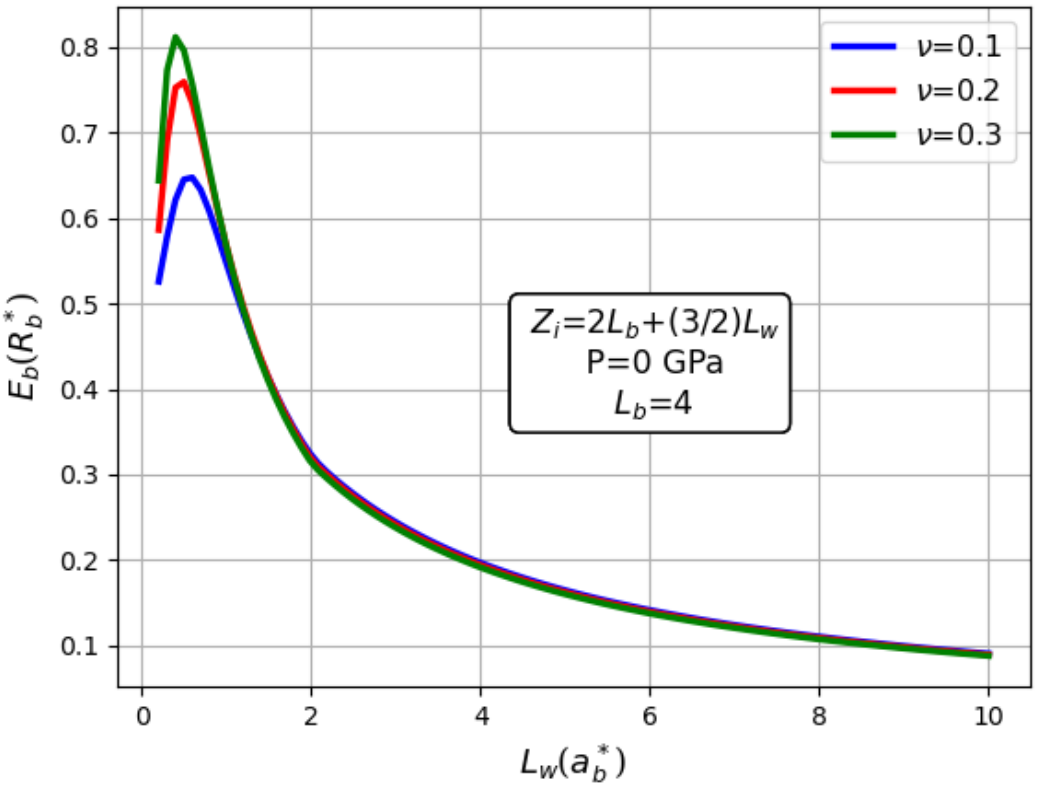


Figure 3.5. The $1s$-like binding energy in (In,Ga)N/GaN-DQWs versus the well width at $T = 300\text{K}$ and $Z_i = 2L_b + \frac{3}{2}L_w$ for three different values of In-composition.

In addition, Figure 3.5 reports the variation of the binding energy according to the well width for three different values of In-compositions. It is seen that the binding energy is insensitive to the increment of the In-composition in particularly for large wells. This reflects that the electronic wave-function located mainly in a large well remains invariably (unperturbed) with increasing the potential barrier height due to In-fraction increasing. On the other hand, a noticeable binding energy increase is obtained for the thin well. Aforesaid increment obtained because a gradually increasing of In-composition enhances the geometrical confinement stopping the spread of the electronic wave-function in the barrier. This effect can only enhance the binding energy.

Moreover, Figure 3.6 describes the variation of the BE as a function of the well width under the effects of the barrier width. It is established that with increasing the barrier width BE falls for all well sizes. The physical basis is due to the coupling phenomenon which diminishes with increasing the barrier width. This reflects somewhat separation of wave-function between left and right wells can alter the BE.

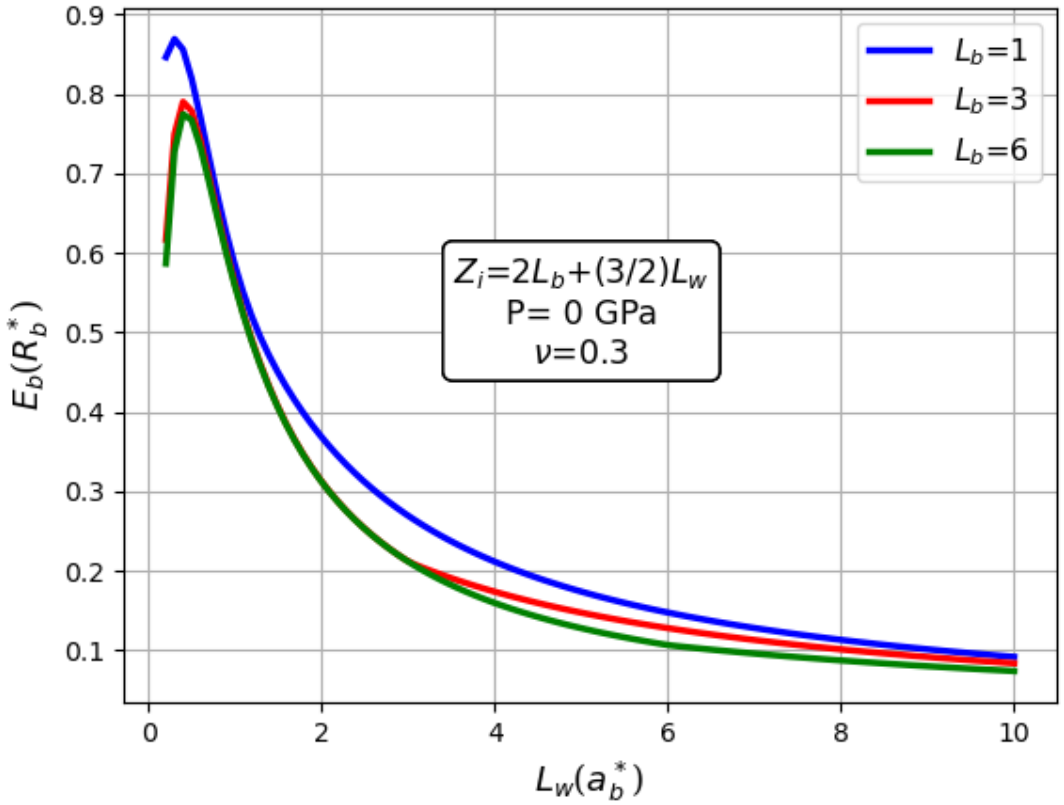


Figure 3.6. The DQW 1s-like binding energy as a function of the well width at room temperature for three different values of the barrier width.

Finally, our obtained results are generally in good agreement with those reported in the literature concerning different low-dimensional nanostructures-shapes based on InGaN QWs [22], $GaAs/Al_{0.3}Ga_{0.7}As$ symmetric double QWs [153] , GaN [154] couple QWs, InGaN couple QDs [31] , $GaAs/Al_{0.3}Ga_{0.7}As$ symmetric DQWs [150] and InGaN coupled QWS [149] . Nevertheless, some discrepancies remain due to the analytical method and structure shape used in each paper. For example, Tianxing et al. [155] have used the same dielectric constant for well (In,Ga)N and barrier (GaN) layers ignoring the mismatch between them for asymmetric multiple QWs.

3.4. CONCLUSION

In summary, the 1s-like binding energy in symmetric (In,Ga)N/ GaN-DQWs is computed according to the well width considering different perturbations such as hydrostatic pressure, barrier size, well chemical concentration, and impurity position. The calculations are performed within the approximations of the effective-mass and one-parabolic band given finite potential barrier height at the interfaces and the mismatches between wells and barriers using the FDM. The pressure- and Indium-dependent binding energy are principally associated with the effective mass, dielectric constant, and potential barrier changes. Our numerical results reveal that the BE:

- is enhanced (dropped) with increasing pressure for large (thin) well,
- decreases as the well coupling increases,
- is quite significant (insensitive) with increasing In-composition for thin (large) well,
- is strongly modulated and conditioned by the impurity position.

Chapter 4

Effect of temperature on the binding energy in InGaN/GaN DQWs for different shapes

4.1. INTRODUCTION

Based on symmetric and asymmetric multiple quantum wells (MQWs) systems, several theoretical papers are reported in the literature, such as double parabolic quantum well (DPQW) [38], double inverse parabolic quantum well (DIPQW) [39], double asymmetric quantum wells (DAQW) [40,41], asymmetric multiple quantum wells (AMQWs) [42]. The effects of external perturbation such as electric field, magnetic field, temperature, and pressure on the physical properties of low dimensional systems constitute a subject of considerable interest from both theoretical and technological point of view, due to the importance of these systems in the development of new semiconductor devices and applications. The temperature effect modifies the energy levels, the masses of carriers, the dielectric constant, the potential barrier, the stability of exciton, and the Γ–X band cross over on the ground-state as well as of some low-lying excited states [156] . The temperature effect has been investigated by Elabsy [157] and Nithiananthi and Jayakumar [158] in a $GaAs/Ga_{1-x}Al_xAs$ quantum well, and R. Khordad [159] in a V-groove $GaAs/Ga_{1-x}Al_xAs$ quantum wire. The electronic properties and strain effects in GaN and InN have also been investigated theoretically [160]. InGaN/GaN multiple quantum wells (MQWs) with high structural and optical qualities have also been successfully fabricated and extensively investigated [161–164]. However, the effect of temperature on shallow-donor-related binding energy in DQWs under an electric field has not been studied enough.

In this chapter, we study the effect of temperature, impurity position, coupling (inner) and side barrier widths on the binding energy of ground state and low-lying excited states in the presence of a hydrogenic impurity in WZ (In,Ga)N/GaN rectangular (DRQW), parabolic (DPQW) and triangular (DTQW) double quantum wells.

4.2. THEORETICAL FRAMEWORK

We are dealing with an on-center hydrogenic shallow-donor impurity in WZ (In,Ga)N/GaN rectangular (DRQW), parabolic (DPQW), and triangular (DTQW) double quantum wells of a height $V_0(\nu, \mathrm{T})$, side barriers width (L_b), coupling barrier width (L_{b1}), and a maximum well width (L_{w}). The description of the nanostructures understudy is included in Figure 4.1, and the corresponding confinement potentials are given in Eqs. (2-4).

The results are given in the effective units, i.e., the effective Rydberg energy $R_b^* \left(= \frac{\mathrm{m}^* \mathrm{e}^4}{2\hbar^2 \varepsilon_0^2} = 27.67 \text{ meV}\right)$ as the unit of the energy and the effective Bohr radius $a_b^* \left(= \frac{\varepsilon_0 \hbar^2}{\mathrm{m}^* \mathrm{e}^2} = 2.80\ nm\right)$ as the unit of length. Within the framework of single-band effective-mass and the parabolic band approximations, the Hamiltonian of the electron in the presence of a shallow-donor impurity in the nanostructures shown in Figure 4.1 can be written as:

$$\mathrm{H} = -\frac{\hbar^2}{2\mathrm{m}^*}\nabla^2 - \frac{e^2}{\varepsilon^* |\vec{\mathrm{r}} - \vec{\mathrm{r}}_0|} + \mathrm{V(z)} \tag{4.1}$$

e is the electron charge, $|\vec{\mathrm{r}} - \vec{\mathrm{r}}_0| = \sqrt{\mathrm{x}^2 + y^2 + (z - z_0)^2}$ is the electron-impurity distance and V (z) is the finite potential barrier given for each profile as:

- rectangular double quantum wells

$$V(z, \upsilon, \mathrm{T}) = \begin{cases} 0, & L_b < z < L_b + L_w \\ 0, & L_b + L_w + L_{b1} < z < L_b + 2L_w + L_{b1} \\ V_0(\upsilon, \mathrm{T}), & Elswhere \end{cases} \tag{4.2}$$

- parabolic double quantum wells

$$\mathrm{V}(z, \upsilon, \mathrm{T}) = \begin{cases} \left(\frac{4}{L_w^2}\right)\left(z - L_b - \frac{1}{2}L_w\right)^2 V_0(\upsilon, T), & L_b < z < L_b + L_w \\ \left(\frac{4}{L_w^2}\right)\left(z - L_b - L_{b1} - \frac{3}{2}L_w\right)^2 V_0(\upsilon, T), & L_b + L_{b1} + L_w < z < L_b + L_{b1} + L_w \\ V_0(\upsilon, T), & Elsewhere \end{cases} \tag{4.3}$$

- triangular double quantum wells

$$\mathrm{V}(z, \upsilon, \mathrm{T}) = \begin{cases} \left(-\frac{2}{L_w}\right)\left(z - L_b - \frac{1}{2}L_w\right) V_0(\upsilon, \mathrm{T}), & L_b < z < L_b + \frac{1}{2}L_w \\ \left(\frac{2}{L_w}\right)\left(z - L_b - \frac{1}{2}L_w\right) V_0(\upsilon, \mathrm{T}), & L_b + \frac{1}{2}L_w < z < L_b + L_w \\ \left(-\frac{2}{L_w}\right)\left(z - L_b - L_{b1} - \frac{3}{2}L_w\right) V_0(\upsilon, \mathrm{T}), & L_b + L_w + L_{b1} < z < L_b + \frac{3}{2}L_w + L_{b1} \\ \left(\frac{2}{L_w}\right)\left(z - L_b - L_{b1} - \frac{3}{2}L_w\right) V_0(\upsilon, \mathrm{T}), & L_b + \frac{3}{2}L_w + L_{b1} < z < L_b + 2L_w + L_{b1} \\ V_0(\upsilon, \mathrm{T}), & Elswhere \end{cases} \tag{4.4}$$

$V_0(\nu, \mathrm{T}) = Q * \Delta Eg(\nu, T)$ is the height of the potential barrier while Q(=0.7) and $\Delta Eg(\nu, T)$ are respectively the conduction band off-set parameter and the difference between the band gaps of GaN and $In_\nu Ga_{1-\nu}N$ semiconductor materials.

According to the Ref. [165], the Temperature-dependent band-gap energy is given as:

$$E_g(T) = E_g(0) - \frac{\alpha * T^2}{T + \beta} \tag{4.5}$$

For $In_\nu Ga_{1-\nu}N$, the band-gap energy is obtained as the interpolation between InN and GaN corrected by the bowing parameter (b=1.40) [166] :

$$E_g^{In_\nu Ga_{1-\nu}N}(\nu, T) = \nu E_g^{InN}(T) + (1-\nu)E_g^{GaN}(T) - b(1-\nu)\nu \tag{4.6}$$

where E_g^{InN} and E_g^{GaN} are respectively the band-gap energies of InN and GaN, while b is the band-gap bowing parameter taking account of bandgap non-linearity as a function of the indium composition.

Several parameters of III-nitrides are reported in many experimental and theoretical works, the bandgap energy of GaN and InN at T= 0K is also reported in the literature. In this chapter, we have used those obtained by Vurgaftam et al. [141] which are listed in Table 4.1.

Table 4.1. Parameters used in the computation.

	$E_g(0\ \mathrm{K})$ (eV)	α ($\mathrm{meV.K^{-1}}$)	β (K)	$\varepsilon^*(300\ K)$ (ε_0)	C (eV)
GaN	3.299	0.909	830	9.8	14.07
InN	0.78	0.245	624	13.7	25.50

The indium composition dependence of $In_\nu Ga_{1-\nu}N$ electron mass is calculated by linear interpolation between GaN and InN. It is given as:

$$m^*(v,T) = \begin{cases} \nu m^*_{InN}(T) + (1-\nu)m^*_{GaN}(T) & in\ the\ well \\ m^*_{GaN}(T) & in\ the\ barrier \end{cases} \tag{4.7}$$

$m^*(T)$ is the temperature-dependent effective-mass. According to $\vec{k}.\vec{P}$ theory, the temperature-dependent effective-mass is given by the formulas [167] :

$$\frac{m_0}{m^*(T)} = 1 + \frac{C}{E_g(T)} \tag{4.8}$$

$E_g(T)$ is the band-gap temperature dependency, m_0 is the free electron mass while C is the energy related to the momentum matrix element, and it is a constant for each material.

The values of the dielectric constants $\varepsilon_r(T)$ for GaN and $In_\nu Ga_{1-\nu}N$ versus the temperature are approximated by [168] :

$$\varepsilon_{GaN}(T) = \varepsilon_{GaN}(300K) * exp\big((T-300) * 10^{-4}\big) \tag{4.9}$$

$$\varepsilon_{In_\nu Ga_{1-\nu}N}(T) = \varepsilon_{GaN}(T) + 6.4 * \nu \tag{4.10}$$

At the interface between the well and the barrier, there is an overlap between GaN and InGaN materials. Thus, as we adopted in recent work [169] the dielectric constant at the interfaces is expressed as follows:

$$\varepsilon_{Interfaces} = \sqrt{\varepsilon_{GaN} * \varepsilon_{In_\nu Ga_{1-\nu}N}} \tag{4.11}$$

Using the effective units, the Hamiltonian described in Eq. (4.1) becomes:

$$H = -\nabla^2 - \frac{2}{r} + V(z) \tag{4.12}$$

Using the finite-element method with a numerical method, the eigenvalues of the Hamiltonian given in Eq. (4.12) can be calculated. The binding energy of a hydrogenic impurity is known as the difference between the energy states without impurity and with impurity for a particular state.

4.3. Numerical Results and Discussion

In this section, we present numerical results for the temperature, size, impurity position and coupling effects on the ground state, first and second excited states in finite InGaN/GaN rectangular (DRQW), parabolic (DPQW) and triangular (DTQW) double quantum wells.

In order to facilitate the interpretation of the binding energy results, we have presented primarily the probability densities of all states in Figure 4.1. The main common characteristic is the fact that the electronic wave-functions are symmetrically distributed. In addition, the ground and first excited states are mainly located in the wells (InGaN regions) while the second excited one is principally located in the barrier (GaN) especially for rectangular-shape. However, for parabolic and triangular shapes, the states are located in the barriers due to the strong confinement compared to rectangular profile.

In Figure 4.2, we present our computed results for the ground, first and second excited states energies in the presence (a) absence (b) of the impurity for different In.1Ga.9N/GaN DQW-shapes versus the well width. These results are obtained for T = 0, 300 and 900 K and ($L_b = 1,\ L_{b1} =$ 1.5). As illustrated by these figures, for a fixed temperature the electron-energy monotonically

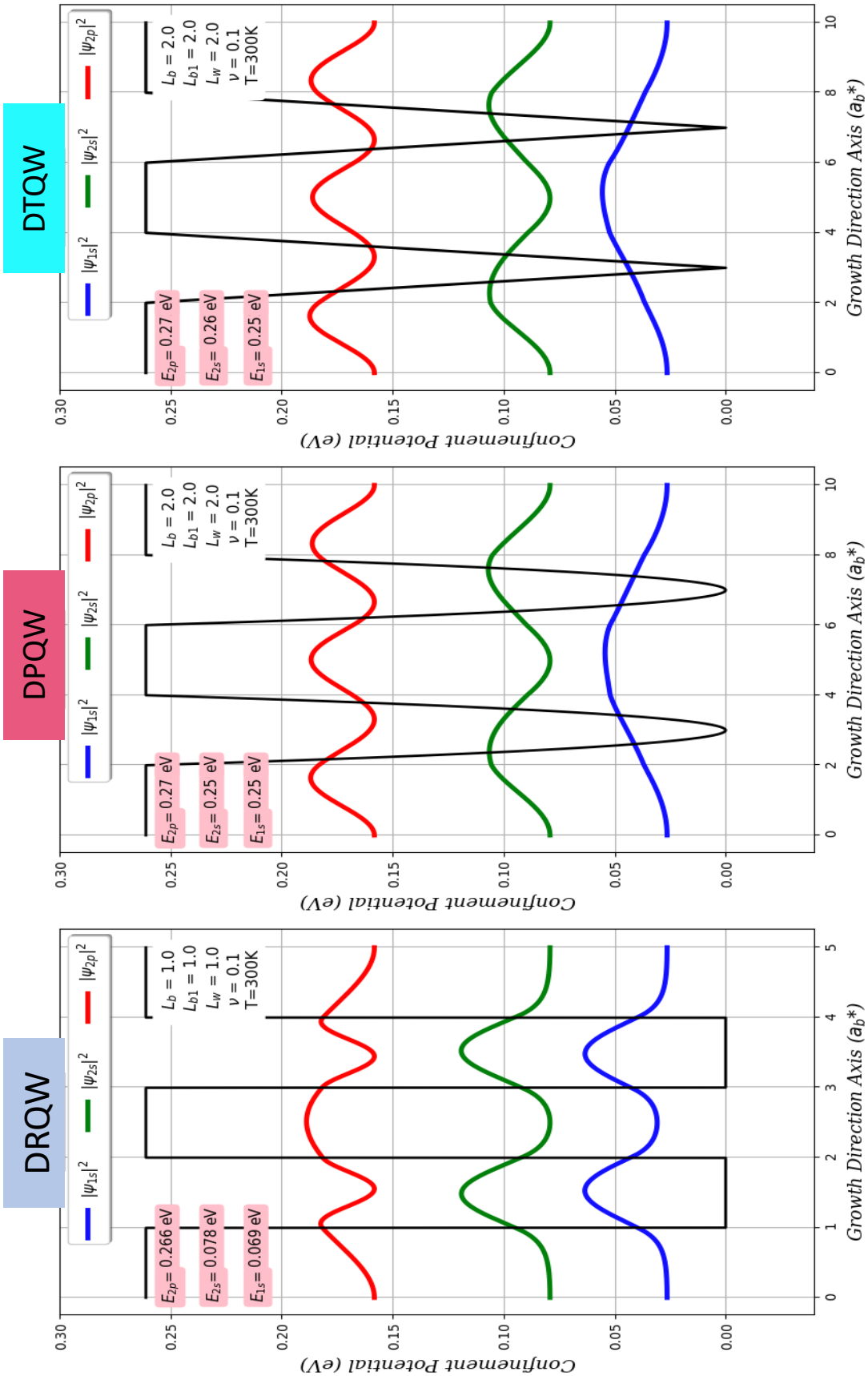


Figure. 4.1. Probability density of 1s, 2s, and 2p states in finite InGaN/GaN on-center donor impurity DRQW, DPQW and DTQW as a function of the growth direction. Potential profiles are included.

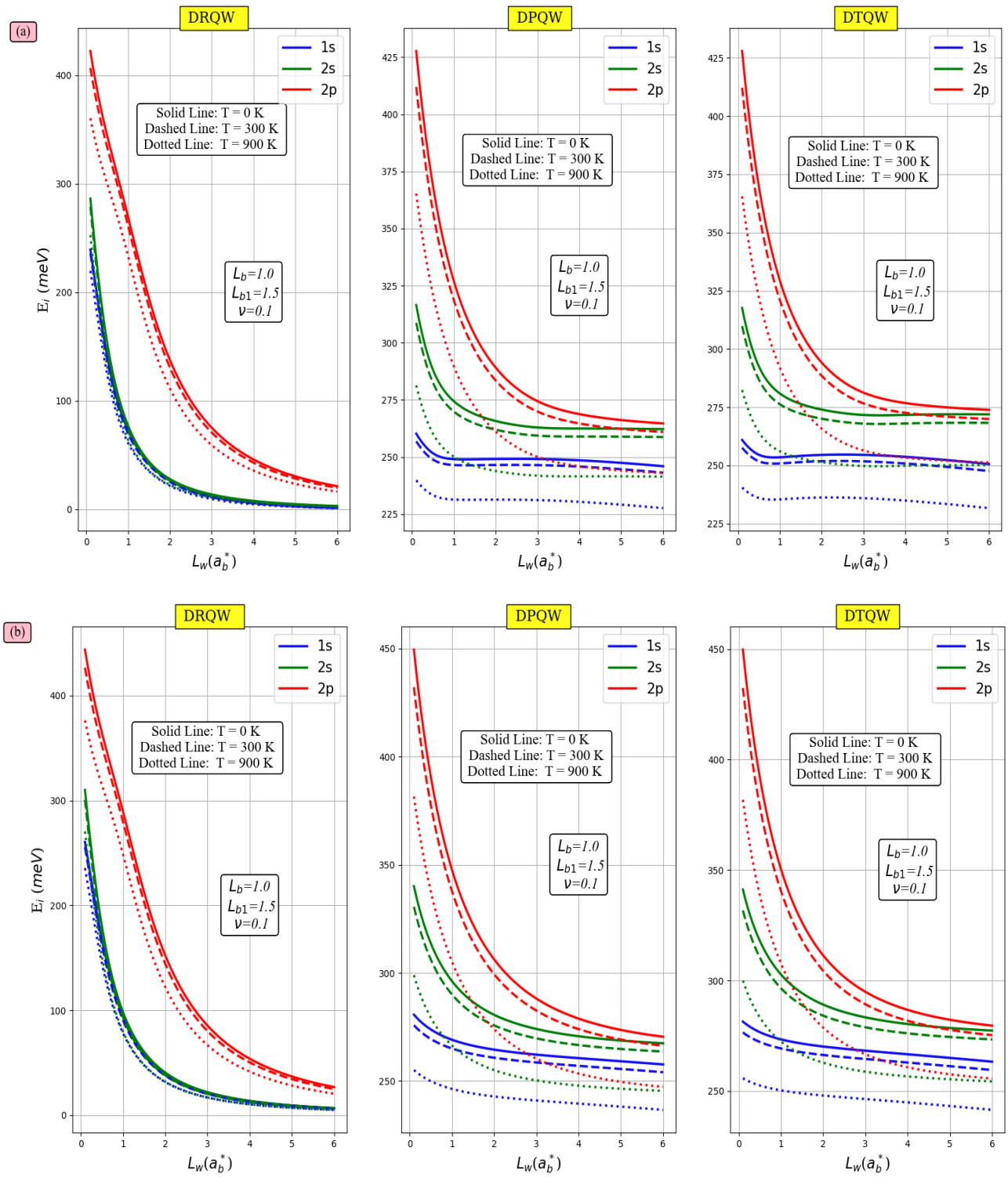


Figure. 4.2. Variation of the donor 1s, 2s and 2p states energies versus well width in a $GaN/In_{0.25}Ga_{0.75}N$ rectangular, parabolic and triangular DQWs for fixed parameters L_b = 1 and L_{b1}= 1.5, in the presence (a) absence (b) of impurity, at T=0K (solid curve), T=300K (dashed curve) and T=900K (dotted curve).

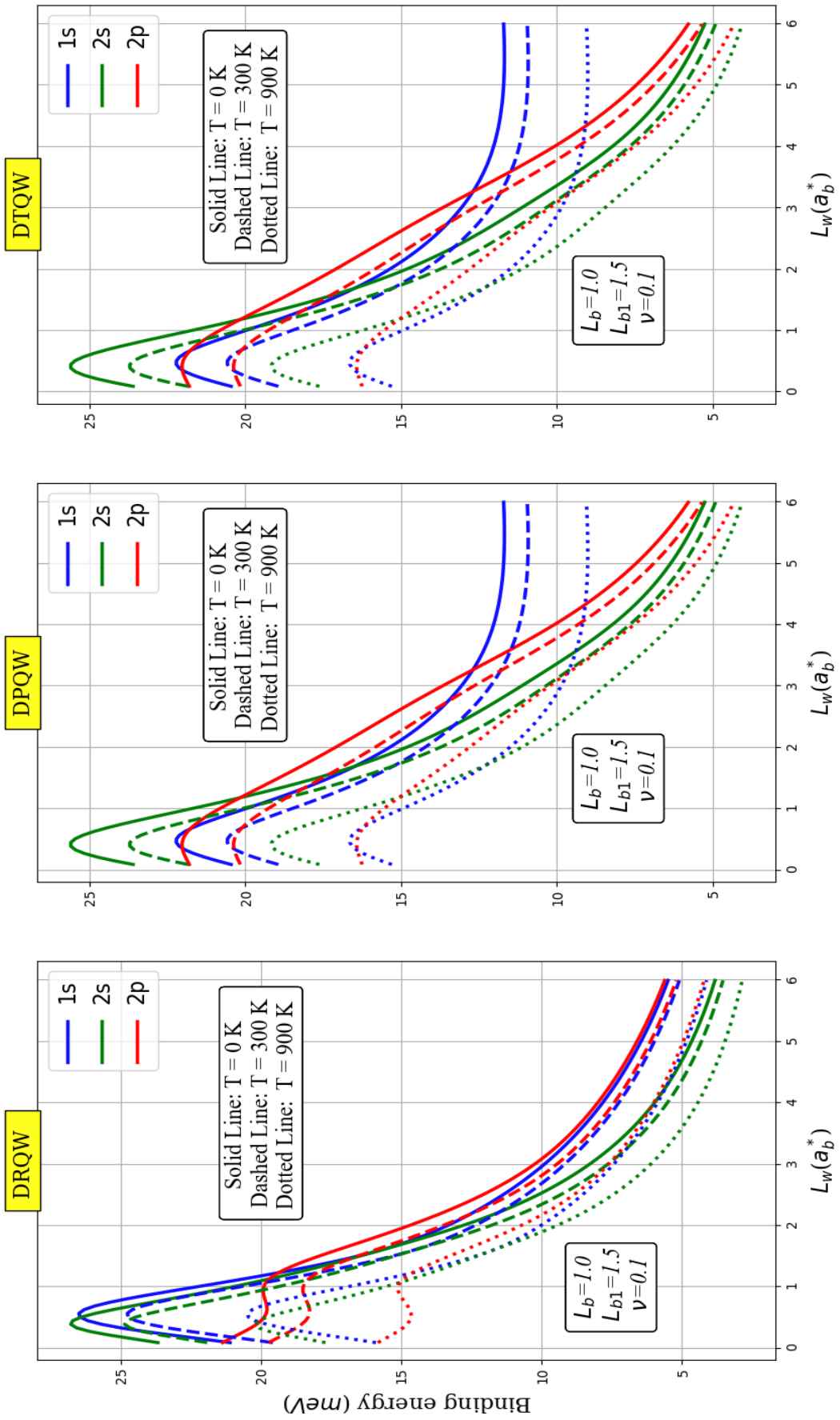


Figure 4.3. The 1s, 2s and 2p states binding energy E_b as a function of the well width in a $GaN/In_\nu Ga_{1-\nu}N$ DRQW, DPQW and DTQW for fixed parameters $\nu = 0.1, L_b = 1,\ L_{b1} = 1.5$, for different temperature values T=0K (solid curve), T=300K (dashed curve) and T=900K (dotted curve).

decreases according to the well width as expected. The curves show similar behavior for all structures for both cases with and without impurity. It is clearly seen that the presence of the impurity leads to the drop of the electron energy which can be due to the Coulomb interaction. It is obviously shown that the electron energy decreases when the temperature increases for all the well widths. This can be assigned to the effective-mass, dielectric constant and potential barrier height dependence according to the temperature as reported in Table 4.2. It is important to mention that this behavior is quite significant in parabolic and triangular DQWs compared to rectangular one.

Table 4.2. The variation of the barrier height, the effective mass and dielectric constant for both well and barrier regions with temperature T for $\nu = 0.1$.

T (K)	Effective mass (m_0)		Dielectric constant (ε_0)		Barrier height (meV)
	In well	In barrier	In barrier	In well	
0	0.182	0.199	10.15	9.51	286.57
300	0.179	0.196	10.43	9.80	284.09
900	0.168	0.184	11.04	10.40	273.27

Figure 4.3 exhibits the variation of 1s-state, 2s and 2p states binding energy associated with an on-center hydrogenic donor impurity in DRQW, DPQW and DTQW as a function of the well width with similar parameters as those fixed in Figure 4.2, for different temperature values T=0 K, 300 K and 900 K. This figure indicates that, as the well width decreases, the binding energy increases reaching a maximum value near the effective Bohr radius, then decreases. The physical reason can be given as follows. A decrement of the well width leads to an increment of the quantum localization effect of the electron wave function and therefore much stronger quantum confinement effect. Thus, the mean relative electron–impurity distance is reduced and the donor binding energy is increased. Additionally, the behavior of the 2p-state is quite different from 1s and 2s states. This difference behavior is in good agreement with those reported in Refs. [170–172] . Moreover, it can be seen from this figure that, the increasing temperature E_b drops for all well widths. Table 4.2 shows that, as the temperature increases dielectric constant increases whilst effective mass and the potential barrier height decrease, leading to an increase in the kinetic energy of donor electrons.

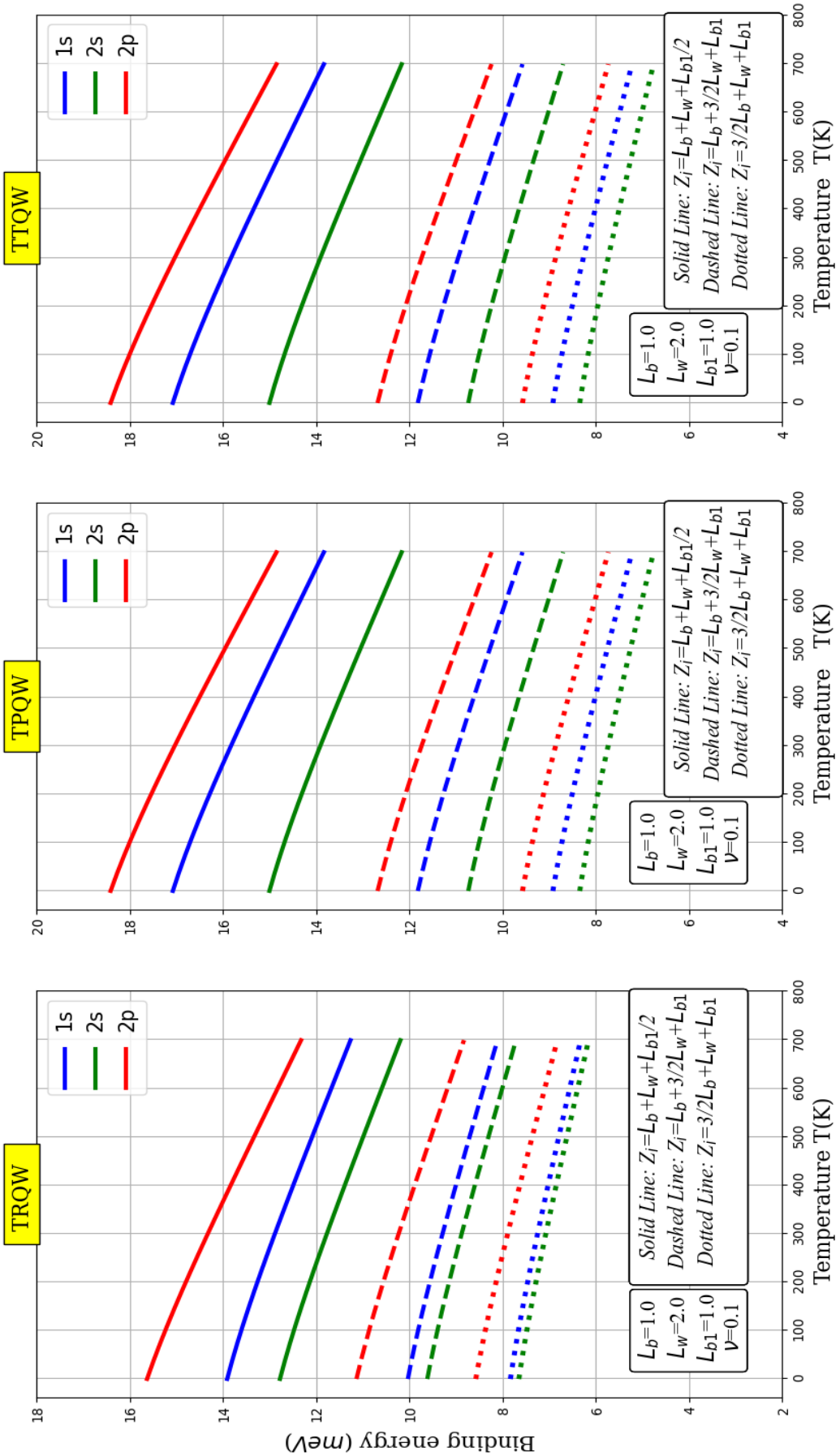


Figure 4.4. Variation of 1s, 2s and 2p states binding energy E_b with temperature T in DRQW, DPQW and DTQW for fixed parameters $\nu = 0.1, L_b = L_{b1} = 1$ and $L_w = 2$ with donor impurities located in the structure center (solid curve), in the right well center (dashed curve) and in the right barrier center (dotted curve).

Furthermore, an increase in the temperature weakens the Coulomb interaction between the electron and the impurity. As a result, the binding energy drops as the temperature increases. Our findings are in good agreement with those reported in Ref. [173] .

The dependencies of the donor ground state (blue curve), first (green curve) and second (red curve) excited states binding energy upon the temperature T in a $GaN/In_{0.1}Ga_{0.9}N$ rectangular, parabolic and triangular DQWs are shown in Figure 4.4, with donor impurities located in the structure center (solid curve), the right well center (dashed curve), and the right barrier center (dotted curve). As demonstrated in Figure 4.3, the donor binding energy decreases as temperature increases for a constant impurity position. For instance, the on-center impurity binding energy difference $E_b^{1s}(0\text{ K}) - E_b^{1s}(900\text{ K})$ is equal to 3.48 meV for DRQW, and 4.26 meV for both DPQW and DTQW. Additionally, we can see that the donor binding energy E_b is largest when the impurity is located at the center of each structure, as expected. This may be due to, as A. M. Elabsy and P. Nithiananthi [157,158] suggests; the temperature-dependent wavefunction is more localized for on-center impurity. For instance, as the impurity moves from the right barrier center to the structure center, for a fixed value of temperature $E_b^{1s}(\text{T} = 0\text{K})$ improvement is about 77.6% in DRQW, whereas it exceeds 91.4% in DPQW and DTQW.

In Figure 4.5, we simulate the ground state, first and second excited states binding energy E_b of an on-center shallow donor impurity as a function of the side barrier width L_b for diverse values of L_{b1} and fixed parameters $\nu = 0.1$, T=300 K. The behavior of the ground state binding energy as a function of L_b is similar to that found in our previous work [22] in simple and double rectangular QWs. More precisely, BE augments (drops) with decreasing the barrier width for a low (strong) confinement regime. The physical reason is that for strong confinement, the entire wave function is in the barrier, the more the barrier width increases the more the wave function spreads in the barrier which reduces the binding energy. In parallel, for low confinement, with increasing the barrier width the wave-function spread in the barrier diminishes, which leads to enhance the binding energy. The same figure (inset) contains the variation of the 2s and 2p states binding energy versus the barrier width. the binding energy of those states increases, reaching a maximum, then decreases as the barrier width is increased. this behavior is different from that of the ground state, E_b is more significant for barrier width near the effective Bohr radius. Moreover, the binding energy drops as the coupling barrier width increases. For instance, the ground state binding energy

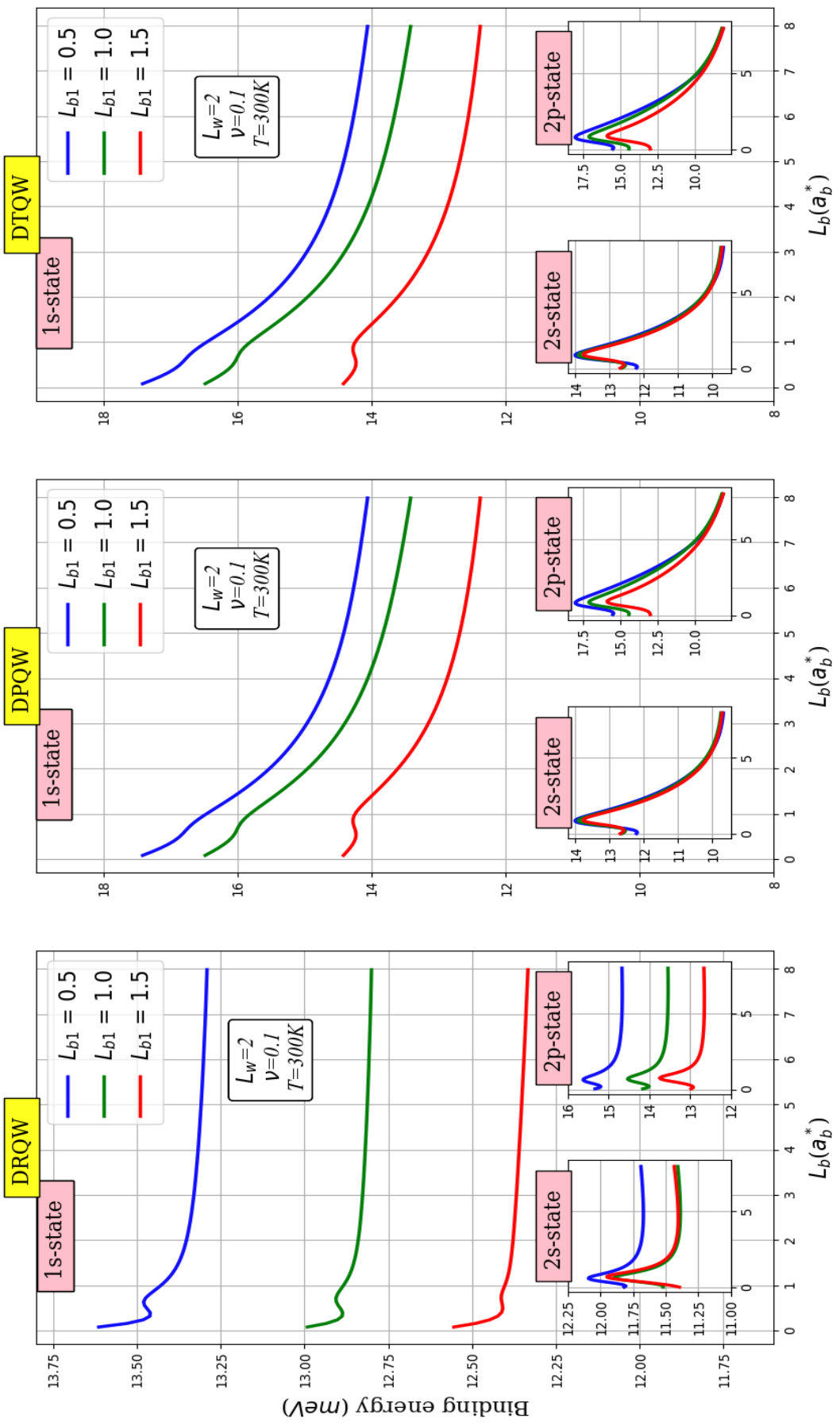


Figure 4.5. The ground state, 2s, and 2p states binding energy E_b of an on-center hydrogenic donor impurity as a function of the side barrier's width of DRQW, DPQW and DTQW for different coupling barrier widths L_{b1} = 0.5, 1.0 and 1.5 with an indium content ν = 0.1, L_w = 2 and T=300K.

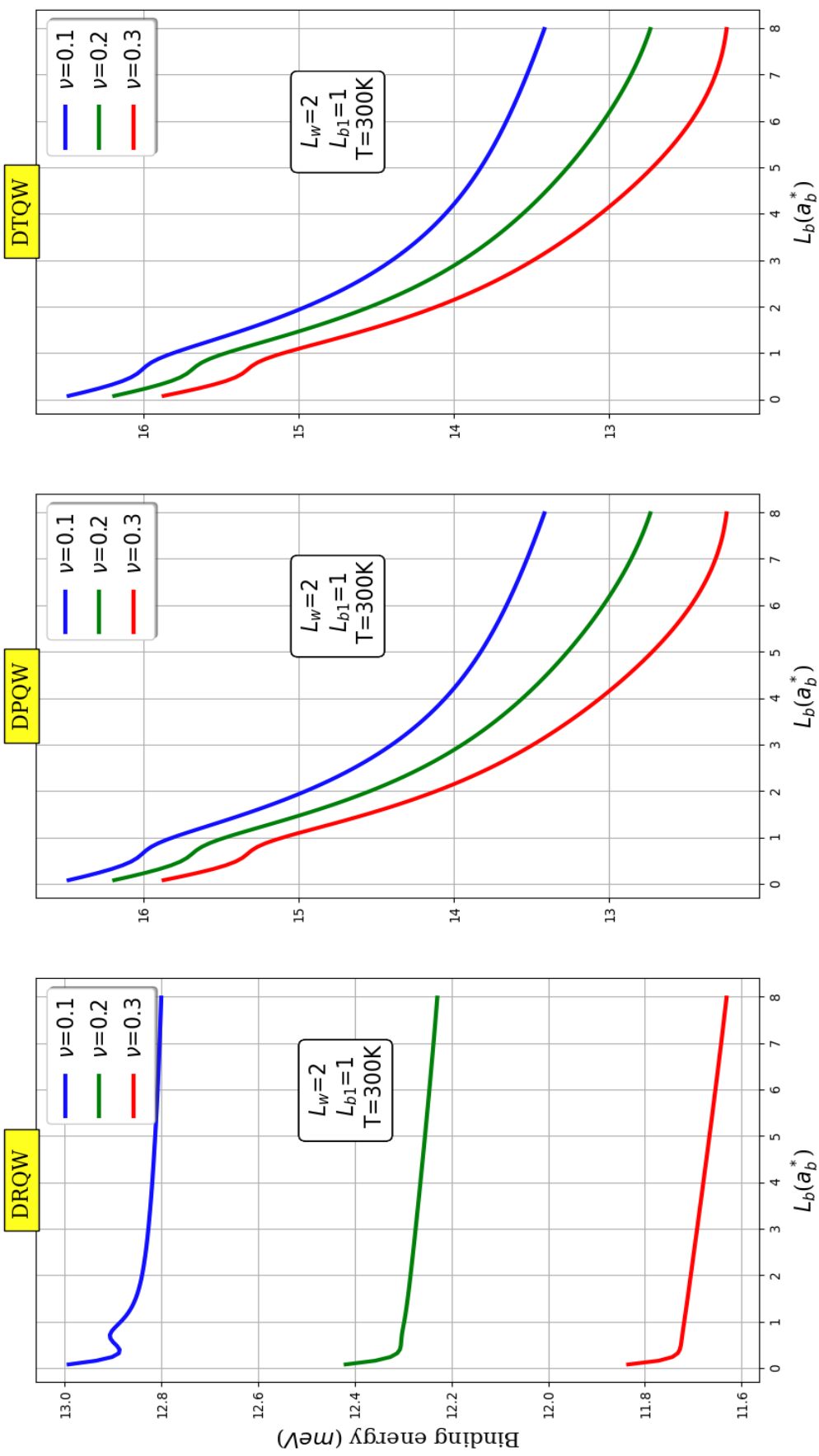


Figure 4.6. Ground state binding energy E_b of an on-center hydrogenic donor impurity as a function of the side barrier's width of DRQW, DPQW and DTQW for fixed parameters T = 300 K, $L_{b1} = 1, L_w = 2$ for different indium content $\nu =$ 0.1, 0.2 and 0.3.

drop rate is about 8.5% in DRQW and 20.8% in both DPQW and DTQW. This result can be attributed to the lowering of the wave-functions overlapping in both wells.

In Figure 4.6, we study the E_b as a function of the side barrier width L by varying the amount of indium in the $In_vGa_{1-v}N$ alloy with similar parameters as those fixed in Figure 4.5. As the indium fraction increases, the electron effective mass decreases while the band discontinuity increases, thus the geometric confinement of the electron wavefunction increases. Subsequently, as the electron gets more energy, its barrier penetration enhances, approaching the bulk behavior. This penetration weakens the Coulomb interaction between the electron and the impurity; thus, the overlap function gets smaller and the binding energy begins to decrease. Our findings are in good agreement with Ref. [174].

4.4. CONCLUSION

Using the effective-mass approximation within the finite element method, the wave functions, binding energy, energies with and without impurity of the 1s, 2s, and 2p states of a shallow donor impurity in InGaN/GaN DQWs have been investigated. This chapter has been devoted to investigate temperature, system dimensions, impurity position and indium mole fraction effects under finite rectangular, parabolic and triangular confinement potentials shapes. The effective-mass, dielectric constant, band-gap energy, and potential barrier temperature dependencies have been taken into consideration. Based on numerical results our conclusions are summed up in the following points: (1) The binding energy is enhanced versus the coupling effect. (2) It is reduced as a function of displacement of the impurity away from the structure center. (3) It is reduced as the In-concentration increases. (4) The binding energy is a decreasing function of temperature. (5) The binding energy is enhanced in DPQW and DTQW more than in DRQW; thus, the changes in the BE dependent on the confinement potential shape.

Chapter 5

Combined effect of temperature and electric field on the binding energy in (Al,Ga)N/AlN DQW for different shapes

5.1. INTRODUCTION

Understanding the impurity states in semiconductors is critical, as the incorporation of impurities can drastically alter the performance of optoelectronic devices. The application of an external electric field along the crystal growth direction enables the carrier distribution to polarize and the quantum energy state to shift, Dalgic and co-workers [175] have investigated the electric field effect on the non-hydrogenic binding energy of shallow donor impurity in a square and cylindrical GaAs/(Ga, Al)As QWW. In a similar context, Aktas and co-workers [176,177] have investigated the shallow donor impurity binding energy (E_b) under applied electric and magnetic fields in a coaxial GaAs/(Ga,Al)As QWW. Authors have calculated the E_b versus the impurity position and barrier width for several values of magnetic and electric fields. Such effects can induce significantly alters in the energy spectrum of carriers, which can be a useful tool to modulate the output of optoelectronic devices. The temperature effect is to modify the dielectric constant, the masses of carriers, the stability of exciton the energy levels, and the potential barrier [156] . The temperature effect has been investigated by Elabsy [157] and Nithiananthi and Jayakumar [158] in a $GaAs/Ga_{1-x}Al_xAs$ quantum well, and R. Khordad [159] in a V-groove $GaAs/Ga_{1-x}Al_xAs$ quantum wire, and M. Hu [25] in a cylindrical GaInAs/GaAs quantum dot.

This chapter is dedicated to investigate the shallow-donor-related binding energy of the ground and two low-lying excited states of on-centre hydrogenic impurity in (Al,Ga)N/AlN double quantum wells for rectangular (DRQW), parabolic (DPQW), and triangular (DTQW) potential profiles, under the combined effects of temperature and electric field, taking into account the difference in the effective mass and the dielectric constant between the well material (Al,Ga)N and the barrier material, AlN. The effects of the well width and the gallium concentration have also been taken into account in the calculations. The Schrodinger equation is treated based on the FDM considering the realistic finite potential barrier height and adequate boundary conditions at the interfaces.

5.2. THEORETICAL APPROACH

The Hamiltonian of the studied system in the presence of a shallow donor impurity located along the z-axis of the DTQW in using the effective mass approximation is expressed:

$$\mathrm{H} = -\frac{\hbar^2}{2}\vec{\nabla}\left(\frac{1}{\mathrm{m}^*}\vec{\nabla}\right) - \frac{e^2}{\varepsilon^*|\vec{\mathrm{r}}_e - \vec{\mathrm{r}}_\mathrm{i}|} + \mathrm{V}\,(z, \upsilon, \mathrm{T}) + |\mathrm{e}|Fz \tag{5.1}$$

F is the external applied electric field along the z-axis, $\vec{\mathrm{r}}_e$ is the position of the electron, $\vec{\mathrm{r}}_i$ is the position of the impurity, z_e is the position of the electron along the z-axis, and V $(z, \upsilon, \mathrm{T})$ is the finite confinement potential for the electron, which has the form:

- rectangular double quantum wells

$$V(z, \upsilon, \mathrm{T}) = \begin{cases} 0, & L_b < z < L_b + L_w \\ 0, & L_b + L_w + L_{b1} < z < L_b + 2L_w + L_{b1} \\ V_0(\upsilon, \mathrm{T}), & Elswhere \end{cases} \tag{5.2}$$

- parabolic double quantum wells

$$\mathrm{V}(z, \upsilon, \mathrm{T}) = \begin{cases} \left(\frac{4}{L_w^2}\right)\left(z - L_b - \frac{1}{2}L_w\right)^2 V_0(\upsilon, T), & L_b < z < L_b + L_w \\ \left(\frac{4}{L_w^2}\right)\left(z - L_b - L_{b1} - \frac{3}{2}L_w\right)^2 V_0(\upsilon, T), & L_b + L_{b1} + L_w < z < L_b + L_{b1} + L_w \\ V_0(\upsilon, T), & Elsewhere \end{cases} \tag{5.3}$$

- triangular double quantum wells

$$\mathrm{V}(z, \upsilon, \mathrm{T}) = \begin{cases} \left(-\frac{2}{L_w}\right)\left(z - L_b - \frac{1}{2}L_w\right) V_0(\upsilon, \mathrm{T}), & L_b < z < L_b + \frac{1}{2}L_w \\ \left(\frac{2}{L_w}\right)\left(z - L_b - \frac{1}{2}L_w\right) V_0(\upsilon, \mathrm{T}), & L_b + \frac{1}{2}L_w < z < L_b + L_w \\ \left(-\frac{2}{L_w}\right)\left(z - L_b - L_{b1} - \frac{3}{2}L_w\right) V_0(\upsilon, \mathrm{T}), & L_b + L_w + L_{b1} < z < L_b + \frac{3}{2}L_w + L_{b1} \\ \left(\frac{2}{L_w}\right)\left(z - L_b - L_{b1} - \frac{3}{2}L_w\right) V_0(\upsilon, \mathrm{T}), & L_b + \frac{3}{2}L_w + L_{b1} < z < L_b + 2L_w + L_{b1} \\ V_0(\upsilon, \mathrm{T}), & Elswhere \end{cases} \tag{5.4}$$

L_b, L_{b1}, and L_w present respectively the width of the edge barriers material (AlN), the width of mid barrier material (AlN), and the width of the well ($Ga_\upsilon Al_{1-\upsilon}N$).

$V_0(\upsilon, \mathrm{T})$ is the barrier height expressed as a function of the Gallium concentration υ and temperature is given by:

$$V_0(\upsilon, \mathrm{T}) = 1.5 * \left(E_g^{AlN}(T) - E_g^{Ga_\upsilon Al_{1-\upsilon}N}(\upsilon, T)\right) \tag{5.5}$$

Using Vegard law, and based on the energy gaps of AlN and GaN, the gap energy of $Ga_{\upsilon}Al_{1-\upsilon}N$ alloy can be calculated as follows:

$$E_g^{Ga_{\upsilon}Al_{1-\upsilon}N}(\upsilon,T) = \upsilon E_g^{GaN}(T) + (1-\upsilon)E_g^{AlN}(T) - b(1-\upsilon)\upsilon \tag{5.6}$$

with b=0.7 [166] is the bowing parameter.

According to Ref. [165] , the Temperature-dependent band-gap energy is given as:

$$E_g(T) = E_g(0) - \frac{\alpha * T^2}{T+\beta} \tag{5.7}$$

where $E_g(0)$ is the band-gap energy at $T = 0$K, and α and β are constants. The suggested parameters used in Eq. (5.7) in our calculations are summarized in Table 5.1 for wurtzite AlN and GaN.

The electron effective mass is affected by temperature, it is given as [167] :

$$\frac{m_0}{m^*(T)} = 1 + \frac{C}{E_g(T)} \tag{5.8}$$

where m_0 is the mass of the free electron, $E_g(T)$ temperature-dependent band-gap energy and C is the energy related to the momentum matrix element obtained from Eq. (5.8) at $T = 300$K which gives $C(AlN) = 17.91$ eV and $C(GaN) = 14.67$ eV.

Using a linear interpolation of the AlN and GaN binaries, the effective mass of the electron and dielectric constant of GaAlN alloy can be formulated as:

$$m^*_{Ga_{\upsilon}Al_{1-\upsilon}N}(\upsilon,T) = \upsilon m^*_{GaN}(T) + (1-\upsilon)m^*_{AlN}(T) \tag{5.9}$$

$$\varepsilon^*_{Ga_{\upsilon}Al_{1-\upsilon}N}(\upsilon,T) = \upsilon \varepsilon^*_{GaN}(T) + (1-\upsilon)\varepsilon^*_{AlN}(T) \tag{5.10}$$

The dielectric constant ε^* is related to the temperature, which is approximated by the linear interpolation [168] :

$$\varepsilon^*(T) = \varepsilon^*_i(0) * exp\big((T-300) * 10^{-4}\big) \qquad i \equiv (Well, Barrier) \tag{5.11}$$

At the interface between the well and the barrier, there is an overlap between AlN and (Al,Ga)N materials. Thus, as adopted in recent work [169] the dielectric constant at the interfaces is expressed as follows:

$$\varepsilon^*_{Interfaces} = \sqrt{\varepsilon^*_{AlN} \times \varepsilon^*_{Ga_\upsilon Al_{1-\upsilon} N}} \tag{5.12}$$

By adopting the effective Bohr radius (EBR) $a^*_b = \varepsilon^*_b \hbar^2 / m^*_b e^2 (= 1.19\ \text{nm})$ for the length unit, the effective electron Rydberg $R^*_b = e^2/2\varepsilon^*_b a^*_b (= 71\ \text{meV})$ as the unit of the energy and the effective electric field $\eta = e a^*_b F / R^*_b$ as the unit of the electric field , the effective Hamiltonian can be expressed as:

$$\widehat{H} = -\nabla^2 - \frac{2}{r} + V(z_e, \upsilon, T) + \eta z \tag{5.13}$$

Using the finite difference method, the eigenvalues of the Hamiltonian given in Eq. (5.13) can be calculated. Then, the ground state and two low lying-excited states shallow-donor binding energy are obtained as follows:

$$E^j_b = E^j_0 - E^j_{\text{Imp}} \qquad j \equiv 1s, 2s \text{ and } 2p \text{ states} \tag{5.14}$$

5.3. Numerical Results and Discussion

Here, we present our numerical results for the temperature, electric field, impurity position, size, and coupling effects on the ground state, first and second excited states in a finite (Al,Ga)N/AlN double rectangular (DRQW), parabolic (DPQW) and triangular (DTQW) quantum wells. The solution of the Schrödinger equation for the ground and excited states are obtained numerically by using the FEM. The parameters used in our calculations are those reported by Vurgaftman et al. [141] which are listed in Table 5.1.

Table 5.1. Physical parameters of wurtzite AlN and GaN used in our computations.

	$E_g(0K)(eV)$	$\alpha\ (meV.K^{-1})$	$\beta\ (K)$	$\varepsilon^*(300K)(\varepsilon_0)$
AlN	6.23	1.799	1462	8.5
GaN	3.299	0.909	830	9.5

First of all, for a proper understanding of the results that shall be presented below, it is necessary to recall the main features of the application of static electric field on finite (Al,Ga)N/AlN double quantum wells. Thus, we present the variations of the potential energy profile with the three lowest energy states and their corresponding probability densities for the DRQW, DPQW, and DTQW in Figure 5.1.

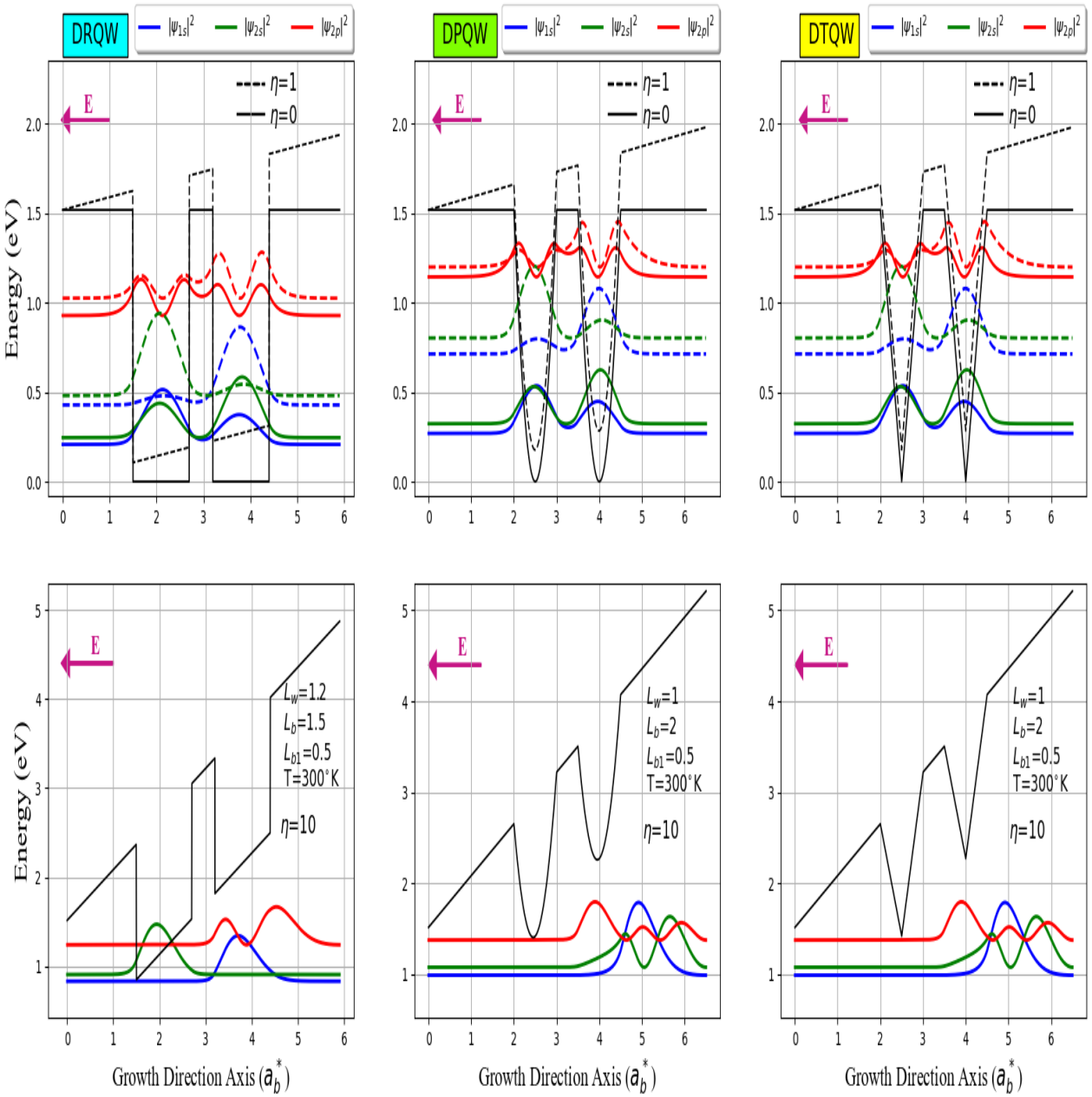


Figure 5.1. The variations of the confinement potential profile, ground, first and second excited state energies and the squared wave functions for related energy levels for different values of the electric field.

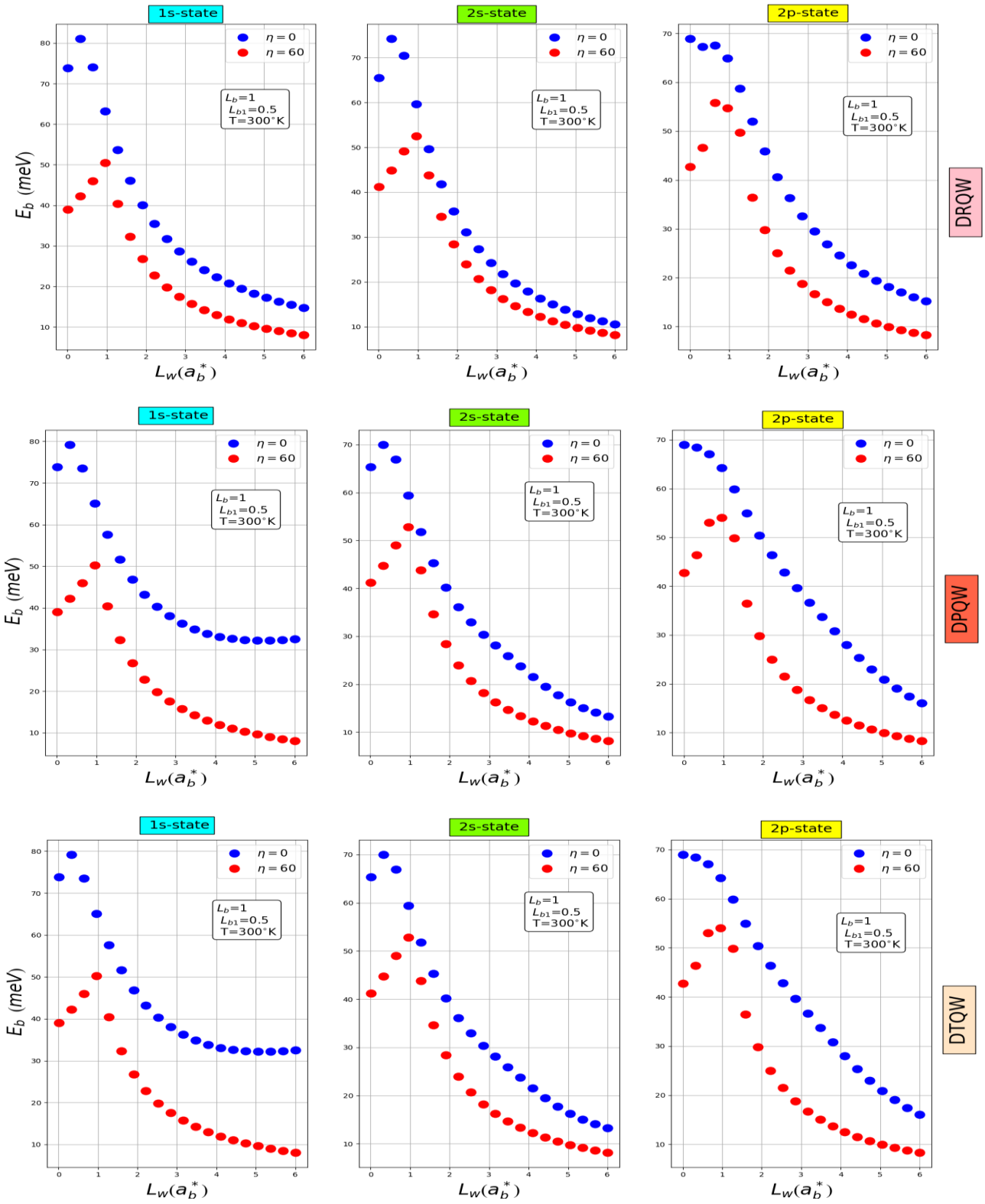


Figure 5.2. The 1s, 2s, and 2p states binding energy $E_b(meV)$ as a function of the well width $L_w(a_b^*)$ in $AlN/Al_{1-\upsilon}Ga_\upsilon N$ DRQW, DPQW, and DTQW for fixed parameters υ=0.1, L_b= 1, L_{b1} =0.5 at $T = 300°K$, for two values of electric field $\eta = 0$ (blue curve) and $\eta = 60$ (red curve).

When an electric field is applied to the growth direction, the shape of the quantum wells is deformed. Thus, the conduction band edge is not flat anymore. It is tilted because of the electric field. With the impact of the electric field, the electrons are transferred partially to the right side of the QWs. Consequently, the energy position of the QWs bottom shifts upwards and therefore the energy of 1s and 2s states increases as well. Such an increase becomes more notorious for higher electric field intensities [178]. 2p state is less affected and shifts upwards slightly. With the increase of *F*, the overall tendency is that the energy differences between the ground state and the first (second) excited states increase (decrease), which results in blue-shifts (red-shifts) (see Table 5.2). With regard to the polarization of the system, the presence of an electric field causes the spatial displacement of the electron probability density. As in the case of the energy values, this effect is more pronounced for the 1s and 2s states, in which $|\psi_{1s}|^2$ confines in the right well and $|\psi_{2s}|^2$ confines in the left well. The wave functions of the 2p state become also deformed by the electric field effect and, more importantly, pushed in the opposite direction of the electric field. When the electric field is about 10, almost the whole wave function is located in the barrier material, so the binding energy is close to the binding energy of bulk material. The same behavior is reported for a rectangular parallelepiped-shaped QD by Shu and Jian [179] by means of a traditional Ritz variational method. This effect is more pronounced in triangular and parabolic profiles than in the rectangular profile. The physical reason behind such behavior is the geometric confinement which is stronger in parabolic and triangular profiles compared to rectangular profile.

Table 5.2. The variation of the energy difference ΔE (meV) between the two lowest excited states and the ground state with the electric field.

	η	ΔE_{1s-2s}	ΔE_{1s-2p}
RDQW	0	58	876
	1	85	482
	10	90	361
PDQW and TDQW	0	44	730
	1	58	605
	10	90	440

The results regarding the effects of the electric field and the well width on the binding energy are shown in Figure 5.2 at T=300°K. This figure indicates that, as the well width decreases, the

binding energy increases reaching a maximum value at half of the effective Bohr radius, then decreases. The physical reason can be given as follows. The quantum localization impact of the electron wave function increases as the well width decreases, resulting in a considerably stronger quantum confinement effect. Thus, the mean relative electron–impurity distance decreases. and the donor binding energy is increased. However, the behavior of the 2p-state is quite different from 1s and 2s states and it agrees with the findings stated in Refs. [170–172] . As the electric field is applied, the binding energies of the ground state and low-lying excited states decrease for all well width values and their maximum value is pushed in the opposite direction of the applied EF (near the effective Bohr radius). This can be explained by the fact that the application of an external electric field breaks the symmetrical distribution of the electron wave functions. As a result, the electron is pushed against the field direction and the charge distribution is concentrated near the right wells, which leads to a decrement of the electronic quantum confinement effect. The electric field effect dominates over the confinement effect and yields a decrease in the binding energy.

In Figure 5.3, the well width and the temperature dependence of the binding energy is depicted for L_b= 1, L_{b1} =0.5 and υ=0.1. It can be seen from this figure that the increasing temperature decreases the binding energy for all well widths. Table 5.3 shows that, as the temperature increases dielectric constant increases whilst effective mass and the potential barrier height decrease, leading to an increase in the kinetic energy of donor electrons. Furthermore, an increase in the temperature weakens the Coulomb interaction between the electron and the impurity. As a result, the binding energy drops as the temperature increases. Our findings are in good agreement with those reported in Refs. [173,178–181] .

Table 5.3. The variation of the barrier height, the effective mass, and dielectric constant for both well and barrier regions with temperature T for υ= 0.1 and η=0.

$T\ (°K)$	Effective mass (m_0)		Dielectric constant (ε_0)		Barrier height (meV)
	well	barrier	well	barrier	
300	0.330	0.378	8.77	8.5	1.278
500	0.324	0.372	8.94	8.67	1.262

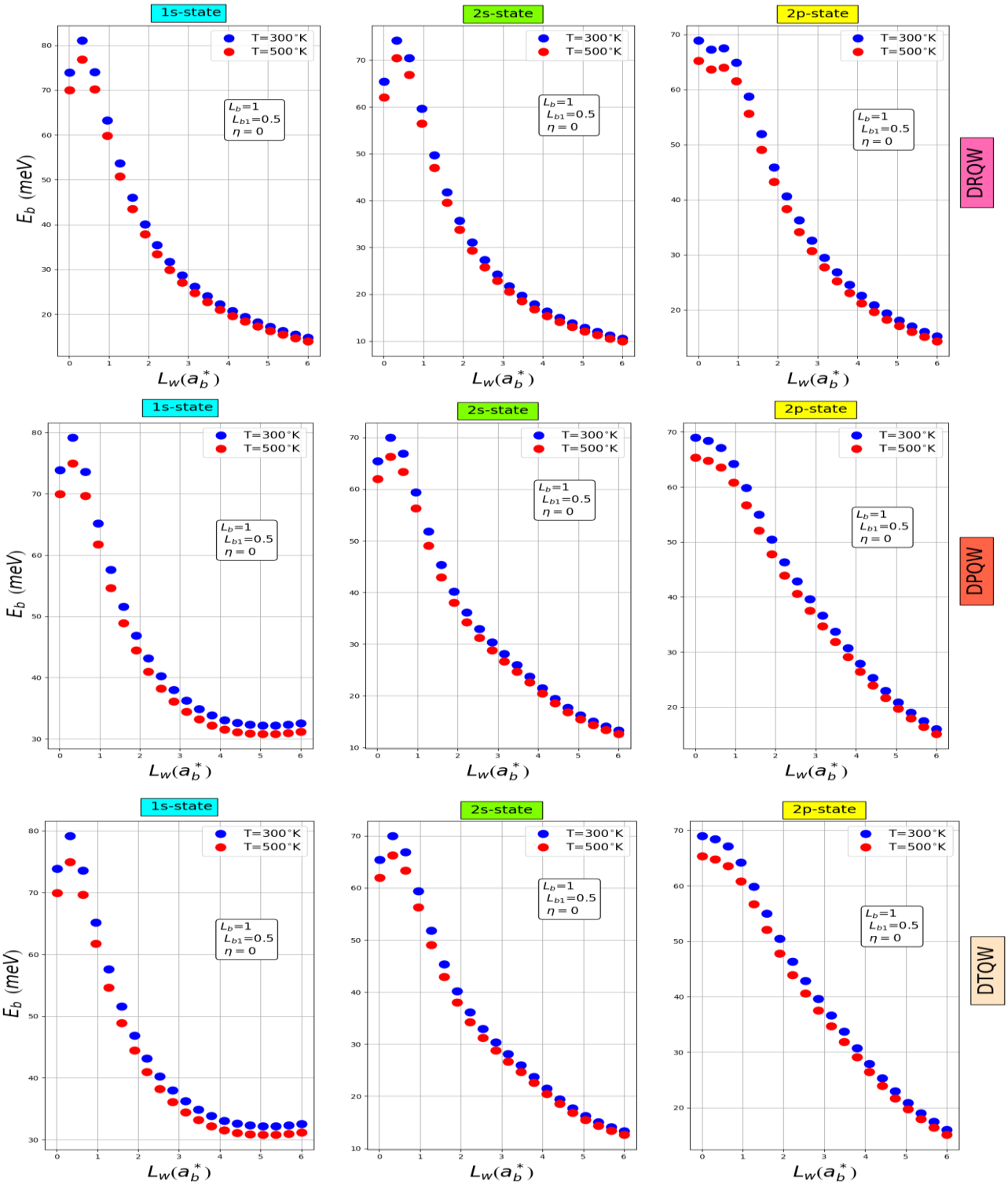


Figure 5.3. The 1s, 2s, and 2p states binding energy $E_b(meV)$ as a function of the well width $L_w(a_b^*)$ in $AlN/Al_{1-\upsilon}Ga_\upsilon N$ DRQW, DPQW, and DTQW for fixed parameters υ=0.1, L_b= 1, L_{b1} =0.5 with $\eta = 0$, for two values of temperature $T = 300°K$ (blue curve) and $T = 500°K$ (red curve).

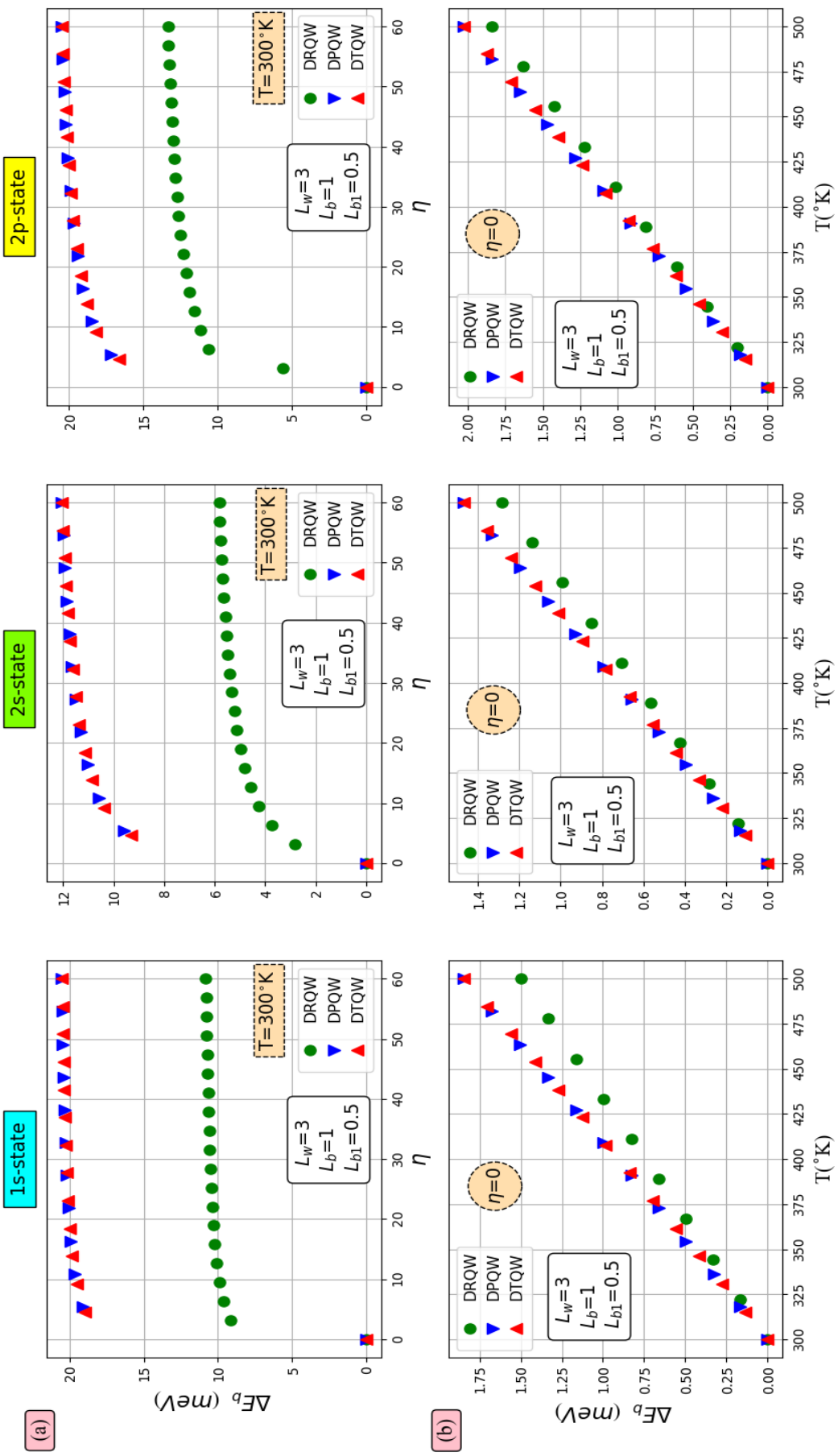


Figure 5.4. The difference of the 1s, 2s, and 2p-states shallow-donor binding energy ΔE_b (meV) of (Al,Ga)N/AlN DRQW, DPQW and DTQW as a function of the electric field η (a) and temperature T (b) for the fixed parameters L_w=3, L_b=1, L_{b1}=0.5 and υ= 0.1.

To clarify the binding energy behavior with studied geometrical shapes under the effects of temperature and electric field, the difference between the binding energies as a function of the electric field $\Delta E_b(\eta) = E_b(0) - E_b(\eta)$ and temperature $(\Delta E_b(T) = E_b(0) - E_b(T))$ is illustrated in Figure 5.4(a) and (b) respectively, for DRQW, DPQW, and DTQW.

Figure 5.4(a) depicts the results obtained for the difference binding energy as a function of the external electric field. It is shown that the $\Delta E_b(\eta)$ increases nonlinearly as a function of the external electric field; i.e, the binding energy decreases, while it tends to saturation regime for all confinement profiles. The results concerning the binding energy as a function of an external electric field effect are in good agreement with those reported in the literature. For (In,Ga)N–GaN parabolic QWW [182] and spherical QD [183] we have reported in our previous work that the main effect of the external electric field is to reduce the ground-state binding energy. When the electric field is greater than about 10 ($F = 6.10^8$ V/m), the binding energies quickly decrease to reach the saturation regime. This is because the electric field pushes the impurity wave function into the barrier material. When the electric field is greater than about 10, almost the whole wave function is located in the barrier material, so the binding energy is close to the binding energy of bulk material. The same behavior is reported for a rectangular parallelepiped-shaped QD by Shu and Jian [179] by means of a traditional Ritz variational method.

From Figure 5.4(b), we can observe that $\Delta E_b(T)$ is sensitive to the variation of the temperature. ΔE_b increases as T increases; i.e., one can see that the binding energy of a hydrogenic donor impurity in its ground state and two low lying excited states is decreased by increasing of temperature. For this behavior, we can mention an explanation with the help of the thermal energy concept. It may be due to the fact that with the application of thermal energy, the donor impurity gains more kinetic energy and the wavefunction is delocalized to a smaller extent and becomes less bound with the impurity atom. The same behavior is reported for $GaAs/Al_\upsilon Ga_{1-\upsilon}S$ for a rectangular quantum well by Nithiananthi and Jayakumar [184] and for a V-groove quantum wire by Khordad [159]. One can see that parabolic and triangular profiles are more sensitive to the external electric field and temperature than the rectangular form. With decreasing the length of the bottom of the wells, the Coulomb interaction between the electron and impurity decreases. As a result, the binding energy drops moving from the rectangular to the triangular profile. These results are in good agreement with those reported by Akankan et al. [185].

5.4. CONCLUSION

Using the effective-mass approximation within the finite element method, the density probabilities and the binding energies of the 1s, 2s, and 2p states of a shallow donor on-center impurity in (Al,Ga)N/AlN DQWs have been investigated. The temperature, electric field, system dimension, and geometrical shape effects are investigated. The effective mass, dielectric constant, band-gap energy, and potential barrier temperature dependencies have been taken into consideration. Based on our numerical results conclusions are summed up in the following points: (i) The system dimension and geometrical shape have a great influence on the binding energy. (ii) The binding energy drops versus both electric field and temperature. (iii) When the electric field is greater than about $6.10^8\ \mathrm{V/m}$, the binding energies quickly decrease to reach the saturation regime and the impurity wave function is pushed into the barrier material.

Chapter 6

Design optimization of multi-quantum well solar cells

6.1. INTRODUCTION

Multi quantum well (MQW) solar cell approach is based on the insertion of a MQW structure in the intrinsic region of p-i-n solar cells with a bunch of wider(barrier) and narrow (well) band gap semiconductor to improve the spectral response below the absorption edge of 'barrier' material. Absorbing layers in the form of a multiple quantum well (MQW) structure are often used to delay strain relaxation. This idea was pioneered by Barnham et al. in 1990 [186]. The MQW structure improves the p-i-n solar cell's efficiency and numerous researchers are working on this structure. This idea is developed by the Imperial College group [186–190]. The quantized energy levels in quantum structures become the driving force for more carrier generation [191]. Several theoretical models have been developed to explain the performance of the MQW solar cells [192–195].

An important difference between organic and conventional inorganic solar cells is in the minus binding energy. In both systems, excitons (induced states) occur upon photon absorption. In inorganic semiconductors, the energy required to decompose these excitons into charge carriers is relatively small (a few millielectric volts easily obtained at room temperature) [196].

Binding energy is another analysis that also elaborates the performance of a solar cell. The presence of small values of binding energy offers high power conversion efficiency and high charge transfers in an excited state. In addition, binding energy also provides strong information about Coulomb forces of attraction, the higher Coulomb forces always contain a small value of binding energies and vice versa [197].

In inorganic solar cells, regarding the design of the active region, many groups have focused on the optimization of the photovoltaic performance of the InGaN/GaN MQW solar cells by modulating the quantum well thickness [198], the barrier thickness [199–201], the In mole fraction of the wells [202], and the number of quantum wells[203–205].

6.2. INFLUENCE OF THE NUMBER OF QUANTUM WELLS ON PHOTOVOLTAIC CHARACTERISTICS

The number of QWs determines the total thickness of the active region in terms of absorption and carrier generation. Usually, in LED devices, the thickness of QWs is chosen to be relatively

small (less than 5 nm for In-content less than 30% to manage the strain balance). But in photovoltaic devices, it is necessary to stack as many wells as possible in the structure to get an effective absorption of incoming light. Although the presence of QWs helps to postpone the relaxation, anyway, it still appears when stacking too many periods leading to linear defects (for example threading dislocations and v-pits) [203].

There is also another problem showing up with an increase in the period number. The internal electric field created by the p-n junction decreases with the active region thickness. This hampers the separation of the electron and hole pairs and their drift to the n- and p- contacts. Therefore, the determination of the appropriate active region thickness is necessary for the development of an efficient device.

Table 6.1. Experimental values of the structural properties and photovoltaic performance of In0.1Ga0.9N/GaN multiple-quantum-well solar cells: number of quantum wells (N_w), external quantum efficiency (EQE), open-circuit voltage (V_{oc}), short-circuit current (J_{sc}), fill factor (FF), and overall conversion efficiency (η) under 1 sun AM1.5 G equivalent illumination [206].

QW number (N_w)	EQE at 380 nm (%)	V_{oc} (V)	J_{sc} (mA/cm^2)	FF (%)	η(%)
5	4	1.6	0.11	54	0.09
15	16	1.8	0.24	56	0.24
30	38	2.1	0.42	54	0.48
40	36	2.4	0.63	56	0.85
60	31	2.3	0.68	56	0.88
100	24	1.9	0.68	60	0.78

Therefore, Mukhtarova et al. [206] investigated $In_{0.11}Ga_{0.89}N(1.7nm)/GaN(8-9nm)$ solar cells with QW number from 5 to 100 (see Table 6.1). The conversion efficiency of 0.88% for the sample with 60 QWs under 1 Sun AM1.5G equivalent illumination was reached. This relatively low (compare to Si or GaAs) value shows that such kind of solar cells can not be used as an independent photovoltaic solution because it absorbs light only with a wavelength less than 415 nm, while the peak of the solar spectrum on the Earth is in 470-550 nm range. Therefore, it is necessary to increase the absorption wavelength of InGaN-based devices. This can be done by optimizing the QW design. Moreover, A low value of conversion efficiency under 1 Sun AM1.5G illumination is related to the lack of absorption at a wavelength higher than 415 nm. An enhancement of η by 1 order of magnitude is observed when increasing the number of QWs from

5 to 60. This increase is mainly associated with the variation of the short-circuit current density, which is enhanced by a factor of 6 with increasing the number of periods (See Table 6.1) [206].

Table 6.2. Theoretical values of the binding energy (meV) of $In_{0.1}Ga_{0.9}N(1nm)/GaN(1nm)$ multiple-quantum well with number of quantum wells (N_w).

QW number (N_w)	Binding energy (meV)
1	100
2	180
3	210

Similarly, we investigated the dependence of the binding energy of $In_{0.1}Ga_{0.9}N/GaN$ MQWs as a function of the number of quantum wells (N_w) (see Table II). BE increases with increasing N_w consequently decreasing the power conversion efficiency and low charge transfers in an excited state. However, besides the number of quantum wells, a MQW solar cell is optimized using the ideal MQW model by varying parameters such as Indium composition of the 'well' and 'barrier'; band gap difference of 'well' and 'barrier'; and the thickness of 'well' and 'barrier'.

6.3. INFLUENCE OF THE QUANTUM WELLS THICKNESS ON PHOTOVOLTAIC CHARACTERISTICS

Light absorption is one of the most critical points of the InGaN/GaN solar cells that determines the value of J_{sc}. One of the ways for light absorption enhancement is to increase the thickness of the absorbing InGaN layer. An increasing number of QWs leads to a thicker active region and decreases the internal electric field inside the structure damaging the collection efficiency. Another way to increase the thickness of the absorbing layer is to change the QW thickness.

Table 6.3. Electrical characteristics of samples with different QW thicknesses: short-circuit current J_{sc}, open-circuit voltage V_{oc}, fill factor FF and conversion efficiency η [207].

QW thickness (nm)	J_{sc} (mA/cm^2)	V_{oc} (V)	FF (%)	η (%)
1.3	0.42	2.2	54	0.49
3.1	0.46	1.3	42	0.25
5.4	0.14	1.1	47	0.07

The deepening of the energy levels with QW thickness increases the confinement of the carriers and prevents their escape from the well. Also, the enhancement of the strain inside the QW structure causes plastic relaxation and dislocation formation. Dislocations degrade the collection efficiency of the devices and induce a decrease of the EQE from 0.52 for the sample with 1.3 nm QW thickness to 0.13 for the sample with 5.4 nm QW thickness (See Table 6.3). Carriers are created inside the QWs, but they cannot be collected because of recombination with the defects. Therefore, the collection of the carriers is very poor. It induces a strong decrease in the values of open-circuit voltage and fill-factor leading to conversion efficiency degradation. Consequently, the best value of conversion efficiency of 0.49% is obtained for the sample with the thinnest QWs (1.3 nm).

Table 6.4. Theoretical values of the binding energy (meV) of $In_{0.1}Ga_{0.9}N(L_w)/GaN(1nm)$ multiple-quantum well with quantum wells thickness (L_w).

L_w (nm)	Binding energy (meV)
1	100
2	120
3	100

Similarly, we investigated the dependence of the binding energy of $In_{0.1}Ga_{0.9}N/GaN$ DQWs as a function of quantum wells thicknesses (L_w) (see Table 6.4). BE increases with increasing L_w until it reaches its maximum at $L_w = 2nm$ then decreases. The increase of QW thickness induces a lowering of the energy difference between hole and electron-states together with increased Quantum Confined Stark Effect, consequently decreasing the power conversion efficiency and low charge transfers in an excited state.

6.4. Influence of the barrier thickness on photovoltaic characteristics

The increase of In-content induces several problems that have to be overcome to avoid any damage to the device's electrical properties. One of them is the enhancement of the carrier confinement because of energy level deepening in the QWs. It becomes more difficult for carriers to escape and to be collected at the electrical contacts. Therefore, there are two main ways for

carriers to escape from the QWs: thermal emission and tunneling [203]. Thermal emission is efficient for low In-content devices because carriers can move easily out from the well at room temperature, but as the energy levels go deeper (as for thicker QWs) the thermal emission becomes insufficient. Normally, for GaN barrier thicknesses of 9 nm, the tunneling effect is negligible as it is shown in the literature [208,209]. Therefore, it is necessary to decrease the barrier thickness to enhance the tunneling probability of the carriers from the QWs. In this section, we will investigate the samples having a $15 \times \mathrm{In_{0.17}Ga_{0.83}N(2nm)/GaN}$ structure with 9 nm, 5.5 nm, and 3.7 nm GaN tuning barrier thickness.

Table 6.5. Summary of the electrical characteristics: external quantum efficiency EQE, open-circuit voltage V_{oc}, short-circuit current J_{sc}, fill factor FF, conversion efficiency η for $15 \times \mathrm{In_{0.17}Ga_{0.83}N(2nm)/GaN}$ −based devices with different barrier thicknesses under 1 Sun AM1.5G equivalent illumination [207].

QW thickness (nm)	EQE at 380 nm (%)	J_{sc} (mA/cm^2)	V_{oc} (V)	FF (%)	η (%)
3.7	27	0.60	2.2	57	0.78
5.5	30	0.61	1.9	63	0.73
9	35	0.69	1.9	70	0.92

From the device's point of view, the decrease of the barrier thickness enhances carrier tunneling. This creates an additional way for carriers to escape from QW improving the values of external quantum efficiency, short-circuit current and fill factor. However, a thinning of the barriers causes the appearance of strain relaxation accompanied by defect formation. This increases the leakage current through the active region of the device and reduces the value of open-circuit voltage (which falls from 2.2 V to 1.9 V) (See Table 6.5). Consequently, the best value of conversion efficiency of 0.92% is obtained for the sample with the thickest barrier (9 nm).

Table 6.6. Theoretical values of the binding energy (meV) of $\mathrm{In_{0.1}Ga_{0.9}N(1nm)/GaN(L_b)}$ simple-quantum well with the barrier thickness (L_b).

L_b (nm)	Binding energy (meV)
2.5	120
7.5	100
15	95

Similarly, we investigated the dependence of the binding energy of $In_{0.1}Ga_{0.9}N/GaN$ MQWs as a function of the barrier thickness (L_b) (see Table 6.6). BE decreases with increasing L_b. It is necessary to decrease the barrier thickness to enhance the tunneling probability of the carriers from the QWs.

6.5. CONCLUSION

The most important limitation for InGaN-based photovoltaics is a small value of short-circuit current. The J_{sc} strongly depends on the absorption of the light. One of the ways to increase absorption is to increase the thickness of QWs. losses in collection efficiency induced by the deepening of the electron and hole energy levels and defect formation due to strain relaxation enhancement with QW thickness.

The decrease of barrier thickness can also improve the collection efficiency and electrical performance of the InGaN QW-based solar cells by stimulating carrier tunneling. Despite of decreased absorption wavelength, the value of the short-circuit current was improved with barrier thickness decrease. This is related to enhanced carrier tunneling fraction in the total value of J_{sc} in addition to carriers that escaped QWs through thermionic emission. Thanks to carrier tunneling, the current under illumination becomes less sensitive to the change of the band diagram with applied bias and this improves the value of the fill factor as well.

Moreover, the conversion efficiency can be modulated by optimizing the number of quantum wells in solar cells' active layer.

Conclusions and perspectives

This work, separated into four parts, deals with the study of the binding energy in III-nitrides based simple and multiple quantum wells. Considering the effective-mass and dielectric mismatches between the well and its surrounding matrix, the numerical calculations are performed within the framework of the parabolic band and the single band effective-mass approximations under the finite potential barrier using finite element method (FEM). To be close to the reality, the diffusion effect at the interface between the well and the barrier is taken into account and an expression of the effective mass and dielectric constant is adopted. In addition, the pressure and temperature dependencies of the effective masse and dielectric constant were taken into account.

In the first part, we exploit the binding energy of hydrogenic shallow-donor impurity in simple and double coupled quantum wells based on unstrained wurtzite (In,Ga)N/GaN. The binding energy is enhanced versus the coupling effect, while it is reduced as a function of displacement of the impurity far away the structure center, a strong binding energy number of layer dependence is shown.

In the second part, we provide the calculation of the 1s-like binding energy of shallow-donor impurity in symmetric double coupled quantum wells based on wurtzite (In,Ga)N/GaN. The binding energy is enhanced (dropped) with increasing pressure for large (thin) well, declined with increasing wells coupling, and it is quite significant (insensitive) with increasing In-composition for thin (large) well.

In the third part, we investigate the shallow-donor-related binding energy of the ground and two low-lying excited states of on-centre hydrogenic impurity in (In,Ga)N/GaN double quantum wells for rectangular (DRQW), parabolic (DPQW), and triangular (DTQW) confinements, under the combined effects of temperature and electric field. The effects of the well width and the gallium

concentration have also been taken into account in the calculations. The binding energy is a decreasing function of temperature and the changes in the BE is dependent on the confinement potential shape. The binding energy is enhanced in DPQW and DTQW more than in DRQW. The confinement potential shape has a strong impact on the binding energy.

In the fourth part, we investigate the shallow-donor-related binding energy of the ground and two low-lying excited states of on-centre hydrogenic impurity in (Al,Ga)N/AlN double quantum wells for rectangular (DRQW), parabolic (DPQW), and triangular (DTQW) potential profiles, under the combined effects of temperature and electric field. The system dimension and geometrical shape have a great influence on the binding energy. The BE drops versus both electric field and temperature.

In the last chapter, we summarized the influence of the insertion of MQW structure in the intrinsic region of p-i-n solar cells, as well as the influence of well thickness, barrier thickness, and the number of quantum wells in a structure on the binding energy.

In addition, our results show that the binding energy is strongly modulated and conditioned by the position of the impurity, it is reduced as a function of displacement of the impurity away from the structure center. The indium (gallium) fractions have an impact on the binding energy and it is dependent on the confinement regime. Moreover, the conversion efficiency can be modulated by optimizing the number of quantum wells, the quantum well thickness, and barrier thickness in solar cells' active layer.

In This thesis, we focused on the study of the binding energy which besides the Bohr radius are the two most essential properties of an impurity in nanostructured semiconductor systems. Advanced properties can be further investigated in the future such as the photoionization cross section (PICS) which also plays a crucial role in the characterization of impurities in semiconductors.

100 .

References

[1] H.P. Maruska, J.J. Tietjen, The preparation and properties of vapor-deposited single-crystal-line GaN, Appl Phys Lett. 15 (1969) 327–329. https://doi.org/10.1063/1.1652845.

[2] H.M. Manasevit, F.M. Erdmann, W.I. Simpson, The Use of Metalorganics in the Preparation of Semiconductor Materials IV. The Nitrides of Aluminum and Gallium, J Electrochem Soc. 118 (1971) 1864. https://doi.org/https://doi.org/10.1149/1.2407853.

[3] S. Yoshida, S. Misawa, A. Itoh, Epitaxial growth of aluminum nitride films on sapphire by reactive evaporation, Appl Phys Lett. 26 (1975) 461–462. https://doi.org/10.1063/1.88210.

[4] J.I. Pankove, E.A. Miller, J.E. Berkeyheiser, GaN electroluminescent diodes, in: 1971 International Electron Devices Meeting, 1971. https://doi.org/https://doi.org/10.1109/IEDM.1971.188400.

[5] S. Yoshida, S. Misawa, S. Gonda, Improvements on the electrical and luminescent properties of reactive molecular beam epitaxially grown GaN films by using AlN-coated sapphire substrates, Appl Phys Lett. 42 (1983) 427–429. https://doi.org/10.1063/1.93952.

[6] H. Amano, M. Kito, K. Hiramatsu, I. Akasaki, P-type conduction in Mg-doped GaN treated with low-energy electron beam irradiation (LEEBI), Jpn J Appl Phys. 28 (1989) L2112–L2114. https://doi.org/10.1143/JJAP.28.L2112/XML.

[7] S. Nakamura, T. Mukai, M. Senoh, N. Iwasa, Thermal Annealing Effects on P-Type Mg-Doped GaN Films, Jpn J Appl Phys. 31 (1992) 139. https://doi.org/https://doi.org/10.1143/JJAP.31.L139.

[8] S. Nakamura, M. Senoh, T. Mukai, P-gan/n-ingan/n-gan double-heterostructure blue-light-emitting diodes, Jpn J Appl Phys. 32 (1993) L8–L11. https://doi.org/10.1143/JJAP.32.L8/XML.

[9] S. Nakamura, T. Mukai, M. Senoh, Candela-class high-brightness InGaN/AlGaN double-heterostructure blue-light-emitting diodes, Appl Phys Lett. 64 (1994) 1687–1689. https://doi.org/10.1063/1.111832.

[10] S. Nakamura, T. Mukai, M. Senoh, High-brightness InGaN/AlGaN double-heterostructure blue-green-light-emitting diodes, J Appl Phys. 76 (1994) 8189–8191. https://doi.org/10.1063/1.357872.

[11] S. Nakamura, M. Senoh, S.I. Nagahama, N. Iwasa, T. Yamada, T. Matsushita, Y. Sugimoto, H. Kiyoku, Room-temperature continuous-wave operation of InGaN multi-quantum-well structure laser diodes, Appl Phys Lett. 69 (1996) 4056–4058. https://doi.org/10.1063/1.117816.

[12] A. Sali, M. Fliyou, H. Satori, H. Loumrhari, E.N.S. de Âpartement De Physique, B.P. 5206, F. Ás, E.N.S. de Marrakech, B.P. 2400, The effect of a strong magnetic field on the binding energy and the photoionization process in quantum-well wires, Journal of Physics and Chemistry of Solids. 64 (2003). https://doi.org/10.1016/S0022-3697(02)00205-6.

[13] G. Bastard, Hydrogenic impurity states in a quantum well: A simple model, Phys Rev B. 24 (1980) 4714. https://doi.org/https://doi.org/10.1103/PhysRevB.24.4714.

[14] E. Iqraoun, A. Sali, A. Rezzouk, E. Feddi, F. Dujardin, M.E. Mora-Ramos, C.A. Duque, Donor impurity-related photoionization cross section in GaAs cone-like quantum dots under applied electric field, Philosophical Magazine. 97 (2017) 1445–1463. https://doi.org/10.1080/14786435.2017.1302613.

[15] L. Aderras, A. Bah, E. Feddi, F. Dujardin, C.A. Duque, Stark-shift of impurity fundamental state in a lens shaped quantum dot, Physica E Low Dimens Syst Nanostruct. 89 (2017) 119–123. https://doi.org/10.1016/j.physe.2017.02.012.

[16] A. el Aouami, E. Feddi, A. Talbi, F. Dujardin, C.A. Duque, Electronic state and photoionization cross section of a single dopant in GaN/InGaN core/shell quantum dot under magnetic field and hydrostatic pressure, Appl Phys A Mater Sci Process. 124 (2018). https://doi.org/10.1007/s00339-018-1856-2.

[17] H. el Ghazi, A. Jorio, I. Zorkani, Pressure-dependent shallow donor binding energy in InGaN/GaN square QWWs, Physica B Condens Matter. 410 (2013) 49–52. https://doi.org/10.1016/j.physb.2012.10.027.

[18] A. Sali, H. Satori, The combined effect of pressure and temperature on the impurity binding energy in a cubic quantum dot using the FEM simulation, Superlattices Microstruct. 69 (2014) 38–52. https://doi.org/10.1016/j.spmi.2014.01.011.

[19] R. Khordad, H. Bahramiyan, Study of impurity position effect in pyramid and cone like quantum dots, EPJ Applied Physics. 67 (2014). https://doi.org/10.1051/epjap/2014140080.

[20] R. En-nadir, H. el Ghazi, A. Jorio, I. Zorkani, Ground-state Shallow-donor Binding Energy in (In,Ga)N/GaN Double QWs Under Temperature, Size, and the Impurity Position Effects, Journal of Modeling and Simulation of Materials. 4 (2021) 1–6. https://doi.org/10.21467/jmsm.4.1.1-6.

[21] R. En-nadir, H. el Ghazi, W. Belaid, A. Jorio, I. Zorkani, H.Ş. Kiliç, Ground and first five low-lying excited states related optical absorption in In.1Ga.9N/GaN double quantum wells: Temperature and coupling impacts, Solid State Commun. 338 (2021). https://doi.org/10.1016/j.ssc.2021.114464.

[22] W. Belaid, H. el Ghazi, I. Zorkani, A. Jorio, Impact of QW coupling on the binding energy in InGaN/GaN under the effects of the size, the impurity and the internal composition, MATEC Web of Conferences. 330 (2020) 01012. https://doi.org/10.1051/matecconf/202033001012.

[23] K. Batra, V. Prasad, K. Batra, V. Prasad, Finite difference calculation of optical properties of hydrogenic impurity in spherical quantum dot with parabolic confinement, Revista Mexicana de Física E. 64 (2018) 7–15.

[24] G.V.B. de Souza, A. Bruno-Alfonso, Donor energy levels of a spherical quantum dot subject to parallel electric and magnetic fields, in: 2011.

[25] M. Hu, Z. Jia, H. Wang, Q. Gong, The effect of hydrostatic pressure and temperature on impurity states in a cylindrical quantum dot, J Comput Electron. 20 (2021) 2369–2378. https://doi.org/10.1007/s10825-021-01771-y.

[26] S.S. Li, J.B. Xia, Application of Plane Wave Method to the Calculation of Electronic States of Nano-Structures, Chinese Physics Letters. 23 (2006) 1896. https://doi.org/10.1088/0256-307X/23/7/066.

[27] S.S. Li, J.B. Xia, Electronic states of a hydrogenic donor impurity in semiconductor nano-structures, Phys Lett A. 366 (2007) 120–123. https://doi.org/10.1016/J.PHYSLETA.2007.02.028.

[28] C. Bose, C.K. Sarkar, Perturbation calculation of donor states in a spherical quantum dot, Solid State Electron. 42 (1998) 1661–1663. https://doi.org/10.1016/S0038-1101(98)00126-9.

[29] A. Boda, Magnetic moment and susceptibility of an impurity in a parabolic quantum dot, J Magn Magn Mater. 483 (2019) 83–88. https://doi.org/10.1016/j.jmmm.2019.03.067.

[30] M. Şahin, M. Tomak, Electronic structure of a many-electron spherical quantum dot with an impurity, Phys Rev B Condens Matter Mater Phys. 72 (2005) 125323. https://doi.org/10.1103/PHYSREVB.72.125323/FIGURES/9/MEDIUM.

[31] S. Wei, Q. Chang, Hydrogenic impurity states in zinc-blende symmetric InGaN/GaN multiple quantum dots, Physica E Low Dimens Syst Nanostruct. 43 (2010) 354–358. https://doi.org/10.1016/J.PHYSE.2010.08.016.

[32] E. Sadeghi, E. Naghdi, Effect of electric and magnetic fields on impurity binding energy in zinc-blend symmetric InGaN/GaN multiple quantum dots, Nano Converg. 1 (2014) 25. https://doi.org/10.1186/s40580-014-0025-3.

[33] J.J. Liu, M. Shen, S.W. Wang, The influence of compressive stress on shallow-donor impurity states in symmetric GaAs-Ga1-xAlxAs double quantum dots, J Appl Phys. 101 (2007). https://doi.org/10.1063/1.2717584.

[34] J. liang Zheng, Binding energy of hydrogenic impurity in GaAs / Ga1 - x Alx As multi-quantum-dot structure, Physica E Low Dimens Syst Nanostruct. 40 (2008) 2879–2883. https://doi.org/10.1016/j.physe.2008.01.017.

[35] J.E. Northrup, C.L. Chua, Z. Yang, T. Wunderer, M. Kneissl, N.M. Johnson, T. Kolbe, Effect of strain and barrier composition on the polarization of light emission from AlGaN/AlN quantum wells, Appl Phys Lett. 100 (2012) 021101. https://doi.org/10.1063/1.3675451.

[36] K. Shojiki, R. Ishii, K. Uesugi, M. Funato, Y. Kawakami, H. Miyake, Impact of face-to-face annealed sputtered AlN on the optical properties of AlGaN multiple quantum wells, AIP Adv. 9 (2019). https://doi.org/10.1063/1.5125799.

[37] R.G. Banal, M. Funato, Y. Kawakami, Characteristics of high Al-content AlGaN/AlN quantum wells fabricated by modified migration enhanced epitaxy, Physica Status Solidi c. 7 (2010) 2111–2114. https://doi.org/10.1002/PSSC.200983609.

[38] G. Salis, K. Ensslin, K.B. Campman, K. Maranowski, A.C. Gossard, Wave-function spectroscopy in parabolic quantum wells, Physica B Condens Matter. 249–251 (1998) 941–945. https://doi.org/10.1016/S0921-4526(98)00350-0.

[39] E. Kasapoglu, Binding energy of donor impurities in double inverse parabolic quantum well under electric field, Physica E Low Dimens Syst Nanostruct. 41 (2009) 1222–1225. https://doi.org/10.1016/j.physe.2009.02.003.

[40] H. Akbas, C. Dane, I. Erdogan, O. Akankan, Hydrogenic donor in asymmetric AlxLGa 1 - XLAs/GaAs/AlxRGa 1 -xRAs quantum wells, Physica E Low Dimens Syst Nanostruct. 60 (2014) 196–199. https://doi.org/10.1016/j.physe.2014.03.003.

[41] H. Akbas, S. Sucu, S. Minez, C. Dane, O. Akankan, I. Erdogan, Ground state normalized binding energy of impurity in asymmetric quantum wells under hydrostatic pressure, Superlattices Microstruct. 94 (2016) 131–137. https://doi.org/10.1016/j.spmi.2016.04.011.

[42] J. Zhu, S.L. Ban, S.H. Ha, Built-in electric field effect on donor impurities in strained wurtzite GaN/AlGaN asymmetric double quantum wells, Modern Physics Letters B. 26 (2012). https://doi.org/10.1142/S0217984912501722.

[43] C.Y. Yeh, Z.W. Lu, S. Froyen, A. Zunger, Zinc-blende–wurtzite polytypism in semiconductors, Phys Rev B. 46 (1992) 10086. https://doi.org/10.1103/PhysRevB.46.10086.

[44] J. Renard, G. Tourbot, D. Sam-Giao, C. Bougerol, B. Daudin, B. Gayral, Optical spectroscopy of cubic GaN in nanowires, Appl Phys Lett. 97 (2010) 081910. https://doi.org/10.1063/1.3478004.

[45] V. Soukhoveev, V. Ivantsov, Y. Melnik, A. Davydov, D. Tsvetkov, K. Tsvetkova, I. Nikitina, A. Zubrilov, A. Lavrentiev, V.A. Dmitriev, Characterization of 2.5 Inch Diameter Bulk GaN Grown from Melt-Solution, 188 (2001). https://www.nist.gov/publications/characterization-25-inch-diameter-bulk-gan-grown-melt-solution (accessed August 16, 2022).

[46] S. Strite, J. Ruan, Z. Li, A. Salvador, H. Chen, D.J. Smith, W.J. Choyke, H. Morkoç, An investigation of the properties of cubic GaN grown on GaAs by plasma-assisted molecular-beam epitaxy, Journal of Vacuum Science & Technology B: Microelectronics and Nanometer Structures Processing, Measurement, and Phenomena. 9 (1998) 1924. https://doi.org/10.1116/1.585381.

[47] T. Lei, T.D. Moustakas, R.J. Graham, Y. He, S.J. Berkowitz, Epitaxial growth and characterization of zinc-blende gallium nitride on (001) silicon, J Appl Phys. 71 (1992) 4933. https://doi.org/10.1063/1.350642.

[48] D.P. Xu, Y.T. Wang, H. Yang, S.F. Li, D.G. Zhao, Y. Fu, S.M. Zhang, R.H. Wu, Q.J. Jia, W.L. Zheng, X.M. Jiang, Anomalous strains in the cubic-phase GaN films grown on GaAs (001) by metalorganic chemical vapor deposition, J Appl Phys. 88 (2000) 3762. https://doi.org/10.1063/1.1288779.

[49] R.C. Powell, N.E. Lee, Y.W. Kim, J.E. Greene, Heteroepitaxial wurtzite and zinc-blende structure GaN grown by reactive-ion molecular-beam epitaxy: Growth kinetics, microstructure, and properties, J Appl Phys. 73 (1998) 189. https://doi.org/10.1063/1.353882.

[50] H. Okumura, H. Hamaguchi, T. Koizumi, K. Balakrishnan, Y. Ishida, M. Arita, S. Chichibu, H. Nakanishi, T. Nagatomo, S. Yoshida, Growth of cubic III-nitrides by gas source MBE using atomic nitrogen plasma: GaN, AlGaN and AlN, J Cryst Growth. 189–190 (1998) 390–394. https://doi.org/10.1016/S0022-0248(98)00321-2.

[51] S.K. Pugh, D.J. Dugdale, S. Brand, R.A. Abram, Electronic structure calculations on nitride semiconductors, Semicond Sci Technol. 14 (1999) 23. https://doi.org/10.1088/0268-1242/14/1/003.

[52] S. Strite, H. Morkoç, GaN, AlN, and InN: A review, Journal of Vacuum Science & Technology B: Microelectronics and Nanometer Structures Processing, Measurement, and Phenomena. 10 (1998) 1237. https://doi.org/10.1116/1.585897.

[53] R.B. Araujo, J.S. de Almeida, A. Ferreira Da Silva, Electronic properties of III-nitride semiconductors: A first-principles investigation using the Tran-Blaha modified Becke-Johnson potential, J Appl Phys. 114 (2013) 183702. https://doi.org/10.1063/1.4829674.

[54] R. Dingle, D.D. Sell, S.E. Stokowski, M. Ilegems, Absorption, Reflectance, and Luminescence of GaN Epitaxial Layers, Phys Rev B. 4 (1971) 1211. https://doi.org/10.1103/PhysRevB.4.1211.

[55] S.C. Jain, M. Willander, J. Narayan, R. van Overstraeten, III–nitrides: Growth, characterization, and properties, J Appl Phys. 87 (2000) 965. https://doi.org/10.1063/1.371971.

[56] L. Cláudio De Carvalho, A. Schleife, F. Fuchs, F. Bechstedt, Valence-band splittings in cubic and hexagonal AlN, GaN, and InN, Appl Phys Lett. 97 (2010) 232101. https://doi.org/10.1063/1.3524234.

[57] I. Vurgaftman, J.R. Meyer, L.R. Ram-Mohan, Band parameters for III–V compound semiconductors and their alloys, J Appl Phys. 89 (2001) 5815. https://doi.org/10.1063/1.1368156.

[58] P. Perlin, E. Litwin-Staszewska, B. Suchanek, W. Knap, J. Camassel, T. Suski, R. Piotrzkowski, I. Grzegory, S. Porowski, E. Kaminska, J.C. Chervin, Determination of the effective mass of GaN from infrared reflectivity and Hall effect, Appl Phys Lett. 68 (1998) 1114. https://doi.org/10.1063/1.115730.

[59] M. Drechsler, D.M. Hofmann, B.K. Meyer, T. Detchprohm, H. Amano, I. Akasaki, Determination of the Conduction Band Electron Effective Mass in Hexagonal Gan, Jpn J Appl Phys. 34 (1995) L1177–L1179. https://doi.org/10.1143/JJAP.34.L1178/XML.

[60] J.S. Im, A. Moritz, F. Steuber, V. Härle, F. Scholz, A. Hangleiter, Radiative carrier lifetime, momentum matrix element, and hole effective mass in GaN, Appl Phys Lett. 70 (1998) 631. https://doi.org/10.1063/1.118293.

[61] M. Suzuki, T. Uenoyama, A. Yanase, First-principles calculations of effective-mass parameters of AlN and GaN, Phys Rev B. 52 (1995) 8132. https://doi.org/10.1103/PhysRevB.52.8132.

[62] A. Salvador, G. Liu, W. Kim, Ö. Aktas, A. Botchkarev, H. Morkoç, Properties of a Si doped GaN/AlGaN single quantum well, Appl Phys Lett. 67 (1998) 3322. https://doi.org/10.1063/1.115234.

[63] A.F. Wright, Elastic properties of zinc-blende and wurtzite AlN, GaN, and InN, J Appl Phys. 82 (1998) 2833. https://doi.org/10.1063/1.366114.

[64] Y. Takagi, M. Ahart, T. Azuhata, T. Sota, K. Suzuki, S. Nakamura, Brillouin scattering study in the GaN epitaxial layer, Physica B Condens Matter. 219–220 (1996) 547–549. https://doi.org/10.1016/0921-4526(95)00807-1.

[65] A. Polian, M. Grimsditch, I. Grzegory, Elastic constants of gallium nitride, J Appl Phys. 79 (1998) 3343. https://doi.org/10.1063/1.361236.

[66] M. Yamaguchi, T. Yagi, T. Azuhata, T. Sota, K. Suzuki, S. Chichibu, S. Nakamura, Brillouin scattering study of gallium nitride: elastic stiffness constants, Journal of Physics: Condensed Matter. 9 (1997) 241. https://doi.org/10.1088/0953-8984/9/1/025.

[67] C. Deger, E. Born, H. Angerer, O. Ambacher, M. Stutzmann, J. Hornsteiner, E. Riha, G. Fischerauer, Sound velocity of AlxGa1-xN thin films obtained by surface acoustic-wave measurements, Appl Phys Lett. 72 (1998) 2400–2402. https://doi.org/10.1063/1.121368.

[68] K. Kim, W.R.L. Lambrecht, B. Segall, Elastic constants and related properties of tetrahedrally bonded BN, AlN, GaN, and InN, Phys Rev B Condens Matter Mater Phys. 53 (1996) 16310–16326. https://doi.org/10.1103/PHYSREVB.53.16310.

[69] L.E. McNeil, M. Grimsditch, R.H. French, Vibrational Spectroscopy of Aluminum Nitride, Journal of the American Ceramic Society. 76 (1993) 1132–1136. https://doi.org/10.1111/J.1151-2916.1993.TB03730.X.

[70] A. Hangleiter, J.S. Im, H. Kollmer, S. Heppel, J. Off, F. Scholz, The role of piezoelectric fields in GaN-based quantum wells, Materials Research Society Internet Journal of Nitride Semiconductor Research. 3 (1998) e15. https://doi.org/10.1557/S1092578300000879.

[71] E.T. Yu, G.J. Sullivan, P.M. Asbeck, C.D. Wang, D. Qiao, S.S. Lau, Measurement of piezoelectrically induced charge in GaN/AlGaN heterostructure field-effect transistors, Appl Phys Lett. 71 (1997) 2794–2796. https://doi.org/10.1063/1.120138.

[72] J. Simon, Etude des propriétés optiques de nanostructures quantiques à base de nitrures d'éléments III, Grenoble university, 2001. https://www.theses.fr/2001GRE10115 (accessed August 15, 2022).

[73] F. Bernardini, V. Fiorentini, D. Vanderbilt, Spontaneous polarization and piezoelectric constants of III-V nitrides, Phys Rev B Condens Matter Mater Phys. 56 (1997) R10024–R10027. https://doi.org/10.1103/PHYSREVB.56.R10024.

[74] F. Bernardini, V. Fiorentini, Nonlinear macroscopic polarization in III-V nitride alloys, Phys Rev B. 64 (2001) 085207. https://doi.org/10.1103/PhysRevB.64.085207.

[75] G. Martin, A. Botchkarev, A. Rockett, H. Morkoç, Valence-band discontinuities of wurtzite GaN, AlN, and InN heterojunctions measured by x-ray photoemission spectroscopy, Appl Phys Lett. 68 (1998) 2541. https://doi.org/10.1063/1.116177.

[76] D.C. Look, R.J. Molnar, Degenerate layer at GaN/sapphire interface: Influence on Hall-effect measurements, Appl Phys Lett. 70 (1997) 3377–3379. https://doi.org/10.1063/1.119176.

[77] W. Götz, L.T. Romano, J. Walker, N.M. Johnson, R.J. Molnar, Hall-effect analysis of GaN films grown by hydride vapor phase epitaxy, Appl Phys Lett. 72 (1998) 1214–1216. https://doi.org/10.1063/1.121017.

[78] H. Brooks, Scattering by ionized impurities in semiconductors, Physical Review. 83 (1951).

[79] G. Bastard, wave mechanics applied to semiconductor heterostructures, 1990.

[80] W. Kohn, Shallow Impurity States in Silicon and Germanium, Solid State Physics - Advances in Research and Applications. 5 (1957) 257–320. https://doi.org/10.1016/S0081-1947(08)60104-6.

[81] G. Bastard, wave mechanics applied to semiconductor heterostructures, 1990.

[82] C.J. Delerue, M. Lannoo, Nanostructures: Theory and Modeling, springer, Berlin, 2013.

[83] J.M. Luttinger, W. Kohn, Motion of Electrons and Holes in Perturbed Periodic Fields, Physical Review. 97 (1955) 869–883. https://doi.org/10.1103/PhysRev.97.869.

[84] G.H. Wannier, The Structure of Electronic Excitation Levels in Insulating Crystals, Physical Review. 52 (1937) 191–197. https://doi.org/10.1103/PhysRev.52.191.

[85] G.H. Wannier, Elements of solid state theory, second, Cambridge University Press, 1959.

[86] S. Sze, Y. Li, K. Ng, Physics of semiconductor devices, 2021.

[87] J. Pankove, Luminescence in GaN, J Lumin. 7 (1973) 114–126. https://doi.org/10.1016/0022-2313(73)90062-8.

[88] H.P. Maruska, D.A. Stevenson, J.I. Pankove, Violet luminescence of Mg-doped GaN, Appl Phys Lett. 22 (1973) 303–305. https://doi.org/10.1063/1.1654648.

[89] N. Shuji, P. Stephen, F. Gerhard, The Blue Laser Diode, second, Springer, Berlin, 1997.

[90] A. Chitnis, V. Adivarahan, J.P. Zhang, M. Shatalov, S. Wu, J. Yang, G. Simin, M.A. Khan, X. Hu, Q. Fareed, R. Gaska, M.S. Shur, Milliwatt power AlGaN quantum well deep ultraviolet light emitting diodes, Physica Status Solidi A Appl Res. 200 (2003) 99–101. https://doi.org/10.1002/PSSA.200303420.

[91] T. Whitaker, SUVOS pushes UV LEDs and lasers to shorter wavelength, Compound Semiconductor , 2004.

[92] T. Mukai, M. Yamada, S. Nakamura, Characteristics of InGaN-based UV/blue/green/amber/red light-emitting diodes, Japanese Journal of Applied Physics, Part 1: Regular Papers and Short Notes and Review Papers. 38 (1999) 3976–3981. https://doi.org/10.1143/JJAP.38.3976/XML.

[93] A. Žukauskas, M.S. Shur, R. Gaska, Light-Emitting Diodes: Progress in Solid-State Lighting, MRS Bull. 26 (2001) 764–769. https://doi.org/10.1557/MRS2001.203.

[94] G. Bernard, Low-Dimensional Nitride, 2002.

[95] S. Nakamura, The roles of structural imperfections in InGaN-based blue light- emitting diodes and laser diodes, Science (1979). 281 (1998) 956–961. https://doi.org/10.1126/SCIENCE.281.5379.956.

[96] S. Chichibu, T. Azuhata, T. Sota, S. Nakamura, Spontaneous emission of localized excitons in InGaN single and multiquantum well structures, Appl Phys Lett. 69 (1998) 4188. https://doi.org/10.1063/1.116981.

[97] S. Chichibu, T. Azuhata, T. Sota, S. Nakamura, Luminescences from localized states in InGaN epilayers, Appl Phys Lett. 70 (1997) 2822–2824. https://doi.org/10.1063/1.119013.

[98] S. Chichibu, K. Wada, S. Nakamura, Spatially resolved cathodoluminescence spectra of InGaN quantum wells, Appl Phys Lett. 71 (1997) 2346–2348. https://doi.org/10.1063/1.120025.

[99] Y. Narukawa, Y. Kawakami, S. Fujita, S. Fujita, S. Nakamura, Recombination dynamics of localized excitons iN multiple quantum wells, Phys Rev B Condens Matter Mater Phys. 55 (1997) R1938–R1941. https://doi.org/10.1103/PHYSREVB.55.R1938.

[100] Y. Narukawa, Y. Kawakami, M. Funato, S. Fujita, S. Fujita, S. Nakamura, Role of self-formed InGaN quantum dots for exciton localization in the purple laser diode emitting at 420 nm, Appl Phys Lett. 70 (1997) 981–983. https://doi.org/10.1063/1.118455.

[101] S. Nakamura, M. Senoh, S. Nagahama, N. Iwasa, T. Yamada, T. Matsushita, H. Kiyoku, Y. Sugimoto, T. Kozaki, H. Umemoto, M. Sano, K. Chocho, InGaN/GaN/AlGaN-Based Laser Diodes with Modulation-Doped Strained-Layer Superlattices, Jpn J Appl Phys. 36 (1997) L1568–L1571. https://doi.org/10.1143/JJAP.36.L1568/META.

[102] M. Leroux, Matériaux semi-conducteurs III-V, II-VI et nitrures pour l'optoélectronique, Hermes publications, Paris, 2003.

[103] D.A. Steigerwald, J.C. Bhat, D. Collins, R.M. Fletcher, M.O. Holcomb, M.J. Ludowise, P.S. Martin, S.L. Rudaz, Illumination with solid state lighting technology, IEEE Journal on Selected Topics in Quantum

Electronics. 8 (2002) 310–320.
https://doi.org/10.1109/2944.999186.

[104] B. Damilano, N. Grandjean, C. Pernot, J. Massies, Monolithic white light emitting diodes based on InGaN/GaN multiple-quantum wells, Japanese Journal of Applied Physics, Part 2: Letters. 40 (2001).
https://doi.org/10.1143/JJAP.40.L918/META.

[105] F. Liang, D. Zhao, D. Zhao, Z. Liu, P. Chen, J. Yang, Improved performance of GaN-based blue laser diodes using asymmetric multiple quantum wells without the first quantum barrier layer, Optics Express, Vol. 30, Issue 6, Pp. 9913-9923. 30 (2022) 9913–9923.
https://doi.org/10.1364/OE.453611.

[106] E. Rosencher, B. Vinter, Optoélectronique, édition Dunod, 2002.

[107] E. Monroy, F. Omnès, F. Calle, Wide-bandgap semiconductor ultraviolet photodetectors, Semicond Sci Technol. 18 (2003) R33.
https://doi.org/10.1088/0268-1242/18/4/201.

[108] O. Al-Zuhairi, A. Shuhaimi, N. Nayan, A. Azman, A. Kamarudzaman, O. Alobaidi, M. Ghanim, E.T. Abdullah, Y. Zhu, Non-Polar Gallium Nitride for Photodetection Applications: A Systematic Review, Coatings. 12 (2022) 275.
https://doi.org/10.3390/coatings12020275.

[109] O. Jani, I. Ferguson, C. Honsberg, S. Kurtz, Design and characterization of GaNInGaN solar cells, Appl Phys Lett. 91 (2007).
https://doi.org/10.1063/1.2793180.

[110] C.J. Neufeld, N.G. Toledo, S.C. Cruz, M. Iza, S.P. DenBaars, U.K. Mishra, High quantum efficiency InGaN/GaN solar cells with 2.95 eV band gap, Appl Phys Lett. 93 (2008).
https://doi.org/10.1063/1.2988894.

[111] J.J. Xue, D.J. Chen, B. Liu, Z.L. Xie, R.L. Jiang, R. Zhang, Y.D. Zheng, Au/Pt/InGaN/GaN Heterostructure Schottky Prototype Solar Cell, Chinese Physics Letters. 26 (2009) 098102.
https://doi.org/10.1088/0256-307X/26/9/098102.

[112] H. Çakmak, E. Arslan, M. Rudziński, P. Demirel, H.E. Unalan, W. Strupiński, R. Turan, M. Öztürk, E. Özbay, Indium rich InGaN solar cells grown by MOCVD, Journal of Materials Science: Materials in Electronics. 25 (2014) 3652–3658.
https://doi.org/10.1007/S10854-014-2070-4.

[113] R. Dahal, J. Li, K. Aryal, J.Y. Lin, H.X. Jiang, InGaN/GaN multiple quantum well concentrator solar cells, Appl Phys Lett. 97 (2010).
https://doi.org/10.1063/1.3481424.

[114] A. Asgari, K. Khalili, Temperature dependence of InGaN/GaN multiple quantum well based high efficiency solar cell, Solar Energy Materials and Solar Cells. 95 (2011) 3124–3129.
https://doi.org/10.1016/J.SOLMAT.2011.07.001.

[115] E. Matioli, C. Neufeld, M. Iza, S.C. Cruz, A.A. Al-Heji, X. Chen, R.M. Farrell, S. Keller, S. DenBaars, U. Mishra, S. Nakamura, J. Speck, C. Weisbuch, High internal and external quantum efficiency InGaN/GaN solar cells, Appl Phys Lett. 98 (2011).
https://doi.org/10.1063/1.3540501.

[116] C.-C. Yang, C.H. Jang, J.-K. Sheu, M.-L. Lee, S.-J. Tu, F.-W. Huang, Y.-H. Yeh, W.-C. Lai, R.R. King, A. Boca, W. Hong, X.Q. Liu, D. Bhusari, D. Larrabee, K.M. Edmondson, D.C. Law, C.M. Fetzer, S. Mesropian, N.H. Karam, J. Wu, W. Walukiewicz, K.M. Yu, W. Shan, J.W. Ager III, E.E. Haller, H. Lu, W.J. Schaff, W.K. Metzger, S. Kurtz, Characteristics of InGaN-based concentrator solar cells operating under 150X solar concentration, Optics Express, Vol. 19, Issue S4, Pp. A695-A700. 19 (2011) A695–A700.
https://doi.org/10.1364/OE.19.00A695.

[117] Z.W. Zheng, M.H. Lai, L.Y. Ying, B.P. Zhang, High-efficiency vertical-type InGaN/GaN multiple quantum well solar cells using aluminum reflectors, 16th International Conference on Nanotechnology - IEEE NANO 2016. (2016) 91–93. https://doi.org/10.1109/NANO.2016.7751339.

[118] S. Liu, Q. Wang, H. Xiao, K. Wang, C. Wang, X. Wang, W. Ge, Z. Wang, Optimization of growth and fabrication techniques to enhance the InGaN/GaN multiple quantum well solar cells performance, Superlattices Microstruct. 109 (2017) 194–200. https://doi.org/10.1016/J.SPMI.2017.05.014.

[119] X. Cai, S. Zeng, B. Zhang, Favourable photovoltaic effects in InGaN pin homojunction solar cell, Search.Proquest.Com. 45 (2009). https://search.proquest.com/openview/261335866a3feae59788d68c4cf15eb2/1?pq-origsite=gscholar&cbl=1936364 (accessed August 15, 2022).

[120] S.W. Zeng, B.P. Zhang, J.W. Sun, J.F. Cai, C. Chen, J.Z. Yu, Substantial photo-response of InGaN p–i–n homojunction solar cells, Semicond Sci Technol. 24 (2009) 055009. https://doi.org/10.1088/0268-1242/24/5/055009.

[121] M.R. Islam, M.R. Kaysir, M.J. Islam, A. Hashimoto, A. Yamamoto, MOVPE Growth of InxGa1−xN ($x \sim 0.4$) and Fabrication of Homo-junction Solar Cells, J Mater Sci Technol. 29 (2013) 128–136. https://doi.org/10.1016/J.JMST.2012.12.005.

[122] C.A.M. Fabien, W.A. Doolittle, Guidelines and limitations for the design of high-efficiency InGaN single-junction solar cells, Solar Energy Materials and Solar Cells. 130 (2014) 354–363. https://doi.org/10.1016/J.SOLMAT.2014.07.018.

[123] L. Hsu, W. Walukiewicz, Modeling of InGaN/Si tandem solar cells, J Appl Phys. 104 (2008) 024507. https://doi.org/10.1063/1.2952031.

[124] X. Zhang, X. Wang, H. Xiao, C. Yang, J. Ran, C. Wang, Q. Hou, J. Li, Z. Wang, Theoretical design and performance of InxGa1−xN two-junction solar cells, J Phys D Appl Phys. 41 (2008) 245104. https://doi.org/10.1088/0022-3727/41/24/245104.

[125] N.G. Young, E.E. Perl, R.M. Farrell, M. Iza, S. Keller, J.E. Bowers, S. Nakamura, S.P. Denbaars, J.S. Speck, High-performance broadband optical coatings on InGaN/GaN solar cells for multijunction device integration, Appl Phys Lett. 104 (2014). https://doi.org/10.1063/1.4873117.

[126] H. el Ghazi, A. John Peter, Photo-ionization cross-section of donor-related in (In,Ga)N/GaN core/shell under hydrostatic pressure and electric field effects, Superlattices Microstruct. 104 (2017) 222–231. https://doi.org/10.1016/J.SPMI.2017.02.013.

[127] N. Duxbury, U. Bangert, P. Dawson, E.J. Thrush, W. van der Stricht, K. Jacobs, I. Moerman, Indium segregation in InGaN quantum-well structures, Appl Phys Lett. 76 (2000) 1600–1602. https://doi.org/10.1063/1.126108.

[128] Y.S. Lin, K.J. Ma, C. Hsu, S.W. Feng, Y.C. Cheng, C.C. Liao, C.C. Yang, C.C. Chou, C.M. Lee, J.I. Chyi, Dependence of composition fluctuation on indium content in InGaN/GaN multiple quantum wells, Appl Phys Lett. 77 (2000) 2988. https://doi.org/10.1063/1.1323542.

[129] K. Watanabe, N. Nakanishi, T. Yamazaki, J.R. Yang, S.Y. Huang, K. Inoke, J.T. Hsu, R.C. Tu, M. Shiojiri, Atomic-scale strain field and in atom distribution in multiple quantum wells InGaN/GaN, Appl Phys Lett. 82 (2003) 715–717. https://doi.org/10.1063/1.1542930.

[130] M. Takeguchi, M.R. McCartney, D.J. Smith, Mapping in concentration, strain, and internal electric field in InGaN/GaN quantum well structure, Appl Phys Lett. 84 (2004) 2103–2105. https://doi.org/10.1063/1.1689400.

[131] V. Potin, E. Hahn, A. Rosenauer, D. Gerthsen, B. Kuhn, F. Scholz, A. Dussaigne, B. Damilano, N. Grandjean, Comparison of the In distribution in InGaN/GaN quantum well structures grown by molecular beam epitaxy and metalorganic vapor phase epitaxy, J Cryst Growth. 262 (2004) 145–150. https://doi.org/10.1016/J.JCRYSGRO.2003.10.082.

[132] S. Chichibu, T. Sota, K. Wada, S. Nakamura, Exciton localization in InGaN quantum well devices, Journal of Vacuum Science & Technology B: Microelectronics and Nanometer Structures Processing, Measurement, and Phenomena. 16 (1998) 2204. https://doi.org/10.1116/1.590149.

[133] N. Grandjean, B. Damilano, J. Massies, Group-III nitride quantum heterostructures grown by molecular beam epitaxy, Journal of Physics: Condensed Matter. 13 (2001) 6945. https://doi.org/10.1088/0953-8984/13/32/305.

[134] S. Dhar, U. Jahn, O. Brandt, P. Waltereit, K.H. Ploog, Influence of exciton localization on the quantum efficiency of GaN/(In,Ga)N multiple quantum wells grown by molecular-beam epitaxy, Appl Phys Lett. 81 (2002) 673–675. https://doi.org/10.1063/1.1493237.

[135] G.R. Mutta, P. Ruterana, J.L. Doualan, M.P. Chauvat, F. Ivaldi, S. Kret, N.A.K. Kaufmann, A. Dussaigne, D. Martin, N. Grandjean, Investigation of the In composition in InGaN/GaN quantum wells deposited by MOVPE and/or MBE with emission from violet to green, Phys Status Solidi B Basic Res. 248 (2011) 1187–1190. https://doi.org/10.1002/PSSB.201000801.

[136] D.M. Graham, A. Soltani-Vala, P. Dawson, M.J. Godfrey, T.M. Smeeton, J.S. Barnard, M.J. Kappers, C.J. Humphreys, E.J. Thrush, Optical and microstructural studies of InGaNGaN single-quantum-well structures, J Appl Phys. 97 (2005). https://doi.org/10.1063/1.1897070.

[137] H. Masui, H. Yamada, K. Iso, S. Nakamura, S.P. Denbaars, Optical polarization characteristics of m-oriented InGaN/GaN light-emitting diodes with various indium compositions in single-quantum-well structure, J Phys D Appl Phys. 41 (2008) 225104. https://doi.org/10.1088/0022-3727/41/22/225104.

[138] H. Yamada, K. Iso, M. Saito, H. Masui, K. Fujito, S.P. DenBaars, S. Nakamura, Compositional dependence of nonpolar m-plane inxGa 1-xN/GaN light emitting diodes, Applied Physics Express. 1 (2008) 0411011–0411013. https://doi.org/10.1143/APEX.1.041101/META.

[139] C. Xia, Y. Jia, S. Wei, H.N. Spector, Finite barrier width effects on exciton states and optical properties in wurtzite InGaN/GaN quantum well, J Lumin. 132 (2012) 607–611. https://doi.org/10.1016/J.JLUMIN.2011.09.055.

[140] L. Guo, X. Wang, H. Xiao, B. Wang, The influence of internal electric fields on the transition energy of InGaN/gaN quantum well, J Cryst Growth. 298 (2007) 522–526. https://doi.org/10.1016/J.JCRYSGRO.2006.11.078.

[141] I. Vurgaftman, J.R. Meyer, Band parameters for nitrogen-containing semiconductors, J Appl Phys. 94 (2003) 3675–3696. https://doi.org/10.1063/1.1600519.

[142] P.G. Moses, C.G. van de Walle, Band bowing and band alignment in InGaN alloys, Appl Phys Lett. 96 (2010). https://doi.org/10.1063/1.3291055.

[143] H. el Ghazi, A. Jorio, I. Zorkani, Linear and nonlinear intra-conduction band optical absorption in (In,Ga)N/GaN spherical QD under hydrostatic pressure, Opt Commun. 331 (2014) 73–76. https://doi.org/10.1016/j.optcom.2014.05.055.

[144] C. Xia, Z. Zeng, Q. Chang, S. Wei, Donor impurity states in zinc-blende InGaN/GaN asymmetric coupled quantum dots: Hydrostatic pressure effect, Physica E Low Dimens Syst Nanostruct. 42 (2010) 2041–2046. https://doi.org/10.1016/j.physe.2010.03.022.

[145] Y. Peter, M. Cardona, Fundamentals of semiconductors: physics and materials properties, 2010.

[146] P. Baser, S. Elagoz, N. Baraz, Hydrogenic impurity states in zinc-blende InxGa 1-xN/GaN in cylindrical quantum well wires under hydrostatic pressure, Physica E Low Dimens Syst Nanostruct. 44 (2011) 356–360.
https://doi.org/10.1016/j.physe.2011.08.027.

[147] S.Q. Wang, H.Q. Ye, Ab initio investigation of the pressure dependences of phonon and dielectric properties for III–V semiconductors, Journal of Physics: Condensed Matter. 17 (2005) 4475.
https://doi.org/10.1088/0953-8984/17/28/007.

[148] S.P. Łepkowski, J.A. Majewski, G. Jurczak, Nonlinear elasticity in III-N compounds: Ab initio calculations, Phys Rev B Condens Matter Mater Phys. 72 (2005).
https://doi.org/10.1103/PhysRevB.72.245201.

[149] C. Xia, Z. Zeng, S. Wei, Donor impurity in InGaN/GaN asymmetric multiple quantum wells, Physica E Low Dimens Syst Nanostruct. 42 (2010) 2416–2419.
https://doi.org/10.1016/J.PHYSE.2010.05.028.

[150] E. Kasapoglu, F. Ungan, H. Sari, I. Sökmen, Binding energies of donor impurities in modulation-doped GaAs/Alx Ga1 - x As double quantum wells under an electric field, Superlattices Microstruct. 45 (2009) 618–623.
https://doi.org/10.1016/j.spmi.2009.02.011.

[151] S. Baskoutas, Z. Zeng, C.S. Garoufalis, G. Bester, Tuning of the optical emission polarization of ZnO nanorods by an applied hydrostatic pressure, Journal of Physical Chemistry C. 116 (2012) 26592–26597.
https://doi.org/10.1021/JP307269D.

[152] Z. Zeng, C.S. Garoufalis, S. Baskoutas, G. Bester, Electronic and optical properties of ZnO quantum dots under hydrostatic pressure, Phys Rev B Condens Matter Mater Phys. 87 (2013).
https://doi.org/10.1103/PhysRevB.87.125302.

[153] N. Raigoza, A.L. Morales, C.A. Duque, Infinite Potential Barrier and Hydrostatic Pressure Effects on Impurity-Related Optical Absorption Spectra in GaAs Double Quantum Wells, 2006.

[154] C. Xia, Z. Zeng, S. Wei, Electric field effects on optical properties in zinc-blende InGaN/GaN quantum dot, J Lumin. 131 (2011) 623–627.
https://doi.org/10.1016/j.jlumin.2010.11.003.

[155] T. Wang, Z. Zeng, C. Xia, S. Wei, Hydrostatic pressure effect on the donor impurity states in asymmetric multiple quantum wells, Superlattices Microstruct. 49 (2011) 365–372.
https://doi.org/10.1016/j.spmi.2010.11.010.

[156] H. el Ghazi, A. Jorio, Temperature dependence of interband recombination energy in symmetric (In,Ga)N spherical quantum dot-quantum well, Physica B Condens Matter. 432 (2014) 64–66.
https://doi.org/10.1016/j.physb.2013.09.017.

[157] A. Elabsy, Effect of the Gamma-X crossover on the binding energies of confined donors in single GaAs/AlxGa1-xAs quantum-well microstructures, Journal of Physics: Condensed Matter. 46 (1994) 10025.
https://doi.org/10.1088/0953-8984/6/46/019.

[158] P. Nithiananthi, K. Jayakumar, Diamagnetic susceptibility of hydrogenic donor impurity in low-dimensional semiconducting systems, Solid State Commun. 137 (2006) 427–430.
https://doi.org/10.1016/j.ssc.2005.12.025.

[159] R. Khordad, Effect of temperature on the binding energy of excited states in a ridge quantum wire, Physica E Low Dimens Syst Nanostruct. 41 (2009) 543–547. https://doi.org/10.1016/j.physe.2008.10.004.

[160] A. Tadjer, B. Abbar, M. Rezki, H. Aourag, M. Certier, Electronic properties and strain effects in zinc blende GaN and InN, Journal of Physics and Chemistry of Solids. 60 (1999) 419–424. https://doi.org/10.1016/S0022-3697(98)00005-5.

[161] C.P. Liu, Y.L. Lai, Z.Q. Chen, Interface characterization and indium content of indium-rich quantum dots in InGaN/GaN multiple quantum wells, in: Appl Surf Sci, Elsevier, 2006: pp. 3922–3927. https://doi.org/10.1016/j.apsusc.2005.09.024.

[162] I. Akasaki, Shortest wavelength semiconductor laser diode, Electron Lett. 32 (1997) 1105–1106. https://ci.nii.ac.jp/naid/80009021688/ (accessed August 15, 2022).

[163] S. Li, J. Schörmann, A. Pawlis, D.J. As, K. Lischka, Cubic InGaN/GaN multi-quantum wells and AlGaN/GaN distributed Bragg reflectors for application in resonant cavity LEDs, in: Microelectronics J, 2005: pp. 963–968. https://doi.org/10.1016/j.mejo.2005.04.003.

[164] S. Li, J. Schörmann, D.J. As, K. Lischka, Room temperature green light emission from nonpolar cubic InGaNGaN multi-quantum-wells, Appl Phys Lett. 90 (2007). https://doi.org/10.1063/1.2475564.

[165] Y. Varshni, Temperature dependence of the energy gap in semiconductors, Physica. 34 (1967). https://doi.org/https://doi.org/10.1016/0031-8914(67)90062-6.

[166] G. Orsal, Y. el Gmili, N. Fressengeas, J. Streque, R. Djerboub, T. Moudakir, S. Sundaram, A. Ougazzaden, J.P. Salvestrini, Bandgap energy bowing parameter of strained and relaxed InGaN layers, Opt Mater Express. 4 (2014) 1030–1041. https://doi.org/10.1364/OME.4.001030.

[167] M. Cardona, Y. Peter, Fundamentals of semiconductors, 3rd ed., springer, 2005. https://doi.org/https://doi.org/10.1007/b137661.

[168] M. Gazzah, B. Chouchen, A. Fargi, H. Belmabrouk, Electro-thermal modeling for InxGa1-xN/GaN based quantum well heterostructures, Mater Sci Semicond Process. 93 (2019) 231–237. https://doi.org/10.1016/j.mssp.2019.01.011.

[169] W. Belaid, H. el Ghazi, I. Zorkani, A. Jorio, Pressure-related binding energy in (In, Ga) N/GaN double quantum wells under internal composition effects, Solid State Commun. 327 (2021) 114193. https://doi.org/10.1016/j.ssc.2021.114193.

[170] M. Barati, G. Rezaei, M.R.K. Vahdani, Binding energy of a hydrogenic donor impurity in an ellipsoidal finite-potential quantum dot, Phys Status Solidi B Basic Res. 244 (2007) 2605–2610. https://doi.org/10.1002/PSSB.200642543.

[171] D.R. Daries Bella, K. Navaneethakrishnan, Donor binding energies and spin–orbit coupling in a spherical quantum dot, Solid State Communications. 130 (2004) 773–776. https://doi.org/https://doi.org/10.1016/j.ssc.2004.02.053.

[172] G. G. Rezaei, N.D. Doostimotlagh, B. Vaseghi, Simultaneous Effects of Hydrostatic Pressure and Conduction Band Non-parabolicity on Binding Energies and Diamagnetic Susceptibility of a Hydrogenic Impurity in Spherical Quantum Dots, Commun Theor Phys. 56 (2011) 377. https://doi.org/10.1088/0253-6102/56/2/31.

[173] A.E. Kasapoglu, The hydrostatic pressure and temperature effects on donor impurities in GaAs/Ga1−xAlxAs double quantum well under the external fields, Phys Lett A. 373 (2008) 140–143. https://doi.org/10.1016/j.physleta.2008.10.080.

[174] F. Ungan, E. Kasapoglu, H. Sari, I. Sökmen, Dependence of impurity binding energy on nitrogen and indium concentrations for shallow donors in a GaInNAs/GaAs quantum well under intense laser field, Eur Phys J B. 82 (2011) 313–318. https://doi.org/10.1140/epjb/e2011-20081-6.

[175] S. Dalgic, B. Ozkapi, Electric field and concentration effects on the binding energy of a non-hydrogenic donor impurity in a finite cylindrical quantum well wire, Journal of Optoelectronics and Advanced Materials . 11 (2009) 2120–2125.

[176] S. Aktas, F. Karaca Boz, S.S. Dalgic, Electric and magnetic field effects on the binding energy of a hydrogenic donor impurity in a coaxial quantum well wire, Physica E Low Dimens Syst Nanostruct. 28 (2005) 96–105. https://doi.org/10.1016/j.physe.2005.02.002.

[177] F.K. Boz, S. Aktas, Magnetic field effect on the binding energy of a hydrogenic impurity in coaxial GaAs/ AlxGa1−xAs quantum well wires, Superlattices Microstruct. 37 (2005) 281–291. https://doi.org/10.1016/J.SPMI.2005.01.004.

[178] U. Yesilgul, H. Sari, F. Ungan, J.C. Martínez-Orozco, R.L. Restrepo, M.E. Mora-Ramos, C.A. Duque, I. Sökmeng, Effects of electromagnetic fields on the nonlinear optical properties of asymmetric double quantum well under intense laser field, Chem Phys. 485–486 (2017) 81–87. https://doi.org/10.1016/j.chemphys.2017.01.013.

[179] S.S. Li, J.B. Xia, Binding energy of a hydrogenic donor impurity in a rectangular parallelepiped-shaped quantum dot: Quantum confinement and Stark effects, J Appl Phys. 101 (2007). https://doi.org/10.1063/1.2734097.

[180] F. Ungan, E. Kasapoglu, H. Sari, I. Sökmen, Dependence of impurity binding energy on nitrogen and indium concentrations for shallow donors in a GaInNAs/GaAs quantum well under intense laser field, European Physical Journal B. 82 (2011) 313–318. https://doi.org/10.1140/EPJB/E2011-20081-6.

[181] A. Fakkahi, A. Sali, M. Jaouane, R. Arraoui, Hydrostatic pressure, temperature, and electric field effects on the hydrogenic impurity binding energy in a multilayered spherical quantum dot, Appl Phys A Mater Sci Process. 127 (2021). https://doi.org/10.1007/S00339-021-05055-X.

[182] H. el Ghazi, I. Zorkani, A. Jorio, Stark effect-dependent of ground-state donor binding energy in InGaN/GaN parabolic QWW, Physica B Condens Matter. 412 (2013) 87–90. https://doi.org/10.1016/j.physb.2012.12.009.

[183] H. el Ghazi, A. Jorio, I. Zorkani, Impurity binding energy of lowest-excited state in (In, Ga) N–GaN spherical QD under electric field effect, Physica B Condens Matter. 426 (2013). https://doi.org/10.1016/j.physb.2013.06.004.

[184] P. Nithiananthi, K. Jayakumar, Effect of temperature on the binding energy of low lying excited states in a quantum well, Int J Mod Phys B. 17 (2003) 5811–5817. https://doi.org/10.1142/S0217979203023331.

[185] O. Akankan, I. Erdogan, A.I. Mese, E. Cicek, H. Akbas, The effects of geometrical shape and impurity position on the self-polarization of a donor impurity in an infinite GaAs/AlAs tetragonal quantum dot, Indian Journal of Physics. 95 (2021) 1341–1344. https://doi.org/10.1007/S12648-020-01813-4.

[186] K.W.J. Barnham, G. Duggan, A new approach to high-efficiency multi-band-gap solar cells, J Appl Phys. 67 (1990) 3490–3493. https://doi.org/10.1063/1.345339.

[187] N.J. Ekins-Daukes, J. Nelson, J. Barnes, K.W.J. Barnham, B.G. Kluftinger, E.S.M. Tsui, C.T. Foxon, T.S. Cheng, J.S. Roberts, Radiative currents in quantum-well solar cells, Physica E Low Dimens Syst

Nanostruct. 2 (1998) 171–176.
https://doi.org/10.1016/S1386-9477(98)00037-X.

[188] K. Barnham, I. Ballard, J. Barnes, J. Connolly, P. Griffin, B. Kluftinger, J. Nelson, E. Tsui, A. Zachariou, Quantum well solar cells, Appl Surf Sci. 113–114 (1997) 722–733.
https://doi.org/10.1016/S0169-4332(96)00876-8.

[189] K. Barnham, J. Connolly, P. Griffin, G. Haarpaintner, J. Nelson, E. Tsui, A. Zachariou, J. Osborne, C. Button, G. Hill, M. Hopkinson, M. Pate, J. Roberts, T. Foxon, Voltage enhancement in quantum well solar cells, J Appl Phys. 80 (1996) 1201–1206.
https://doi.org/10.1063/1.362857.

[190] K.W.J. Barnham, B. Braun, J. Nelson, M. Paxman, C. Button, J.S. Roberts, C.T. Foxon, Short-circuit current and energy efficiency enhancement in a low-dimensional structure photovoltaic device, Appl Phys Lett. 59 (1991) 135–137.
https://doi.org/10.1063/1.105553.

[191] C.I. Cabrera, J.C. Rimada, M. Courel, L. Hernandez, J.P. Connolly, A. Enciso, D.A. Contreras-Solorio, Modeling Multiple Quantum Well and Superlattice Solar Cells, Natural Resources. 04 (2013) 235–245.
https://doi.org/10.4236/nr.2013.43030.

[192] R. Corkish, M.A. Green, Junction recombination current in abrupt junction diodes under forward bias, J Appl Phys. 80 (1996) 3083–3090.
https://doi.org/10.1063/1.363168.

[193] G.L. Araújo, A. Martí, Absolute limiting efficiencies for photovoltaic energy conversion, Solar Energy Materials and Solar Cells. 33 (1994) 213–240.
https://doi.org/10.1016/0927-0248(94)90209-7.

[194] N.G. Anderson, Ideal theory of quantum well solar cells, J Appl Phys. 78 (1995) 1850–1861.
https://doi.org/10.1063/1.360219.

[195] J. Nelson, Quantum-Well Structures for Photovoltaic Energy, in: M.H. Francombe, J.L. Vessev (Eds.), Homojunction and Quantum-Well Infrared Detectors, Academic Press Limited, 1995: pp. 312–366.

[196] H.S. Vogelbaum, G. Sauvé, Recently developed high-efficiency organic photoactive materials for printable photovoltaic cells: a mini review, Synth Met. 223 (2017) 107–121.
https://doi.org/10.1016/j.synthmet.2016.12.011.

[197] M.Y. Mehboob, R. Hussain, Z. Irshad, M. Adnan, Enhancement in the Photovoltaic Properties of Hole Transport Materials by End-Capped Donor Modifications for Solar Cell Applications, Bull Korean Chem Soc. 42 (2021) 597–610.
https://doi.org/10.1002/bkcs.12238.

[198] L. Redaelli, A. Mukhtarova, S. Valdueza-Felip, A. Ajay, C. Bougerol, C. Himwas, J. Faure-Vincent, C. Durand, J. Eymery, E. Monroy, Effect of the quantum well thickness on the performance of InGaN photovoltaic cells, Appl Phys Lett. 105 (2014) 131105.
https://doi.org/10.1063/1.4896679.

[199] N. Watanabe, H. Yokoyama, N. Shigekawa, K. Sugita, A. Yamamoto, Barrier Thickness Dependence of Photovoltaic Characteristics of InGaN/GaN Multiple Quantum Well Solar Cells, Jpn J Appl Phys. 51 (2012) 10ND10.
https://doi.org/10.1143/JJAP.51.10ND10.

[200] J.J. Wierer, D.D. Koleske, S.R. Lee, Influence of barrier thickness on the performance of InGaN/GaN multiple quantum well solar cells, Appl Phys Lett. 100 (2012) 111119.
https://doi.org/10.1063/1.3695170.

[201] L. Redaelli, A. Mukhtarova, A. Ajay, A. Núñez-Cascajero, S. Valdueza-Felip, J. Bleuse, C. Durand, J. Eymery, E. Monroy, Effect of the barrier thickness on the performance of multiple-quantum-well InGaN

photovoltaic cells, Jpn J Appl Phys. 54 (2015) 072302. https://doi.org/10.7567/JJAP.54.072302.

[202] S. Valdueza-Felip, A. Mukhtarova, L. Grenet, C. Bougerol, C. Durand, J. Eymery, E. Monroy, Improved conversion efficiency of as-grown InGaN/GaN quantum-well solar cells for hybrid integration, Applied Physics Express. 7 (2014) 032301. https://doi.org/10.7567/APEX.7.032301.

[203] N.G. Young, R.M. Farrell, Y.L. Hu, Y. Terao, M. Iza, S. Keller, S.P. DenBaars, S. Nakamura, J.S. Speck, High performance thin quantum barrier InGaN/GaN solar cells on sapphire and bulk (0001) GaN substrates, Appl Phys Lett. 103 (2013) 173903. https://doi.org/10.1063/1.4826483.

[204] S. Valdueza-Felip, A. Mukhtarova, Q. Pan, G. Altamura, L. Grenet, C. Durand, C. Bougerol, D. Peyrade, F. González-Posada, J. Eymery, E. Monroy, Photovoltaic Response of InGaN/GaN Multiple-Quantum Well Solar Cells, Jpn J Appl Phys. 52 (2013) 08JH05. https://doi.org/10.7567/JJAP.52.08JH05.

[205] N. Watanabe, M. Mitsuhara, H. Yokoyama, J. Liang, N. Shigekawa, Influence of InGaN/GaN multiple quantum well structure on photovoltaic characteristics of solar cell, Jpn J Appl Phys. 53 (2014) 112301. https://doi.org/10.7567/JJAP.53.112301.

[206] A. Mukhtarova, S. Valdueza-Felip, L. Redaelli, C. Durand, C. Bougerol, E. Monroy, J. Eymery, Dependence of the photovoltaic performance of pseudomorphic InGaN/GaN multiple-quantum-well solar cells on the active region thickness, Appl Phys Lett. 108 (2016) 161907. https://doi.org/10.1063/1.4947445.

[207] A. Mukhtarova, Puits quantiques de composés nitrures InGaN/GaN pour le photovaoltaique, Université Grenoble Alpes (ComUE), 2015.

[208] J.R. Lang, N.G. Young, R.M. Farrell, Y.-R. Wu, J.S. Speck, Carrier escape mechanism dependence on barrier thickness and temperature in InGaN quantum well solar cells, Appl Phys Lett. 101 (2012) 181105. https://doi.org/10.1063/1.4765068.

[209] Q. Deng, X. Wang, H. Xiao, C. Wang, H. Yin, H. Chen, Q. Hou, D. Lin, J. Li, Z. Wang, X. Hou, An investigation on InxGa1−xN/GaN multiple quantum well solar cells, J Phys D Appl Phys. 44 (2011) 265103. https://doi.org/10.1088/0022-3727/44/26/265103.

List of Publications

1. M. Tihtih, J.E.F.M. Ibrahim, M.A. Basyooni, E. Kurovics, W. Belaid, I. Hussainova, I. Kocserha, *Role of A-site (Sr), B-site (Y), and A, B sites (Sr, Y) substitution in lead-free BaTiO3 ceramic compounds: Structural, optical, microstructure, mechanical, and thermal conductivity properties*, Ceram Int. (2022).
   [URL: https://doi.org/10.1016/j.ceramint.2022.09.160]

2. W. Belaid, H. el Ghazi, R. En-Nadir, H.Ş. Kılıç, I. Zorkani, A. Jorio, *Temperature-Related Electronic Low-Lying States in Different Shapes In.1Ga.9N/GaN Double Quantum Wells under Size Effects*, Trends in Sciences. 19 (2022) 5777. (Chapter 4)
   [URL: https://doi.org/10.48048/tis.2022.5777]

3. M. Tihtih, J.E.F.M. Ibrahim, M.A. Basyooni, W. Belaid, L.A. Gömze, I. Kocserha, *Structural, optical, and electronic properties of barium titanate: experiment characterisation and first-principles study*, Materials Technology. (2022) 1–11.
   [URL: https://doi.org/10.1080/10667857.2022.2107473]

4. W. Belaid, H. el Ghazi, M.A. Basyooni, I. Zorkani, A. Jorio, *Ground and two low-lying excited states binding energy in (Al,Ga)N/AlN double quantum wells: temperature and electric field effects*, Philosophical Magazine. (2022) 1–13. (Chapter 5)
   [URL: https://doi.org/10.1080/14786435.2022.2100939]

5. M.A. Basyooni, W. Belaid, A. Houimi, S.E. Zaki, Y.R. Eker, S.Y. Gezgin, H.Ş. Kiliç, *Observation of negative photoresponse in joule-heated Au/Cu2SnS3 ternary chalcogenide thin film deposited by low energy pulsed laser deposition*, Opt Mater (Amst). 128 (2022) 112389.
   [URL: https://doi.org/10.1016/j.optmat.2022.112389]

6. W. Belaid, H. el Ghazi, I. Zorkani, A. Jorio, *Pressure-related binding energy in (In, Ga) N/GaN double quantum wells under internal composition effects*, Solid State Communications. 327 (2021) 114193. (Chapter 3)
   [URL: https://doi.org/https://doi.org/10.1016/j.ssc.2021.114193]

7. W. Belaid, H. el Ghazi, I. Zorkani, A. Jorio, *Impact of QW coupling on the binding energy in InGaN/GaN under the effects of the size, the impurity and the internal composition*, MATEC Web of Conferences. 330 (2020) 01012. (Chapter 2)
   [URL: https://doi.org/10.1051/matecconf/202033001012]

8. R. En-nadir, H. el Ghazi, W. Belaid, H. Abboudi, F. allah Jabouti, A. Jorio, I. Zorkani, *The Confinement Profile Effect on the Optical Properties in Different Inverse-shaped Single InGaN/GaN Quantum Wells*, Iraqi Journal of Physics (IJP). 20 (2022) 1–13.
   [URL: https://doi.org/10.30723/ijp.v20i1.965]

9. R. En-nadir, H. el Ghazi, W. Belaid, A. Jorio, I. Zorkani, H.Ş. Kiliç, *Ground and first five low-lying excited states related optical absorption in In.1Ga.9N/GaN double quantum wells: Temperature and coupling impacts*, Solid State Communications. 338 (2021).
[URL: https://doi.org/10.1016/j.ssc.2021.114464]

10. R. En-nadir, H. el Ghazi, W. Belaid, A. Jorio, I. Zorkani, *Intraconduction band-related optical absorption in coupled (In,Ga)N/GaN double parabolic quantum wells under temperature, coupling and composition effects*, Results in Optics. 5 (2021) 100154.

[URL: https://doi.org/10.1016/j.rio.2021.100154]

11. S. E. Zaki, M. A.Basyooni, W. Belaid, M. Tihtih, J. E. F. M. Ibrahim, G. F. Attia, *Terahertz Resonance Frequency through Ethylene Glycol Phononic Multichannel Sensing via 2D MoS2/PtSe2 Structure*, Materials Chemistry and Physics (2022).
[URL: https://doi.org/10.1016/j.matchemphys.2022.126863]

12. W. Belaid, H. el Ghazi, R. En-nadir, M.A. Basyooni, M. Tihtih, I. Zorkani, A. Jorio, *A theoretical study of the effects of electric field, hydrostatic pressure, and temperature on photoionization cross-section of a donor impurity in (Al,Ga)N/AlN double triangular quantum wells*, Physica Scripta.
Revised

List of Conferences

1. Walid Belaid, Haddou El Ghazi, Hamdi Şükür Kiliç, Izeddine Zorkani, and Anouar Jorio. *A theoretical study of the effects of electric field, hydrostatic pressure, and temperature on photoionization cross-section of a donor impurity in (Al,Ga)N/AlN double triangular quantum wells*, The 2nd international characterization symposium on characterization (ISC'22) 22-25 Septembre 2022. Afyonkarahisar, Turkey. **poster - video conferencing**.

2. Walid Belaid, Haddou El Ghazi, Izeddine Zorkani, and Anouar Jorio. *The Subband Optical Transitions in Symmetric InGaN/GaN Parabolic QW with finite potential under temperature and electric field effects*, online International Conference of Physics Students (ICPS) 2021, 5-8 August 2021. Copenhagen, Denmark. **poster - video conferencing**.

3. Walid Belaid, Haddou El Ghazi, Izeddine Zorkani, and Anouar Jorio. *The effect of temperature on shallow donor impurity in rectangular, parabolic, and triangular InGaN/GaN DQWs*, 5th international Erciyes conference on scientific research, 16-17 April 2021. Kayseri, Turkey. **Oral presentation - video conferencing**.

4. Walid Belaid, Haddou El Ghazi, Izeddine Zorkani, and Anouar Jorio. *Pressure, Size, Impurity, and Internal Composition Effects on Shallow Donor Binding Energy in InGaN/GaN Square Simple and Double QW*, 8th International Renewable and Sustainable Energy Conference (IRSEC'20), 28 November 2020, Tetouan- Morocco. **Oral presentation- video conferencing**.

5. Walid Belaid, Haddou El Ghazi, Izeddine Zorkani, and Anouar Jorio. *Impurity-related optical properties of InGaN MQW under laser effect*. N@NO'2018: The first international online conference on nanoscience and nanotechnology, 28-29 December 2018, Fes, Morocco. **Oral presentation**.

6. Walid Belaid, Haddou El Ghazi, Izeddine Zorkani, and Anouar Jorio. *Laser effect on linear and nonlinear optical properties of InGaN multiple QW*, 5th international symposium EVF'2018 "Energy and city of the future", 25-26 October 2018, Fes, Morocco. **Oral presentation-Proceedings**